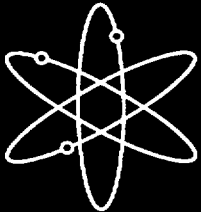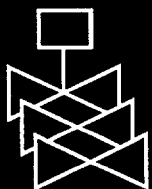# Advanced Nondestructive Evaluation for Steam Generator Tubing

Argonne National Laboratory

U.S. Nuclear Regulatory Commission
Office of Nuclear Regulatory Research
Washington, DC 20555-0001

Advanced Nondestructive Evaluation for Steam Generator Tubing

Prepared by
S. Bakhtiari, J.Y. Park, D.S. Kupperman, S. Majumdar, W.J. Shack

Argonne National Laboratory
9700 South Cass Avenue
Argonne, IL 60439

J. Muscara, NRC Project Manager

Advanced NDE for Steam Generator Tubing

S. Bakhtiari, J. Y. Park, D. S. Kupperman, S. Majumdar, W. J. Shack

Abstract

This report describes research activities carried out at Argonne National Laboratory (ANL) as part of the Steam Generator (SG) Tube Integrity Program sponsored by the U.S. Nuclear Regulatory Commission (USNRC). As a follow-up to a preceding publication on the assessment of advanced nondestructive evaluation (NDE) techniques for inservice inspection of steam generator tubing. This report provides an overview of more recent studies associated primarily with signal processing and data analysis techniques applied to eddy current NDE. Results of efforts made to date on implementation of various algorithms that pertain to computer-aided analysis of eddy current rotating probe data are discussed. As a benchmark for NDE accuracy, production and destructive characterization of specimens with laboratory-induced cracking are described. The effect of uncertainties in NDE estimates of flaw size on the prediction of tube structural integrity is addressed.

Contents

Figures

Tables

Executive Summary

This report is an overview of recent studies associated primarily with signal processing and data analysis techniques in application to eddy current nondestructive evaluation (NDE) for inservice inspection (ISI) of SG tubing. The work was carried out at Argonne National Laboratory (ANL) as part of the Steam Generator (SG) Tube Integrity Program sponsored by the U.S. Nuclear Regulatory Commission (USNRC). Results of efforts made to date on implementation of various algorithms that pertain to computer-aided analysis of eddy current rotating probe data are discussed. Also described are production and destructive characterization of specimens with laboratory-induced cracking used to benchmark NDE accuracy. The effect of uncertainties in NDE estimates of flaw size on the prediction of tube structural integrity is also addressed.

An overview is presented of the basic structure of a data analysis scheme that was implemented at ANL to explore the applicability of such algorithms for more accurate and efficient processing of eddy current rotating probe data. Some key objectives of this work have been to characterize flaws in the ANL tube bundle mock-up in order to minimize the expense of tedious destructive examinations, and to further assist in parallel studies under this program on prediction of tube structural integrity from NDE estimates of flaw profiles. NDE assessments so far have been limited to analyses of data from rotating pancake coils, however, many of the fundamental processes described here are applicable to other probe geometries and coil configurations.

Implementation of data conversion and calibration routines at ANL for off-line manipulation of eddy current data is initially addressed. Subsequently, a general description of signal processing and data analysis schemes adapted for manipulation of C-scan recordings with high-resolution probes is presented. The issue of data quality and its implications on reliability and uniformity of NDE results is also discussed. Selected test cases from analyses of various batches of machined and laboratory-produced specimens with chemically induced cracking are provided to illustrate the NDE results. Comparisons of estimated flaw profile by NDE with true state by fractography are subsequently presented, following a brief description of destructive examination procedure. Finally, results of limited statistical analysis to determine the significance of NDE uncertainties on predicting the structural integrity of tubing are shown. Reference is provided to a report with a detailed description of analytical formulations used here to estimate the failure pressure from NDE and destructive profiles.

Acknowledgments

Acronyms and Abbreviations

ANL	Argonne National Laboratory
APC	alternate plugging criterion
ARC	alternate repair criteria
ASME	American Society of Mechanical Engineers
ASTM	American Society for Testing and Materials
EC	eddy current
EDM	electro-discharge-machined
EPRI	Electric Power Research Institute
FBH	flat-bottom hole
FIR	finite-impulse response
GUI	graphical user interface
HP	Hewlett Packard
ID	inner diameter
IDSCC	inner-diameter stress corrosion crack/cracking
IGA	intergranular attack
IIR	infinite-duration impulse response
IPC	interim plugging criterion
ISI	inservice inspection
MLR	multiple linear regression
MP	Multiparameter
NDE	nondestructive evaluation
NRC	U.S. Nuclear Regulatory Commission
OD	outer diameter
ODSCC	outer-diameter stress corrosion crack/cracking
PC	(Windows) personal computer
PCR	principal component regression
RPC	rotating pancake coil
SCC	stress corrosion crack/cracking
SG	steam generator
S/N	signal-to-noise ratio
SVD	Singular value decomposition
TSP	tube support plate
TW	throughwall

1 Introduction

A description of research activities carried out at Argonne National Laboratory (ANL) as part of the Steam Generator (SG) Tube Integrity Program sponsored by the U.S. Nuclear Regulatory Commission (USNRC) is provided in this report. It is a follow-up report to a preceding publication on the assessment of advanced nondestructive evaluation (NDE) techniques for inservice inspection (ISI) of SG tubing.[1] An overview of more recent studies associated primarily with signal processing and data analysis techniques in application to eddy current NDE of SG tubing is presented. In particular, results of efforts made to date on implementation of various algorithms that pertain to computer-aided analysis of eddy current (EC) rotating probe data are discussed. Production and destructive characterization of specimens with laboratory-induced cracking, used to benchmark NDE accuracy, are also described. Finally, the effect of uncertainties in NDE estimates of flaw size on the prediction of tube structural integrity is briefly addressed.

In the following sections, the basic structure of a computer-aided data analysis algorithm that was implemented at ANL as a means for more accurate and efficient processing of EC rotating probe data is described. Implementation of data conversion and calibration routines for off-line manipulation of EC data is initially addressed. A general overview of signal processing and data analysis schemes adapted for manipulation of C-scan recordings with high-resolution rotating probes is presented. The issue of data quality and its implications on reliability and uniformity of NDE results is also discussed. Selected test cases from analyses of various batches of laboratory-produced specimens with chemically induced cracks are provided to illustrate the NDE results. Comparisons of estimated flaw profile by NDE with true state by fractography are subsequently presented, following a brief description of destructive examination procedure. Finally, results of statistical analysis to determine the significance of NDE uncertainties on predicting the structural integrity of tubing are presented. Reference to reports with a detailed description of analytical formulations used here to estimate the failure pressure from NDE and destructive profiles are provided.

2 Computer-Aided Analysis of Eddy Current Inspection Data

Manual analysis of multiple-frequency EC data is a tedious and challenging process. No qualified technique, manual or automated, currently exists that could provide reliable estimation of flaw size over a wide range of SG tubing damage. Conventional data analysis methods become rather subjective when dealing with complex forms of degradation such as stress corrosion cracking (SCC). Signal distortion by interference from internal/external artifacts in the vicinity of a flaw further complicates discrimination of flaw signals from noise. In this context, noise is referred to any random or coherent signal that is not induced by a flaw. In comparison to high-speed bobbin coil inspections, high-resolution multicoil rotating and array probes generate enormous amounts of data over comparable scanning lengths. Rotating probe ISI of SG tubing is thus generally restricted to areas that are historically predisposed to known damage mechanisms and sections of particular interest that are flagged by the initial bobbin coil examinations. More extensive application of such probes for improving NDE reliability rests in part on automating various stages of the data screening process. Computer-aided data analysis

is a viable means to overcome many of the challenges associated with reliable processing of data acquired with high-resolution probes.

An overview of the basic structure of a data analysis scheme that was implemented to explore the applicability of such algorithms for the processing of eddy current rotating probe data is presented next. Some key objectives of this work have been to characterize flaws in the ANL tube bundle mock-up in order to minimize the expense of tedious destructive examinations and to further assist in parallel studies under this program on prediction of tube structural integrity from NDE estimates of flaw profile. NDE assessments so far have been limited to analyses of data from rotating pancake coils; however, many of the fundamental processes described here are applicable to other probe geometries and coil configurations. The following section includes a brief description of the structure and fundamental operations adapted for computer-aided analysis of EC rotating probe data.

2.1 Data Processing Structure

Computer-aided data analysis here refers to a series of routines assembled to carry out various stages of processing of the raw EC inspection data. Figure 1 depicts the basic architecture of the algorithm implemented to allow for off-line analysis of data acquired with a commercial EC testing instrument. Blocks associated with the processes mentioned in this report are numbered. Output of the acquisition block shown in Fig. 1 is the digitized recordings of a multiple-frequency inspection system. The EC testing instrumentation and software currently in use at ANL are a Miz-30^{TM} (Zetec, Inc.) remote data acquisition unit that is controlled under the HP-UX-based Eddynet^{TM} (Zetec, Inc.) environment. To facilitate development of algorithms for evaluation of EC inspection results, codes have been developed to convert the raw inspection data to a standard file format. All data analysis and signal processing algorithms have been implmented by using the PC-based software MATLAB, which is a high-level scripting language that provides an efficient environment for developing codes, together with convenient graphical user interfaces (GUIs) and graphical displays of the results.

The block diagram shown in Fig. 1 can be divided into three basic components: data conversion, calibration, and analysis stage. A description of each block is provided in the following sections. In the conversion stage (block 1) digitized recordings of inspection data that sequentially represent the in-phase and quadrature signal components are converted to a readable format for off-line manipulations. In the subsequent stage, multiple-frequency raw EC data, shown as block 2, are calibrated for all the recorded frequency channels. Finally, in the data analysis stage, represented by blocks 3-6, calibrated data are processed to ultimately produce NDE profiles that represent sizing estimates along a selected test section of a tube.

2.2 Conversion and Calibration Routines

A series of algorithms has been implemented under the MATLAB environment to carry out the conversion, normalization, and reformatting of EC readings for subsequent analysis. An interactive MATLAB program, *ECTool*, calls the data retrieval and calibration routines through a single GUI control window. This software currently retrieves and processes inspection data acquired with either the Zetec MIZ-18 or MIZ-30 EC inspection instruments. With appropriate modifications, the software could also be used to convert inspection results from other standard commercial instruments.
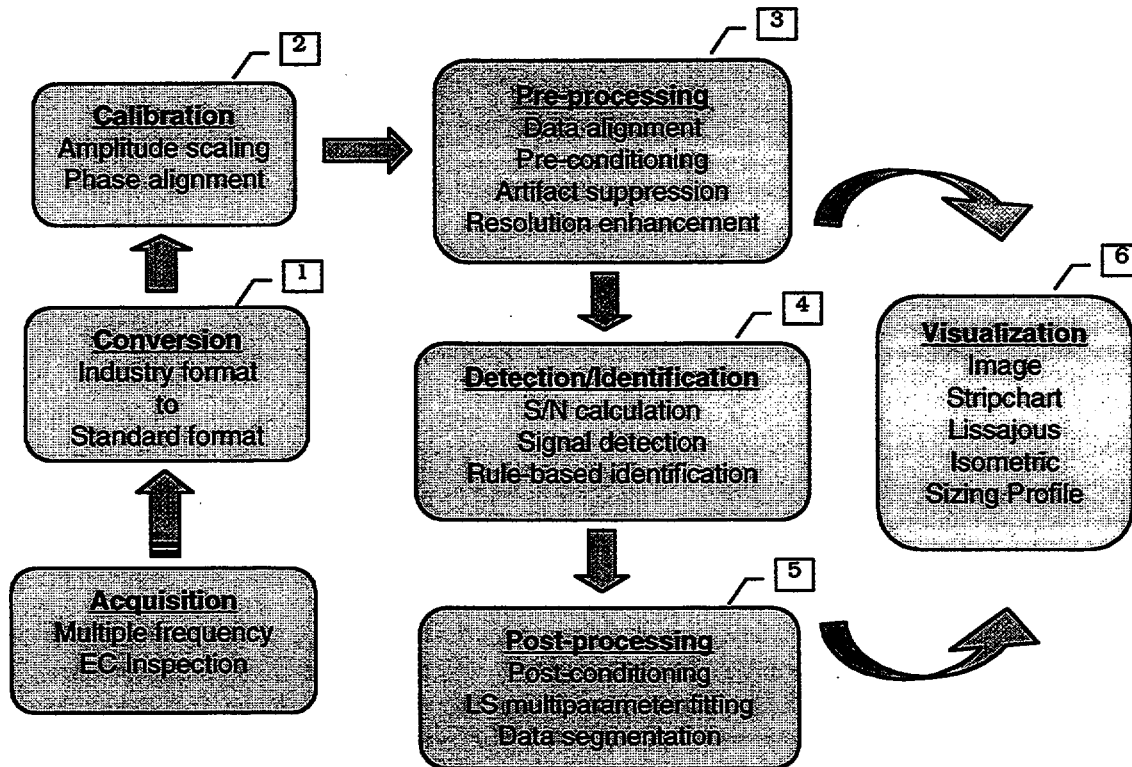
Figure 1. Schematic diagram showing basic structure of computer-aided data analysis algorithm. Blocks associated with operations described in this report are numbered.

The main control window contains virtual instrument controls such as pull-down menus, editable text, and pushbuttons that activate various functions for the manipulation of the NDE results. Data files in Eddynet format are initially read by these codes. The data conversion routine extracts the essential header information (currently assumed to be from MIZ-18 or MIZ-30 instruments), such as the number of channels and their associated frequencies, from the original Eddynet-formatted files. The decoded header information contains the frequency and channel configuration that is subsequently used to sort out raw EC readings. The reformatted data matrix, along with the header and coil configuration information, is then stored in a user-defined data file. Normalization values of all the available channels are calculated by using the inspection results from a calibration standard tube. These values consist of amplitude scaling factors, phase angle rotations, and null values that are automatically calculated based on user-defined approximate locations of known indications on the tube. Although the necessary information for standard normalization procedures is defined as a set of default values in the program, the code also allows calculation of these values in an arbitrary fashion. Finally, raw EC readings are calibrated by another code that is also activated from the main menu and applies the previously calculated normalization factors to each new raw data file. To avoid incorrect application of normalization factors, the codes initially check the header information

3

for consistency between the original calibration standard tube and new data files that are subsequently loaded.

2.2.1 Data Conversion

Eddynet provides inspection data in MIZ-18 and MIZ-30 formats. The header sizes for MIZ-18 and MIZ-30 are currently preset to contain a fixed number of bytes. Following the header is the data stream that sequentially contains the horizontal and vertical signal components for all channels that are stored in 2-byte signed integer format. The necessary information can be extracted from the header to carry out the data conversion. This information reveals whether the data are in the MIZ-18 or MIZ-30 formats and the numbers of channels in the data file. Once these two pieces of information are determined, the conversion routine can retrieve and convert EC data files to a format suitable for any future manipulations. Figure 2 shows an intermediate display of the tools under conversion and segmentation functions that are activated from the main menu.

2.2.2 Automated Data Calibration

Calibration of raw EC data plays an important role in any data analysis procedure. Conventional phase angle calibration procedures for normalizing EC data are carried out manually and routinely involve visual alignment of the impedance-plane signal trajectory (i.e., lissajous plot) with respect to some reference indication. This implies that the extent of background fluctuations and signal-to-noise ratio (S/N), as well as analyst judgment, could affect the calibration process and consequently lead to varying estimates of a desired parameter. Because estimates of flaw depth from phase angle information of multifrequency inspection data depend heavily on initial calibrations, it is expected that computer-aided data calibration routines will play an essential role in uniform and accurate normalization of raw EC data.

Automatic calibration of multifrequency EC inspection results could provide more efficient data analysis and more importantly render consistent calibrations by reducing variability in analyst interpretation in the presence of noise (i.e., background fluctuations and artifacts). Algorithms for automatic calibration have been developed and incorporated into *ECTool* that display the acquired data in standard graphical formats. Signals from machined flaws on a calibration standard tube are used to normalize the amplitude and phase of raw EC data. Amplitude scaling is performed with respect to peak signal voltage from a known indication on a calibration standard. Alignment of the phase angle at each frequency is typically made in reference to either a shallow inside-diameter (ID) or a throughwall flaw.

Figure 3 displays the user interfaces along with intermediate and final stages of calibration of raw EC readings collected with the 2.92-mm (0.115-in.)-diameter primary pancake coil of a three-coil rotating probe on a 18-notch standard. The code sequentially asks the user to interactively provide information on the approximate positions of lift-off signal, a sound portion of the tube, and an amplitude scaling artifact; it calculates the phase angle rotation, null value, and scaling factors for uniform normalization of all of the data files that belong to the same calibration group.

4
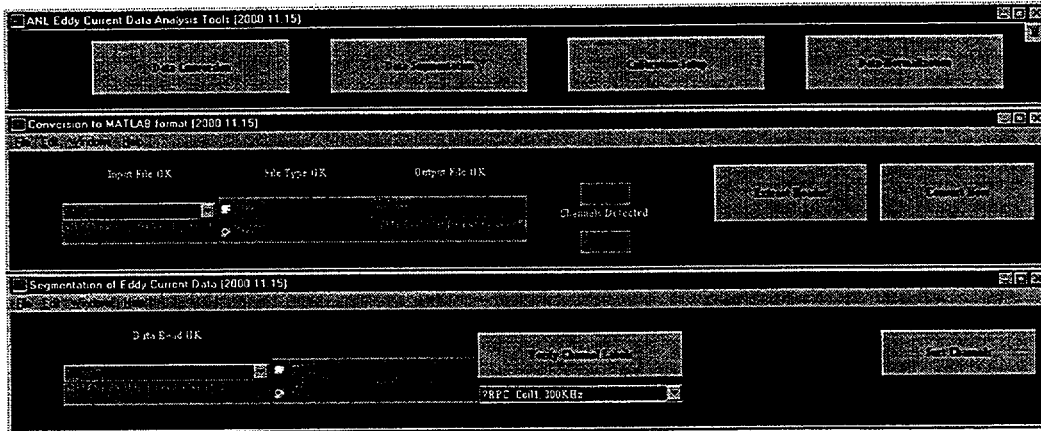
(a)
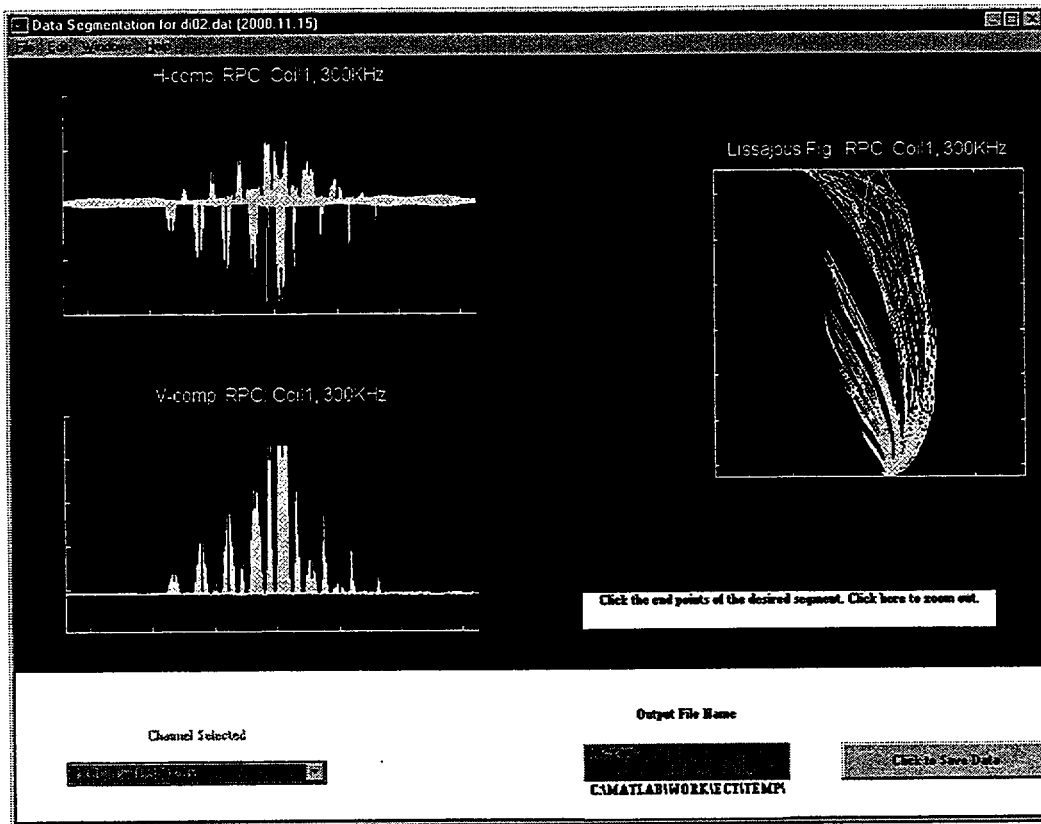
(b)

Figure 2. *Display of GUIs for (a) main ECTool menu with data conversion and segmentation submenus and (b) strip chart and lissajous display of segmented raw data. Eddy current data was acquired on a 18-notch standard with a 2.92-mm (0.115-in.)-diameter primary pancake coil of a three-coil rotating probe.*

5
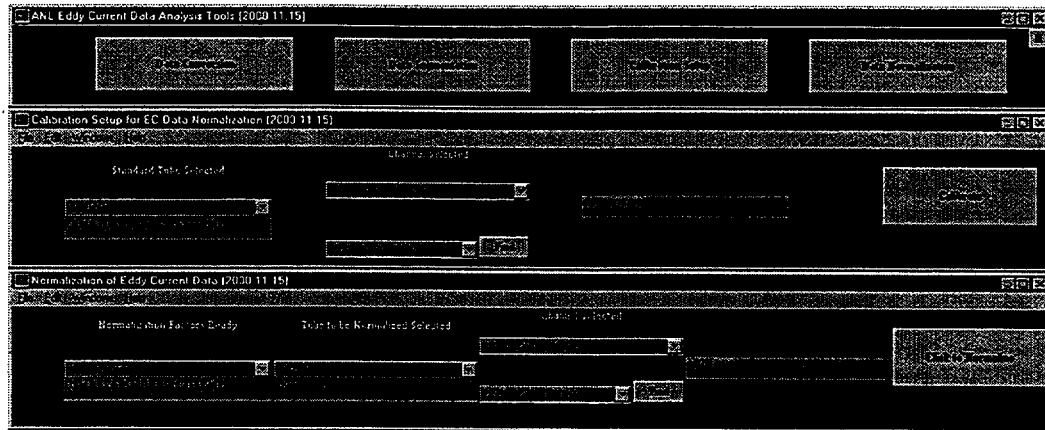
(a)
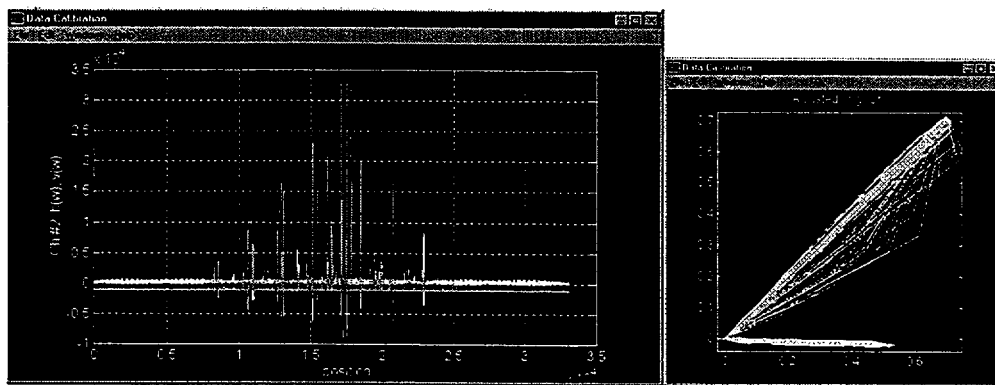
(b)
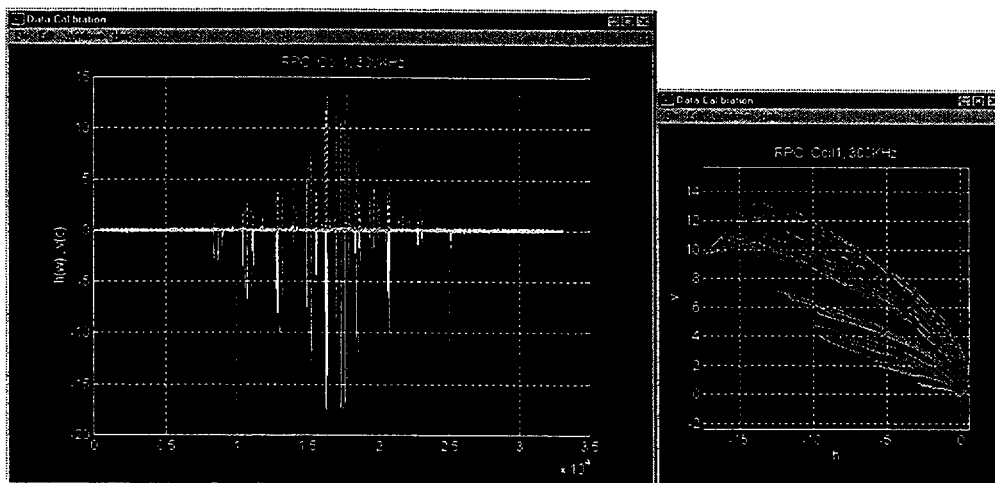
(c)

Figure 3. Display of GUIs for (a) main ECTool menu with data calibration submenus, (b) raw data and trigger channel, and (c) calibrated data in strip chart and lissajous display format. Eddy current data was acquired on a 18-notch standard with a 2.92-mm (0.115-in.)-diameter primary pancake coil of a three-coil rotating probe.

2.3 Signal Processing, Data Analysis, and Display Routines

In reference to Fig. 1, the data analysis section (shown by blocks 3-6) is composed of three basic stages: pre-processing, flaw detection and identification, and post-processing of data. These blocks consist of various scripts that successively perform the calculation of S/N for all channels, apply filters for pre- and post-processing of data, and ultimately combine multiple-frequency information from all processed channels to provide an estimate of the depth profile for the entire tubing test section. Both frequency and spatial domain filters are incorporated for signal conditioning, baseline reduction, and resolution enhancement. Initially, the S/N ratio is calculated from a user-defined approximate location along the trace baseline and minimum detectable amplitude from a calibration standard tube. Subsequently, this information is used to implement a series of filters that perform suppression of artifacts, baseline fluctuations, and signal enhancement or restoration. Filter characteristics are determined by taking into account both the coil configuration and the sampling frequency of the inspection data. Identification of flaws and their origin is made by a series of rules that are applied to the multiple-frequency EC data. Both amplitude and phase relationships among the processed channels are used at this stage of the process. Finally, the phase information at multiple frequencies is combined to calculate the depth profile for the tube test section in reference to known indications on a calibration standard tube. Multivariate analysis is used for estimating the NDE depth profile of the tube using the available information from multiple channels. In the following sections, brief descriptions of various signal processing and data analysis schemes that perform the fundamental operations for multiparameter analysis of EC rotating probe data is provided.

A series of algorithms have been implemented as MATLAB scripts to provide in real-time profile of flaw depth in a SG tube test section from NDE inspection results. These codes are executed through a user interface tool to automatically process EC inspection results at the multiple frequencies acquired with rotating probes. Figure 4 shows the main window of the GUI tool *ETProf*, which incorporates various algorithms for the processing of raw EC data. Pull-down menus, pushbuttons, and editable text areas on the display can be activated to perform the various stages of data analysis process. A series of modifications were recently incorporated to allow for more quantitative mapping between NDE estimates and destructive examination results. Figure 4 also shows several forms of graphics currently in place for the visualization data at various stages of analysis. Subsequent to calculation of the depth profile, estimated values are converted to percent of tube wall thickness. Reconstruction of helically scanned data into C-scan format allows for the observation of sizing results from any azimuth and elevation view angle and for any axial or circumferential cross section of the tube. Scaling of data in axial and circumferential directions allows for direct deduction of flaw extent along the tube. Test case results on analyses of various tubing specimens using this computer-aided data analysis tool are provided later this report.

7
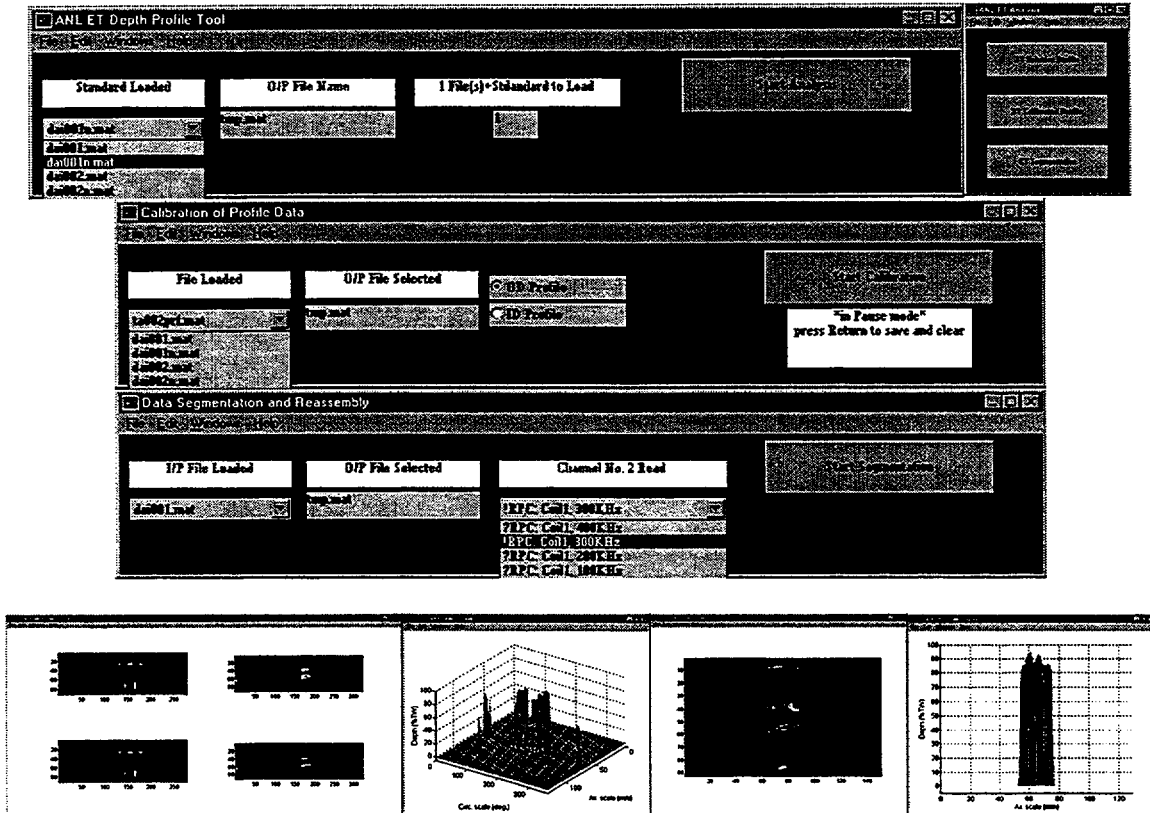
Figure 4. Series of MATLAB-based Graphical User Interface (GUI) tools (top three rows) for automated analysis of EC inspection results acquired with standard commercial instruments. Also shown (bottom row) are several graphical display formats such as image, terrain, and cross-sectional NDE profiles of tube test section at various stages of analysis.

2.3.1 Application of Digital Filters

Analog and digital filters are often integral parts of any electronic measurement instrument. They may be implemented either in the hardware or software and serve in essence to discriminate between real signals and noise. Although digital filters in theory are the numerical counterparts of analog devices, there are many practical cases in which the two cannot be substituted for one another. A fundamental difference that separates the two is that at a given point in time, in-line analog filters operate only on the basis of information available up to the point at which data have been collected, in contrast to off-line filters that also have access to information on data points ahead. This additional information would allow implementation of various digital filters with no apparent analog equivalent. The discussion here is concerned only with the application of digital filters for the processing of EC inspection data. Several filtering operations that were adopted for this specific application are described. They are implemented either in the original signal domain (i.e., spatial or time) or in the Fourier domain (i.e., frequency). The choices for selecting the proper domain are discussed below.

8

In its most basic form, the one-dimensional (1-D) discrete form of a spatial domain digital filtering may be written as

$$g(-n\mathrm{D}x) = \sum_x f(x)h(x - n\mathrm{D}x), \quad n = 0,1,2,... \tag{1}$$

in which $f(x)$ is the original signal, $h(x)$ is the filter function, $g(n\Delta x)$ is the filtered signal, and Δx denotes the sampling interval. Equation 1 also represents the discrete form of convolution integral in which $h(x)$ would then represent the convolution kernel. A fundamental mathematical theorem states that convolution in the time domain is equivalent to multiplication in the frequency domain. This can be represented as

$$g(x) = f(x) * h(x) \tag{2a}$$

$$G(w) = F(w)\,h(w), \tag{2b}$$

in which Eqs. 2(a) and 2(b) denote the transformation pairs that show the equivalency of the convolution and multiplication operations in the original and Fourier domain, respectively. With EC rotating probe data being collected in a two-dimensional (2-D) fashion, Eq. 1 can be expanded to represent the discrete form 2-D convolution or filtering equation as

$$g(x, y) = \sum_{m=0}^{M-1} \sum_{n=0}^{N-1} f(m,n)h(x - m, y - n), \tag{3}$$

where (x,y) is the spatial coordinate of a pixel in a matrix of C-scan data. For EC data, f and g are complex quantities that represent in-phase and quadrature components of a signal.

In regard to processing of eddy current NDE data, digital filters generally serve three basic purposes: noise reduction, artifact suppression, and signal enhancement or restoration. All of these operations, however, are fundamentally aimed at improving the S/N ratio. In this context, noise is characteristically defined as any unwanted signal, regardless of its source. Transformations of the form shown in Eq. 2 are quite widespread in signal and data processing applications. In general, they provide information that may not readily be available in the other domain. When frequency domain filtering is the desired method, data are transformed to the Fourier domain, processed, and then reverse-transformed into the original domain. The choice for using either a frequency or spatial domain operation depends on the signal features that need to be suppressed or preserved. No strict rules can be given as to use of spatial or frequency domain filtering. For EC signals, frequency domain operations are often better suited for reducing low-frequency baseline fluctuations and high-frequency noise. Spatial domain filtering, on the other hand, is typically more appropriate for enhancing subtle features in the data. In general, when the frequency content of the signal and noise are well separated, frequency domain operations are the preferred method for noise suppression.

2.3.2 Signal Conditioning

Pre- and post-conditioning of data are some of the most fundamental operations in any signal processing application. The aim of such data manipulations is to minimize the contribution from known sources of signal distortion. Coherent noise that is present at multiple

channels occurs commonly in EC testing of SG tubing. Low-frequency baseline variations and high-frequency noise are also always present, to various degrees, in any EC inspection data. Typical sources of low-frequency signals, particularly for absolute impedance coils, are probe wobble, probe wear, temperature fluctuations, and gradual dimensional and geometry changes of the tube. Tube ID conditions and electronic noise, on the other hand, are typical sources of high-frequency noise. For both these sources of signal degradation, frequency domain filters can be designed to effectively suppress unwanted signals. Two types of filtering have been incorporated into the data analysis routine to reduce the level of such noise. They consist of standard Fourier domain filters and the more elaborate finite-impulse response (FIR) filters. In reference to Eq. 2, conventional filtering in frequency domain is performed through application of the filter transfer function to the Fourier transform of the signal. Filter characteristics are determined based on the data sampling rate and the frequency content of noise. A brief description of FIR filters used to serve the same purpose is given below.

Frequency domain bandpass FIR filters are nonrecursive filters that offer certain advantages and limitations over recursive infinite-duration impulse response (IIR) filters. The primary advantages are their linear phase, stability, finite-duration transients, and efficiency of implementation. FIR filters are always stable, but require longer sequences to meet the same requirements as their IIR counterparts. This latter property, a direct consequence of their simpler transfer function, often translates into more computation time for nonrecursive filters. As with all frequency-domain filters, when conditions are not ideal, the increase in S/N ratio gained by the filtering process is always accompanied by some degree of perturbation of amplitude and phase of the original signal.

The time-domain difference equation for a linear filter with input sequence $x(k)$ and output sequence $y(n)$ could be written in a general form as

$$y(n) = \sum_{k=0}^{M} b(k)\,x(n-k) + \sum_{k=1}^{N} a(k)\,y(n-k), \qquad (4)$$

in which the coefficients a and b define the filter response. The transfer function of the IIR filter in z domain, which is the z-transform of the time-domain difference Eq. 4, can be described by

$$H(z) = \frac{Y(z)}{X(z)} = \frac{\sum_{k=0}^{M} b(k)z^{-k}}{a_0 + \sum_{k=1}^{N} a(k)z^{-k}}, \qquad (5)$$

where $a_0 = 1$ for the case of a FIR filter, and the summation in the denominator of Eq. 5 vanishes. The difference between the two filtering type can be seen by examining the filter frequency response, which is a rational function in z^{-1} for an IIR filter and represents a discrete Fourier transform for a FIR filter. Regardless of filter type, unless the data sequence in the Fourier domain is composed of sinusoidal components of the desired signal and noise that are well separated, the amplitude and phase of the filtered signal will always experience perturbation with respect to those of the original signal. This is of particular concern in the case of EC signals in which the frequency content of the entire data sequence is often closely spaced and thus requires very sharp (high-order) filters to separate real signals from

background variations. Filters for EC signal conditioning often require a sharper transient and consequently a larger number of coefficients, because much of the useful information content of the Fourier domain spectrum is at the low-frequency end. Studies so far have suggested that frequency domain filters are generally more suitable for improving detection probability. Phase angle perturbations that are a result of filter application can often lead to more complex impedance-plane trajectories, which may complicate conventional data analysis procedures.

2.3.3 Signal Enhancement and Restoration

Two basic approaches for improving data quality are the signal enhancement and signal restoration methods. Signal enhancement refines the quality of data without any knowledge of the degradation phenomenon. Signal restoration, on the other hand, is founded on the assumption that the degradation source is well understood so that an inverse process could be implemented to recover the true response. The principal objective in both cases is to treat the data so that the result is more suited for a specific application than the original data. Although the two approaches are clearly differentiated in most standard data restoration applications, distinction between the two becomes less apparent in practical applications associated with the EC testing of SG tubing. This is because of the difficulty in accurately modeling the underlying degradation phenomenon that arises from the combined influence of many factors, in addition to the blurring effect of the coil impulse response. Both data enhancement and approximate restoration schemes have been incorporated into the multiparameter data analysis algorithm. Studies to date suggest that comparable results can be achieved by the two techniques for the processing of EC rotating probe data. Signal restoration, referred to here as approximate deconvolution or inverse filtering, is implemented in the frequency domain. Signal enhancement, on the other hand, is implemented directly in the original spatial domain. Although deconvolution-based methods are generally expected to produce more accurate results, they are also computationally more intensive.

The application of approximate deconvolution schemes to real-time processing of multifrequency inspection results has been investigated at ANL. This study was prompted by the need for more accurate characterization of complex cracking morphologies in SG tubing. Deconvolution techniques are used in a wide range of signal processing applications, primarily to recover signals distorted by the sensing environment. In EC inspection applications, pseudoinverse filters could be effective for enhancement of spatial resolution that is degraded by the finite spread of the coil-induced field. Better separation of flaw indications from extraneous signals could, in turn, improve the estimation of flaw depth determined from the phase-angle information of multifrequency data. Frequency-dependent signal restoration could also help reduce differences in probe response at different frequencies. This could be particularly beneficial for multifrequency mixing techniques in which the differences in the coil impulse response at the base and auxiliary frequencies could significantly contribute to the level of mix residuals.

The fundamental limitation of data enhancement and restoration techniques in application to EC signals could be attributed to the flow of current in a conducting medium that is governed by the diffusion phenomenon. This suggests that distortion is not simply a modulation of signal amplitude. Instead, the waveform could experience a complete alteration of structure that is not linearly dependent on its original form. Another factor that could significantly influence the degree to which a signal can be recovered is the lack of separation between the spectral content

11

of flaw indications and extraneous signals. Internal/external artifacts and design discontinuities (e.g., conducting and magnetic deposits, tube dimensional variations, external support structures, etc.) could produce signal trajectories with spectral components that are close to those from flaw indications. Furthermore, practical sampling rates that are typically used for acquisition of ISI data with rotating probes do not render continuous smooth signals that are essential for optimal restoration by inverse-filtering schemes. Finally, it is important to note that physically realizable optimal inverse filters are often unstable. For this reason, approximate deconvolution algorithms may provide the best alternative for real-time restoration of EC flaw signals for practical ISI applications.

Signal Enhancement– When the exact form of the degradation process can only be approximated, signal enhancement techniques are often the first choice for the treatment of data. Because such techniques can be implemented directly in the original domain, they are computationally efficient. Data enhancement is achieved by applying pre-stored kernels to the EC C-scan data in accordance with Eq. 3. Both smoothing and peak restoration are attained in this manner. The kernels in effect perform least squares polynomial fitting of the data. Because of the availability of information around any center pixel, a symmetric convolution process is applied. Typical 2-D kernels are shown in the following discussion on signal restoration.

Signal Restoration– Degradation of the probe's spatial resolution in two dimensions could, in general, be described by the following discrete convolution model:

$$g(x, y) = \sum_{m=0}^{M-1} \sum_{n=0}^{N-1} f(m,n)h(x - m, y - n) + h(x, y)$$
$$\equiv h(x, y) * f(x, y),$$

(6)

where f is the nondistorted signal (probe input), g is the measured signal (probe output), h is the coil impulse response, η is the additive noise, and $*$ denotes the convolution operation. With prior knowledge of the distortion model, the original signal may then be recovered through deconvolution, either directly by polynomial division in the spatial domain, or more efficiently by transformation into frequency domain. The inverse-filtering operation in the Fourier domain could be expressed as

$$\hat{f}(x, y) = \mathcal{F}^{-1}\left[\frac{G(u, v)}{H(u, v)}\right]$$

(7)

where $\hat{f}$ is the new estimate of the original signal. The distorted frequency-domain signal $G(u,v)$ and Probe transfer function $H(u,v)$ are defined as

$$G(u, v) = \mathcal{F}[g(x, y)]$$

(8)

$$H(u, v) = \mathcal{F}[h(x, y)],$$

(9)

in which the transformed variables (u,v) are inversely proportional to the sample spacing in the original spatial domain. Equation 7 suggests that the level to which a signal can be restored is dependent on knowledge of the degradation function.

Representative amplitude response (1-D circumferential trace) of a rotating probe to a narrow axial flaw is shown in Fig. 5(a). The coil is a standard 2.92-mm (0.115-in.)-diameter pancake excited at a frequency of 300 kHz. The machined flaw is an axial notch of length 6.35 mm (0.25 in.) and depth of 100% TW. The trace in this figure was resampled at approximately twice the minimum prescribed ISI sampling rate of rotating probes. As an approximation to the coil response in Fig. 5(a), two different functions were considered in this study. Figure 5(b) displays Gaussian and Lorentzian functions of the form

$$G(x) = Ae^{-a(x-b)^2} \tag{10}$$

$$L(x) = \frac{A}{1 + a(x-b)^2}, \tag{11}$$

in which β determines the peak position, and the parameter α is inversely proportional to the variance for the Gaussian function and to the width at half-height for the Lorentzian function. Values of the parameter β in Fig. 5(b) were selected so that the two functions have approximately the same widths at half-height.

Although both Gaussian and Lorentzian functions could be considered as close approximations to the coil impulse response, the former can be adjusted to better match the measured response. This is expected, because coil impedance is a complex exponential function (i.e., a sinusoidal response). However, the Gaussian function, which is often the principal choice for simulating the coil impulse response, may not be the optimal choice for inverse-filtering applications. The sharp taper of this function could result in amplification of high-frequency signal components and false indications. The smoothly decreasing Lorentzian function, on the other hand, could resolve this problem associated with the use of Gaussian function as the impulse response of the coil.

Figure 6 displays a series of 2-D kernels that was constructed from 1-D Gaussian and Lorentzian functions of Fig. 6(b). The two types of kernels considered in this study consisted of (1) two superimposed orthogonal 1-D functions and (2) "true" 2-D impulse response made by rotating a 1-D function about its vertical axis. Although both the Gaussian and Lorentzian functions have been implemented as part of a 2-D deconvolution algorithm, in all test cases considered so far the results have pointed to the consistency and improved stability of the Lorentzian over the Gaussian impulse response for restoration of rotating pancake coil (RPC) signals.

Test Case Results on Signal Restoration for Machined Specimens– Preliminary evaluation of the 2-D deconvolution scheme that is integrated into the multiparameter data analysis algorithm was carried out by using a subset of laser-cut notch specimens. The geometry of all the available laser-cut specimens is depicted in Fig. 7. Flaw dimensions are listed in Table 1. Inspection results acquired with a standard mid-range pancake coil were preprocessed by using both types of 2-D kernels described in the previous section. To display the outcome of the inverse-filtering scheme, intermediate results with a Lorentzian impulse response are presented at a single frequency. However, for multiparameter data analysis, the code automatically calculates the impulse response parameters for all the available excitation frequencies. A user-

defined segment of the EC trace, typically from the available tube standard, is initially used to calculate these parameters.

Figure 8(a) shows a terrain plot of the original C-scan data from a Type-1 laser-cut specimen (#5528-1-1) containing a single axial notch of length 6.35 mm and nominal OD depth of 80% TW. Figures 8(b) and (c) display the restored signals subsequent to application of the 2-D kernels shown in Figs. 6(a) and (b), respectively. In both cases, the deconvolved signals display better spatial resolution and lower baseline variation. The improvement in spatial resolution could most clearly be observed from comparison of the original and restored response at opposite ends of the axial flaw in which the flaw ends in the deconvolved signal are better defined. This is also reflected in the lissajous trace displayed alongside the terrain plot. Similar improvement in spatial resolution is also expected in the circumferential direction. NDE maximum depth estimates for this sample were 58% by bobbin coil (phase-angle) and 75% by multiparameter analysis of RPC (2.92-mm [0.115-in.] pancake) data.

Figures 9-15 display the results of inverse filtering on the remaining samples from the subset of laser-cut tubes with one or both types of 2-D Lorentzian kernels. In all cases, the restored data show improved spatial resolution and reduction of the baseline level. It is important to note that the primary objective of the proposed deconvolution scheme as a preprocessing tool for multiparameter analysis of EC inspection results is to maximize the separation between crack-like indications and extraneous signals with minimum loss of information from the original data. For all test cases shown here, the results also indicate less ambiguity in the measurement of the phase-angle of restored indications in comparison to those from the original readings. A more detailed description of analyses of EC inspection results using bobbin and +Point™ probes, as well as multiparameter data analysis, was provided in our earlier report.[2]

Test Case Results on Signal Restoration for Laboratory-grown SCC Specimens– Eddy current readings on a collection of 22.2-mm (0.875-in.)-diameter Alloy 600 tubes with laboratory-produced cracking were analyzed by using a multiparameter data analysis scheme described in this report. Flaws in this small set of six samples consisted primarily of OD axial cracking in free-span and circumferential cracking in roll-transition regions, plus a single specimen with axial ID cracking at a dented TSP region. Multiple-frequency NDE data used in this study were acquired with a standard three-coil rotating probe containing a 2.92-mm (0.115-in.) pancake, a mid-range +Point, and 2.03-mm (0.080-in.) high-frequency pancake coil. The primary pancake coil readings were utilized for analyses. The calibration standard contained 18 EDM notches of axial and circumferential orientation originating from the OD and ID of the tube and ranging in depth from 20% to 100% TW. All notches were 6.35 mm (0.25 in.) in length. Data analysis results are presented as an isometric display of relative depth profile for the flawed region of the tube. Estimated profiles are shown both with and without signal restoration by inverse filtering.

Figure 16 shows the normalized depth profile for a specimen with laboratory-grown longitudinal ODSCC. For all test cases, only the portion of tube in the vicinity of the flaw is displayed. In reference to the calibration standard, the maximum flaw depth in the laboratory-

(a)   (b)
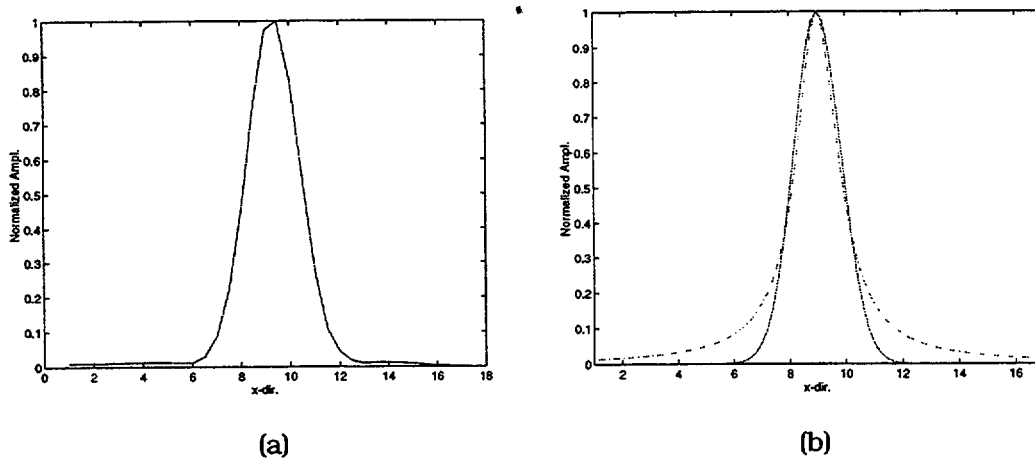
Figure 5.   (a) Typical amplitude response of RPC (2.92-mm [0.115-in.]
            pancake) to 100% TW, 6.35-mm (0.25-in.)–long axial EDM notch
            at 300 kHz and (b) normalized Gaussian [solid line] and
            Lorentzian (dashed line) impulse responses having approximately
            same parameters.

(a)

(b)
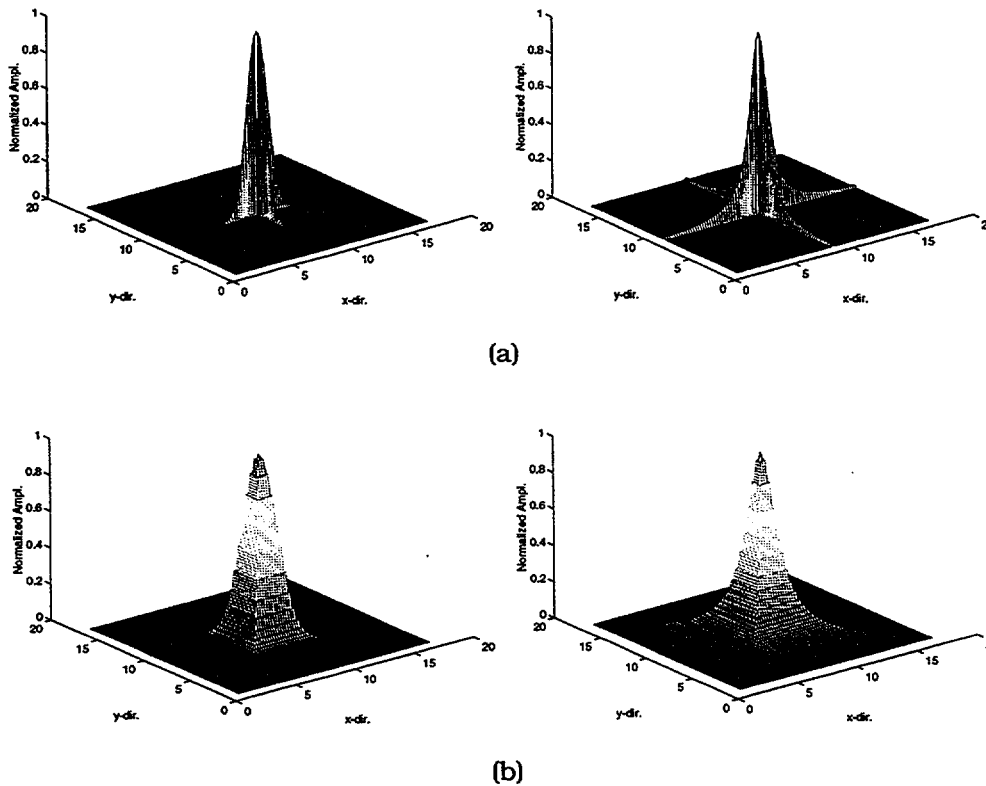
Figure 6.   Spatial domain 2-D kernels for Gaussian (left) and Lorentzian
            (right) impulse responses constructed by (a) two orthogonal 1-D
            functions and (b) rotation of 1-D function about vertical axis.

15
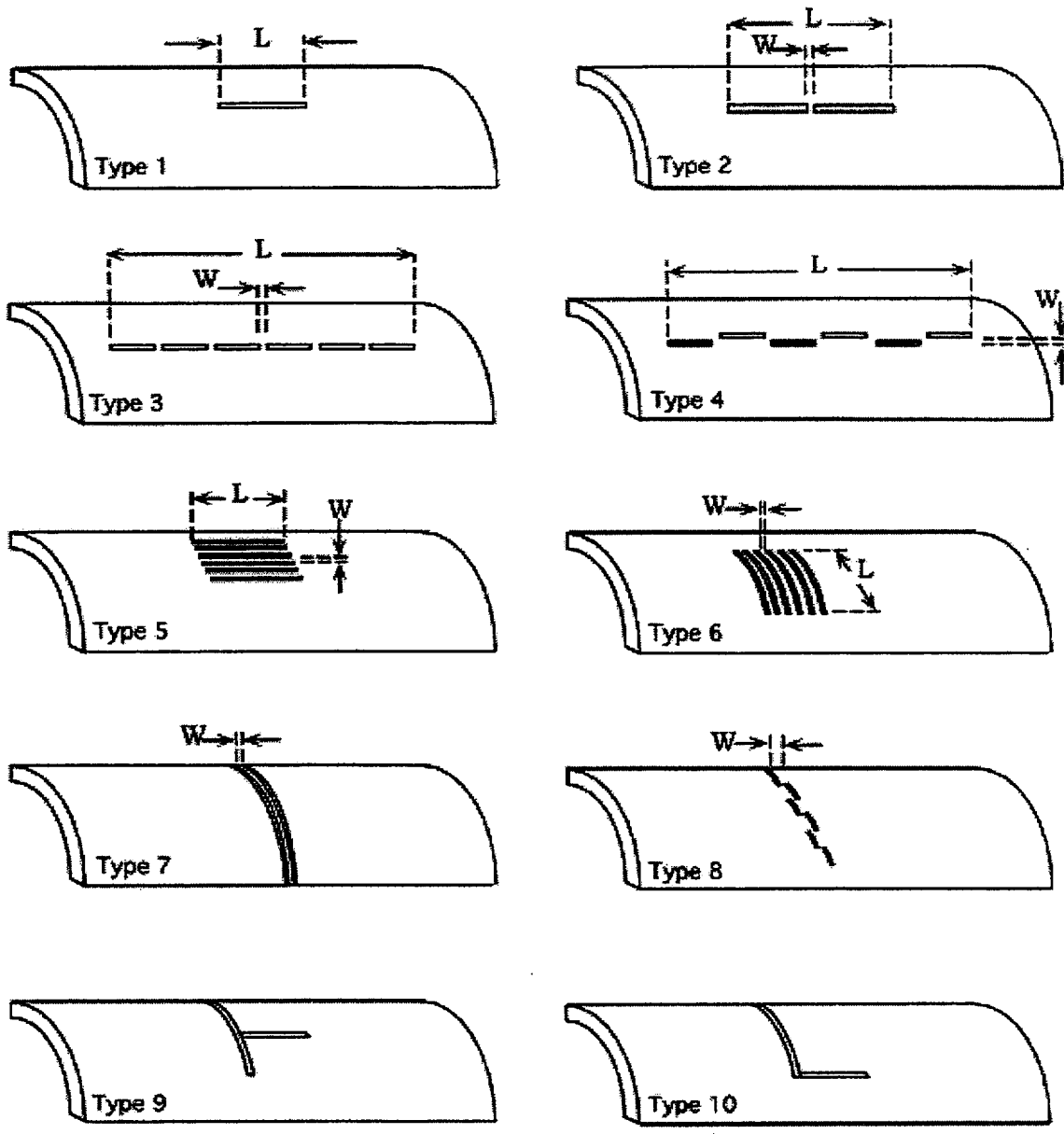
Figure 7. Flaw geometries in set of 24 laser-cut specimens. Flaw dimensions are listed in Table 1.

Table 1. List of all available laser-cut tube specimens and their nominal flaw dimensions.

Tube ID #	Type	No. of Notches	Length (in./deg)	Depth (%TW)	Ligament Width (in.)
5528-1-1	1	1	0.25"	80.00	NA
5528-1-2	1	1	0.25"	80.00	NA
5528-1-3	1	1	0.35"	80.00	NA
5528-1-4	1	1	0.35"	80.00	NA
5528-2-1	1	1	0.5"	80.00	NA
5528-2-2	1	1	0.5"	80.00	NA
5516-4-3	2	2	0.5"	80.00	0.010
5516-4-2	2	2	0.5"	80.00	0.005
5528-3-1	3	6	0.5"	80.00	0.005
5528-3-2	3	6	0.5"	80.00	0.010
5528-3-3	3	6	0.5"	40.00	0.010
5528-3-4	4	6	0.5"	80.00	0.005
5469-2-1	4	6	0.5"	80.00	0.010
5469-2-2	4	6	0.5"	40.00	0.010
5469-2-3	5	6	0.5"	80.00	0.010
5469-2-4	5	6	0.5"	80.00	0.020
5469-3-1	6	6	0.5"	80.00	0.010
5531-3-1	6	6	0.5"	80.00	0.020
5469-3-3	7	2	360°	80.00	0.005
5469-3-4	7	2	360°	80.00	0.010
5469-4-1	8	6	360°	80.00	0.010
5469-4-2	8	6	360°	80.00	0.005
5469-4-3	9	2	180°x0.5"	80.00	NA
5469-4-4	10	2	180°x0.5"	80.00	NA

(a)

(b)

(c)
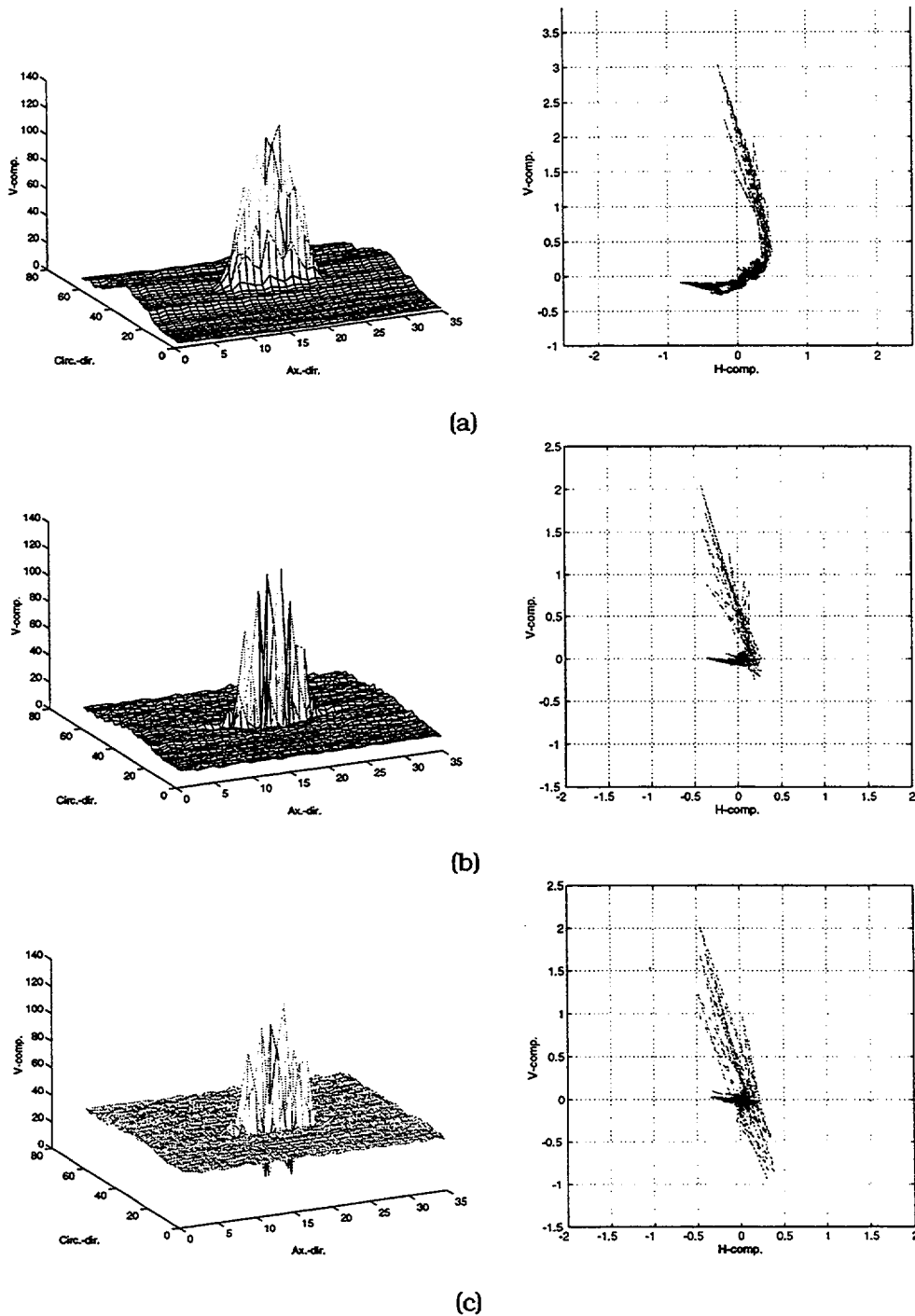
Figure 8. (a) Original and (b)-(c) restored signals with 2-D Lorentzian kernels of Fig. 6 for Type-1 laser-cut specimen #5528-1-1 with nominal OD flaw depth of 80% TW. In both cases, deconvolved signal displays higher spatial resolution and lower baseline variation. NDE maximum depth estimates were 58% by bobbin coil (phase-angle) and 75% by multiparameter analysis of RPC (2.92-mm [0.115-in.] pancake) data.

18
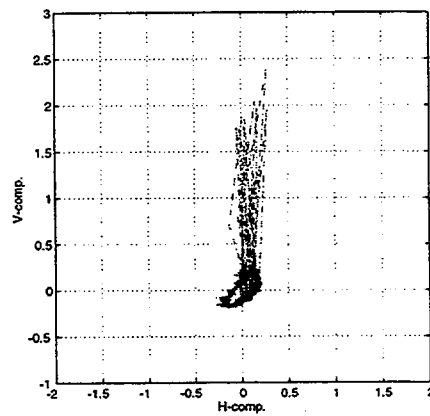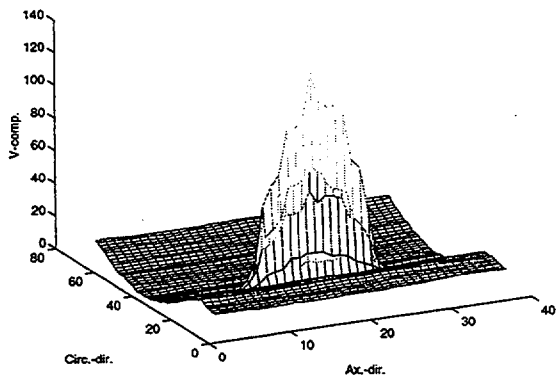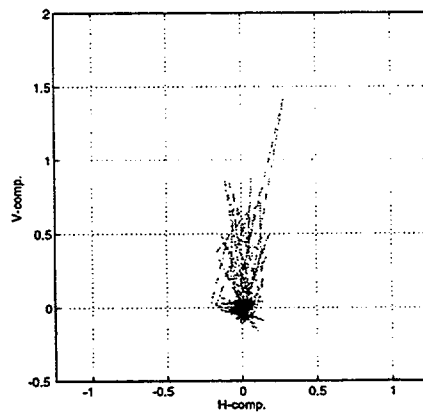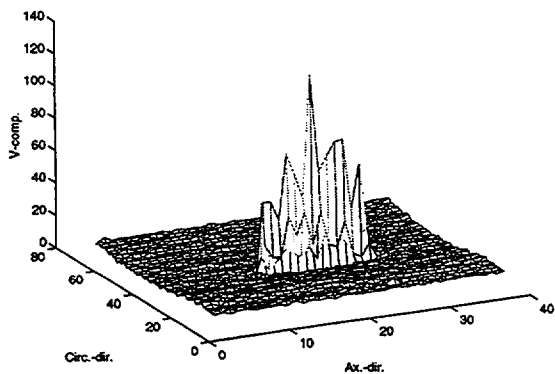
Figure 9.   (a) Original and (b) restored signal for Type-2 laser-cut specimen #5516-4-3 with nominal OD flaw depth of 80% TW.   NDE maximum depth estimates were 35% by bobbin coil (phase-angle) and 72% by multiparameter analysis of RPC (2.92-mm [0.115-in.] pancake) data.
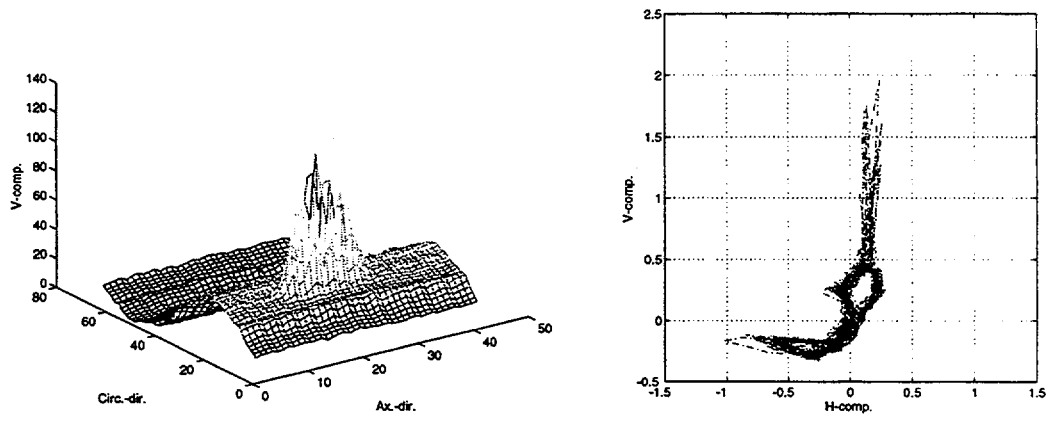
(a)
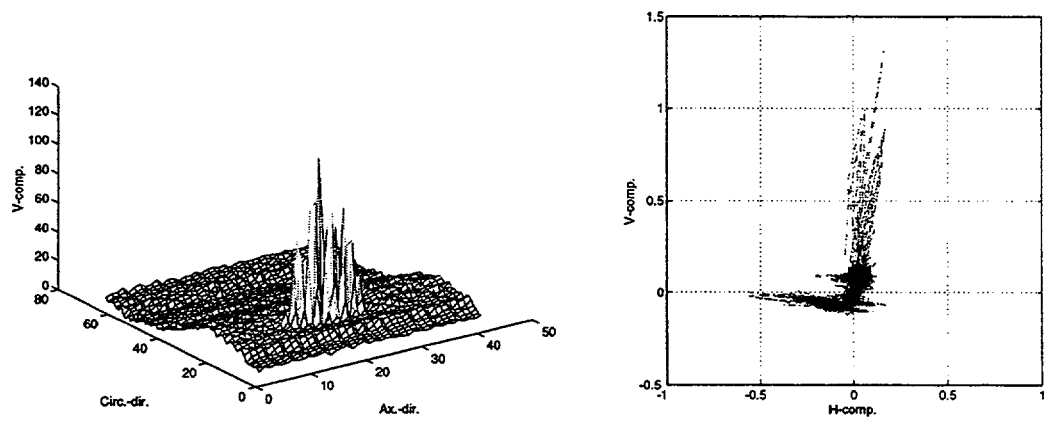
(b)

Figure 10. (a) Original and (b) restored signal for Type-3 laser-cut specimen #5528-3-3 with nominal OD flaw depth of 40% TW. NDE maximum depth estimates were 42% by bobbin coil (phase-angle) and 61% by multiparameter analysis of RPC (2.92-mm [0.115-in.] pancake) data.
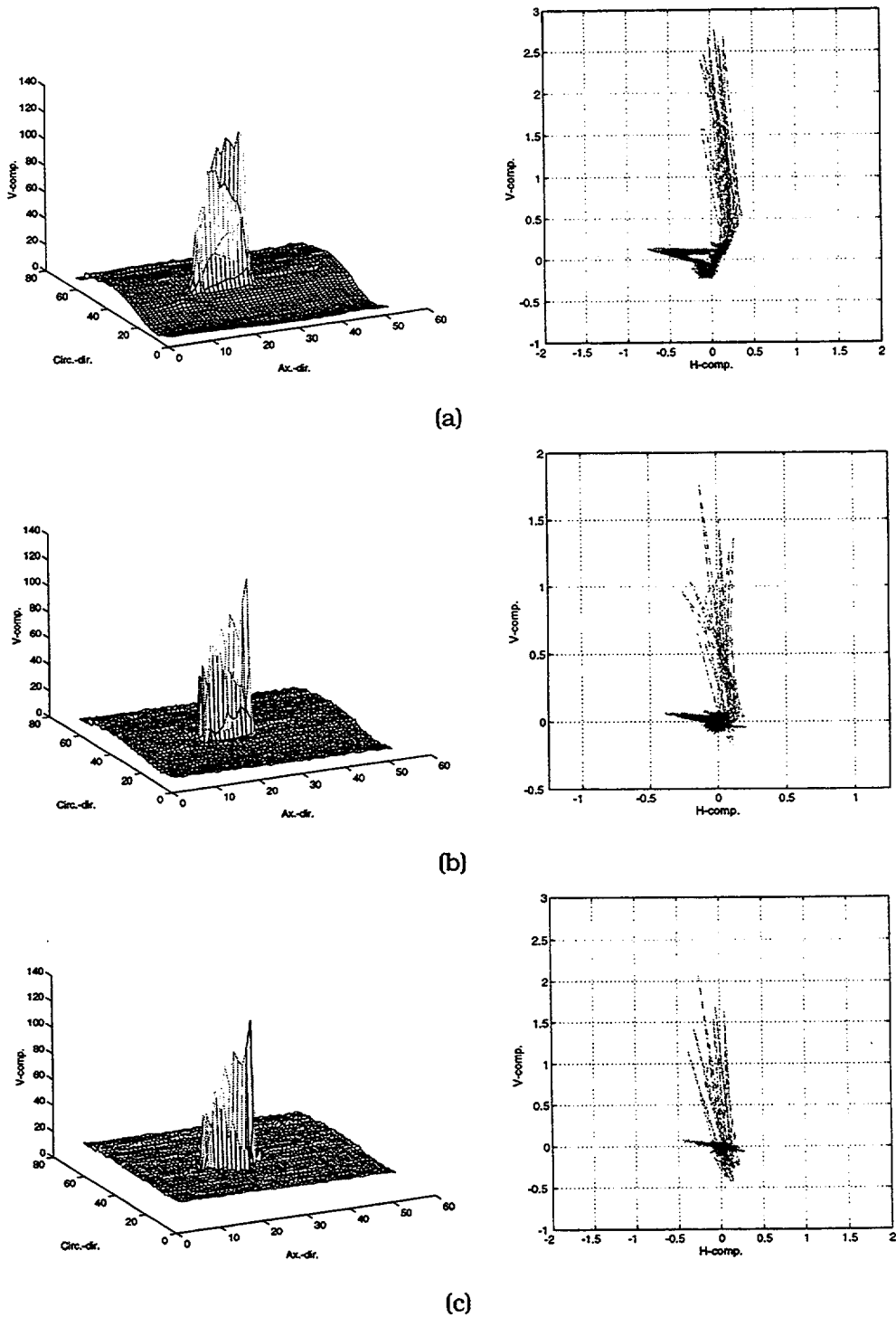
Figure 11. (a) Original and (b)-(c) restored signals with 2-D Lorentzian kernels for Type-4 laser-cut specimen #5469-2-1 with nominal OD flaw depth of 80% TW. NDE maximum depth estimates were 45% by bobbin coil (phase-angle) and 74% by multiparameter analysis of RPC (2.92-mm [0.115-in.] pancake) data.
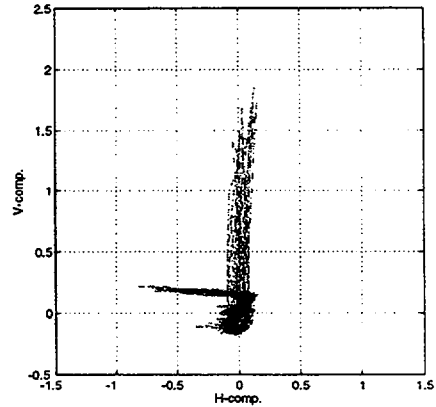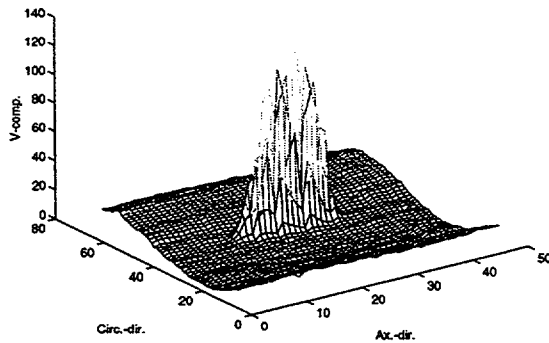
(a)
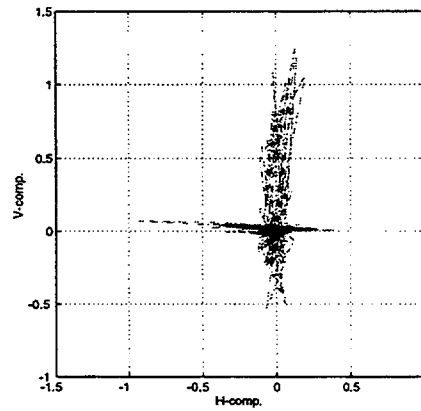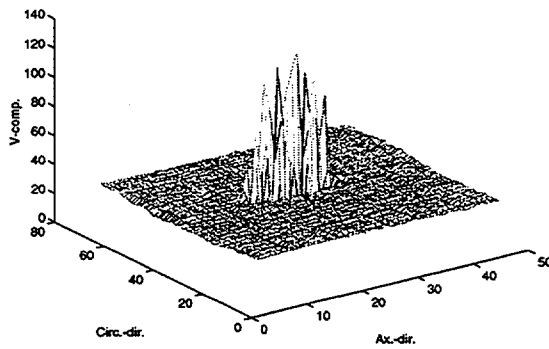
(b)

Figure 12. (a) Original and (b) restored signal for Type-4 laser-cut specimen #5469-2-2 with nominal OD flaw depth of 40% TW. NDE maximum depth estimates were 43% by bobbin coil (phase-angle) and 60% by multiparameter analysis of RPC (2.92-mm [0.115-in.] pancake) data

22
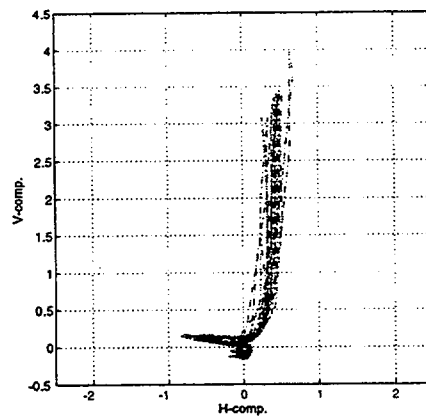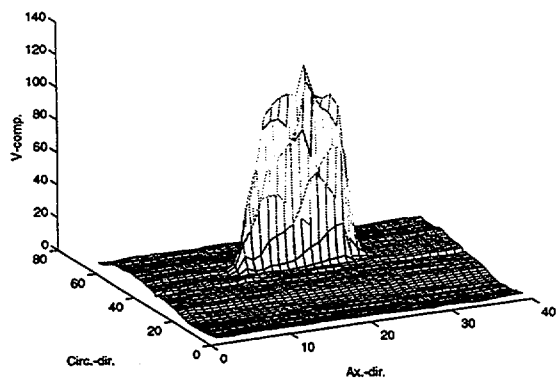
(a)
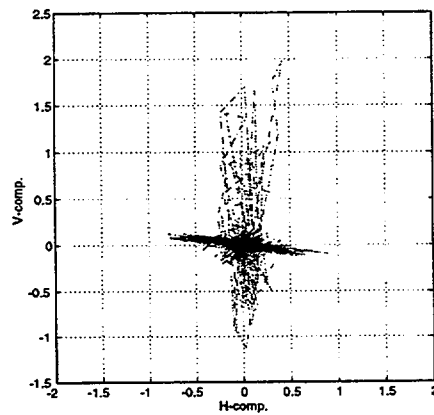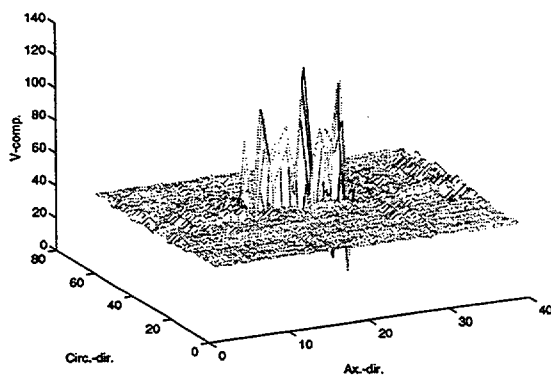
(b)

Figure 13. (a) Original and (b) restored signal for Type-5 laser-cut specimen #5469-2-4 with nominal OD flaw depth of 80% TW. NDE maximum depth estimates were 64% by bobbin coil (phase-angle) and 78% by multiparameter analysis of RPC (2.92-mm [0.115-in.] pancake) data
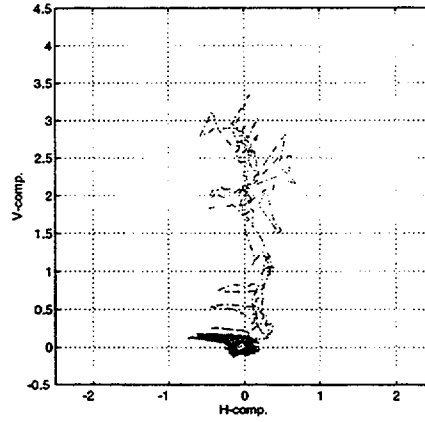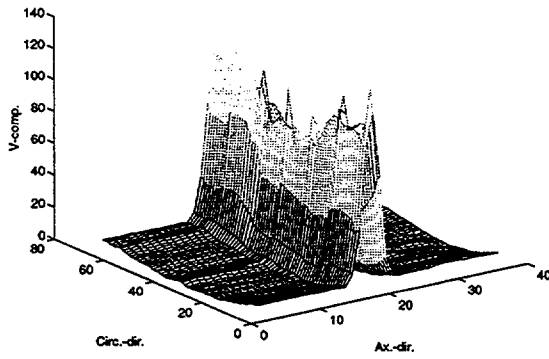
(a)
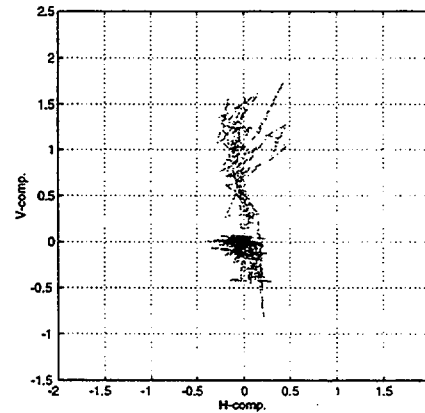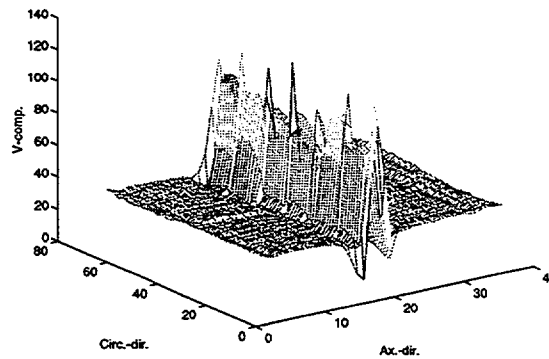
(b)

Figure 14. (a) Original and (b) restored signal for Type-8 laser-cut specimen #5469-4-1 with nominal OD flaw depth of 40% TW. NDE maximum depth estimates were 39% by bobbin coil (phase-angle) and 70% by multiparameter analysis of RPC (2.92-mm [0.115-in.] pancake) data
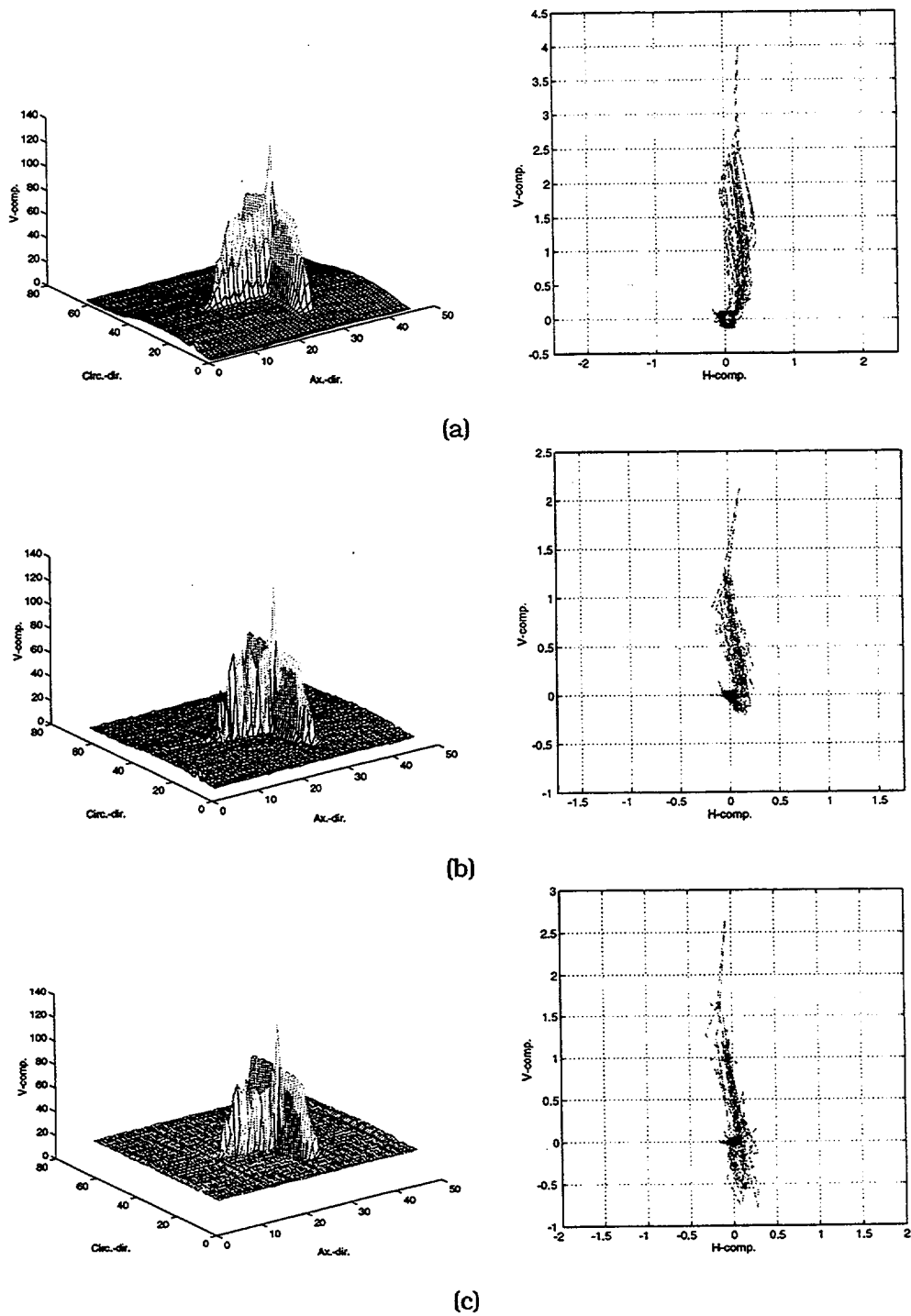
Figure 15. (a) Original and (b)-(c) restored signals with 2-D Lorentzian kernels for Type-9 laser-cut specimen #5469-4-3 with nominal OD flaw depth of 80% TW. NDE maximum depth estimates were 48% by bobbin coil (phase-angle) and 69% by multiparameter analysis of RPC (2.92-mm [0.115-in.] pancake) data.

25

(a)   (b)
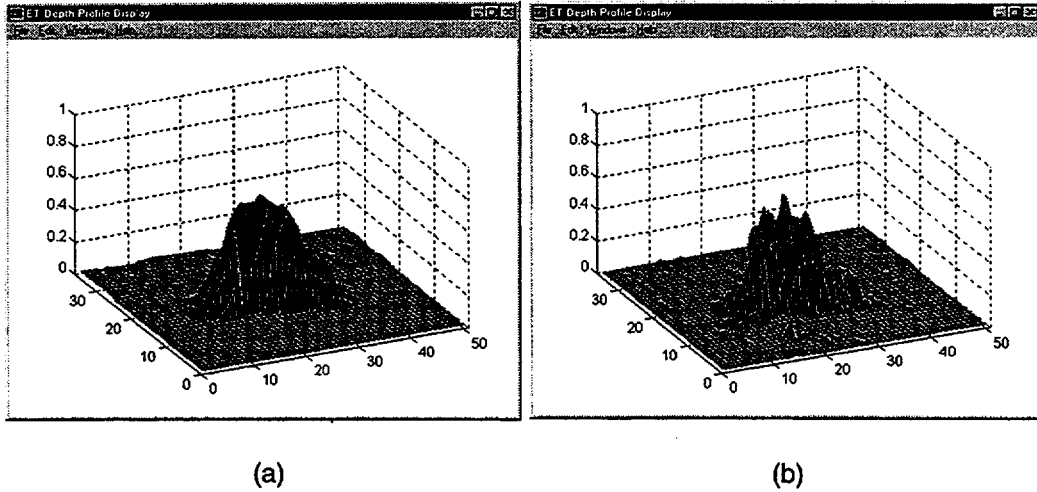
Figure 16. Data analysis results for specimen with laboratory-grown longitudinal ODSCC showing (a) terrain plot of relative OD depth profile for cracked zone and (b) restored profile by inverse filtering. Maximum crack depth is estimated to be >80% TW. Isometric display of results shows finer details in restored profile.

(a)   (b)
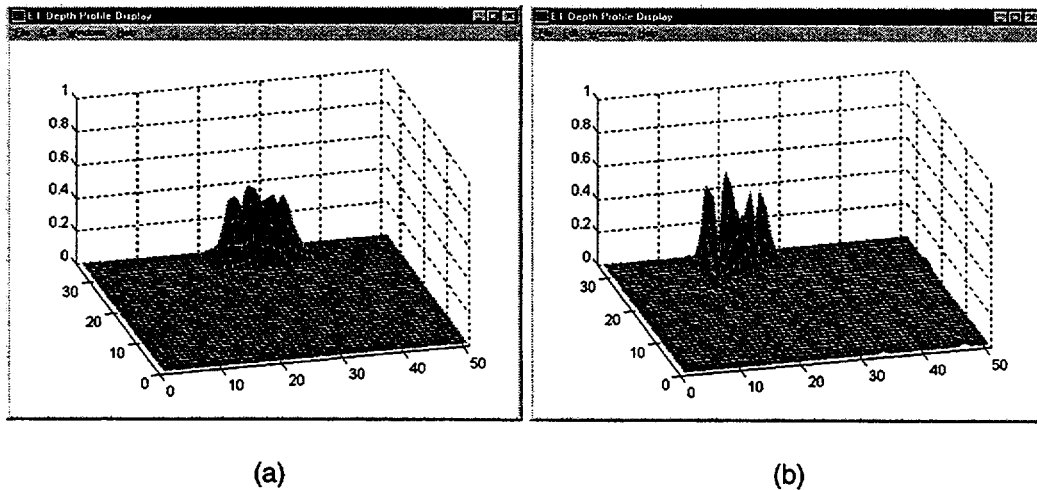
Figure 17. Data analysis results for specimen with laboratory-grown longitudinal ODSCC showing (a) terrain plot of relative OD depth profile for cracked zone and (b) restored profile by inverse filtering. Maximum crack depth is estimated to be ≈80% TW. Isometric display of results shows finer details in restored profile.

grown specimen was estimated to be >80% TW. Figures 16(a) and (b) display, respectively, the estimated 2-D profiles of the flawed segment without and with the deconvolution process being applied. Unlike the gradual tapering of the flaw depth seen in Fig. 16(a), restored depth profile of Fig. 16(b) shows the flaw to have a rather uniform depth in the center, with a sharp drop in depth at the two ends of the crack.

Figure 17 shows the results of analyses for the second axial ODSCC flaw with estimated maximum depth of ≈80% TW. Comparison of the restored depth profile in Fig. 17(b) with that in
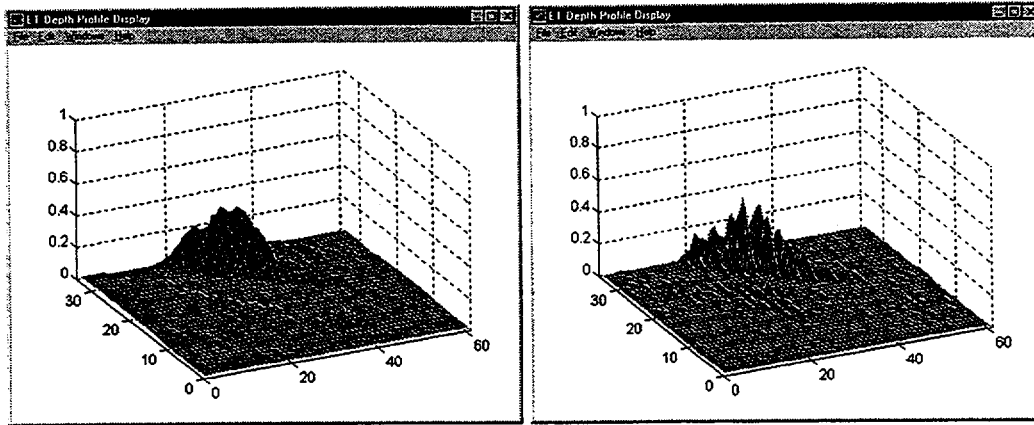
(a)   (b)

Figure 18. Data analysis results for specimen with laboratory-grown skewed ODSCC
showing (a) terrain plot of relative OD depth profile for cracked zone and (b)
restored profile by inverse filtering. Maximum crack depth is estimated to be
≈80% TW. Isometric display of results shows finer details in restored profile.
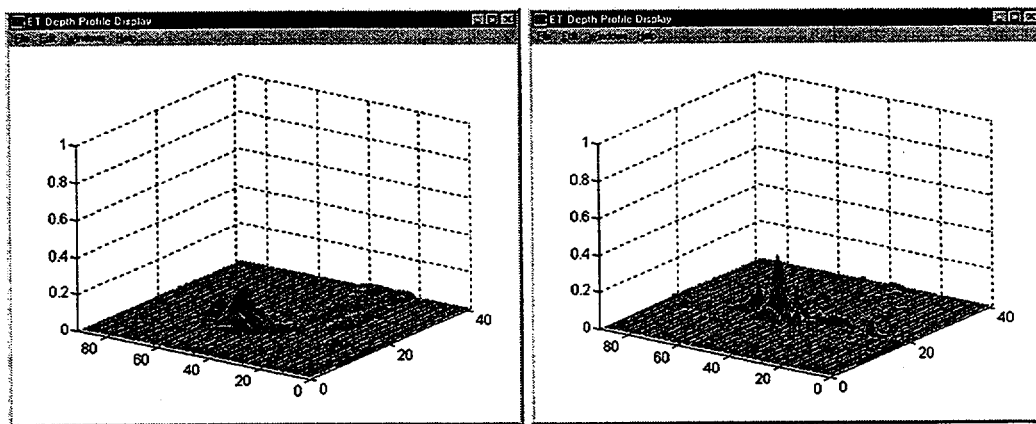
(a)   (b)

Figure 19. Data analysis results for specimen with laboratory-grown circumferential
ODSCC showing (a) terrain plot of relative OD depth profile for cracked zone
and (b) restored profile by inverse filtering. Maximum crack depth is
estimated to be ≈60% TW. Isometric display of results shows finer details in
restored profile.

Fig. 17(a) suggests the crack to be composed of a series of axial segments with the one segment being nearly separated from the rest. Similar results are shown in Fig. 18 for another specimen with an axial ODSCC flaw. Terrain plots of the depth profile, however, suggest the orientation of the crack to be approximately at 45° with respect to the tube axis. Maximum flaw depth in this case was estimated to be ≈80% TW.

Figures 19 and 20 show the results of analyses for two specimens with circumferential ODSCC at the roll-transition region of the tube. The processed data clearly indicates complete suppression of the roll-transition that is the primary signal feature in the amplitude trace. The

27

(a)   (b)
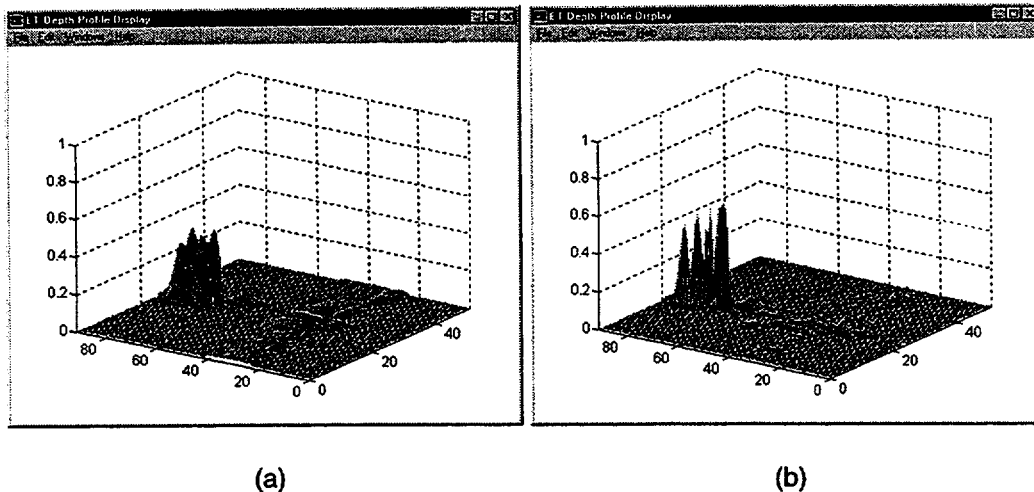
Figure 20. Data analysis results for specimen with laboratory-grown circumferential ODSCC showing (a) terrain plot of relative OD depth profile for cracked zone and (b) restored profile by inverse filtering. Maximum crack depth is estimated to be ≈80% TW. Isometric display of results shows finer details in restored profile.

maximum flaw depths were estimated to be ≈60% and ≈80% TW, respectively. Based on the terrain plots in Figs. 19(a) and 20(a), both cracks extend nearly 120° around the circumference. The depth profiles of the restored signals shown in Figs. 19(b) and 20(b) suggest both circumferential cracks to be composed of multiple segments. The maximum depth of the flaw displayed in Fig. 19(b) appears to be near the center. Terrain plotting of the estimated depth for the restored signal in Fig. 20(b), however, suggests that the circumferential crack consists of four closely spaced short segments with comparable maximum depths.

Finally, Fig. 21 shows the results of analysis for an ID axial crack in a dented region at the tube support plate intersection. The maximum flaw depth was predicted to be ≈40% TW. In this case, a terrain plot of the defected segment was constructed from the estimated ID profile. Comparing the restored profile of Fig. 21(b) with that of 21(a) indicates some improvement of spatial resolution following signal restoration. Once again, complete suppression of the TSP and dent signals is clearly evident in both cases.

2.4 Multiparameter Data Analysis

Multivariate data analysis algorithms serve as the foundation for various operations for the processing of EC data. Both regression and factor-based techniques fit into this category of data manipulation. More prominent areas of application to EC ISI data are in algorithms used for suppression of unwanted signals and in predictive models that attempt to correlate NDE parameters to single or multiple independent variables such as flaw size or tube structural integrity. Three separate algorithms were investigated earlier in this program and have been adapted for use in various areas of research associated with the EC testing of SG tubing. They consisted of multiple linear regression (MLR), principal component regression (PCR), and partial least squares (PLS) techniques. Conventional least-squares-based regression has been used primarily in standard artifact suppression schemes, commonly referred to as mixing algorithms. The more versatile PLS algorithm has been used in a wider range of applications, including more
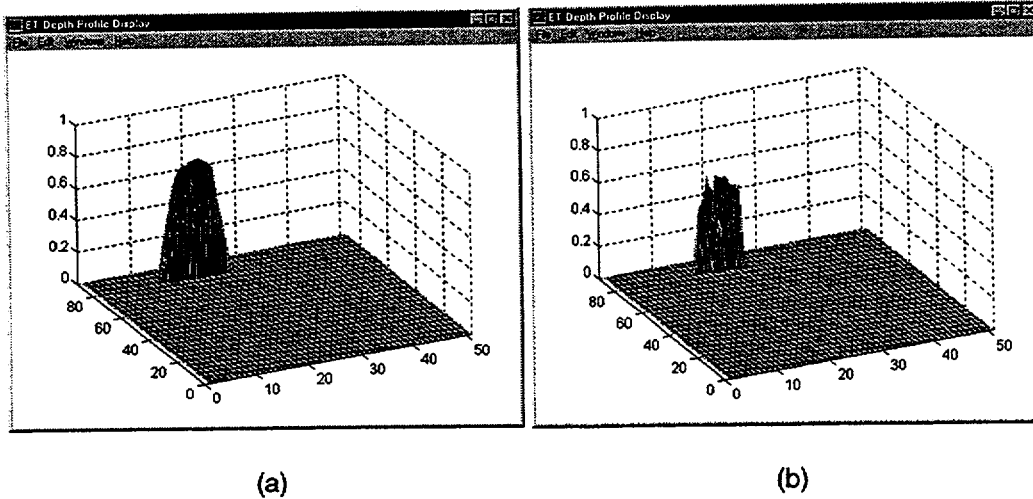
Figure 21. *Data analysis results for specimen with laboratory-grown longitudinal IDSCC at dented TSP intersection showing (a) terrain plot of relative ID depth profile for cracked zone and (b) restored profile by inverse filtering. Maximum crack depth is estimated to be <40% TW. Isometric display of results shows finer details in restored profile.*

sophisticated suppression schemes and predictive models. A brief description of these techniques is presented next.

2.4.1 Least Squares Regression and Factor-Based Techniques

Multivariate analysis techniques are often utilized to explore unknown trends in large quantities of data. The two basic stages in such analyses are generally referred to as calibration and prediction. In the calibration stage, a data matrix is constructed from the probe response at various time or frequency slots for a given set of calibration samples. The calibration phase produces a model that relates the probe response to known values of the parameters to be estimated. In the prediction stage, the matrix of coefficients and weights that describes the system response (input-output relationships) is used to estimate the parameters of interest in new measurement test sets. Of the three multivariate techniques, MLR (an extension of the ordinary least squares algorithm) is used most frequently. Having the response matrix [X] and the parameter matrix [Y], MLR develops a linear combination of variables in [X] that minimizes the errors in reproducing [Y]. This is accomplished by constructing a relationship between [X] and [Y] such that

$$[Y] = [X][b] + [E], \tag{12}$$

where [β] is the matrix of regression coefficients and [E] is the matrix of errors associated with the MLR model. The matrix [β] is found by linear regression to minimize the difference between the true and estimated elements of the parameter matrix in a least-squares sense as

$$[E] = \sum_{n=1}^{N} \sum_{m=1}^{M} \left(y_{mn} - \hat{y}_{mn} \right)^2 = \sum_{n=1}^{N} \sum_{m=1}^{M} e_{mn}^2. \tag{13}$$

29

The MLR approach is often a good choice when dealing with linear systems that are described as exhibiting linear response, low noise, no interference, and no colinearities. MLR attempts to use all of the available information in the independent variable matrix for model construction. Both relevant (signal) and irrelevant (noise) information will be weighted equally by this method when input-output relations are constructed. To overcome this limitation, the two factor-based techniques (PCR and PLS) have also been examined. The factors are linear combinations of the original variables. Factor-based models attempt to use a minimal set of factors that best describe the true relationship between the independent and dependent variable matrix. Because factor-based models do not attempt to directly invert the covariance matrix, potential colinearities in data could be accommodated without causing singularities.

PLS was chosen to construct a multivariate regression model for the EC data. For the PLS algorithm, a general model would consist of a regression between the scores of the relationships for the dependent variable [Y] and independent variable [X]. The outer relationships can be written in matrix form as

$$[X] = [T][P] + [E] = \sum_{n=1}^{N} t_n p_n + [E] \tag{14a}$$

$$[Y] = [U][Q] + [F] = \sum_{n=1}^{N} u_n q_n + [F], \tag{14b}$$

with the inner relation defined by

$$\hat{u} = b_n t_n, \tag{14c}$$

where [T], [U], [P], and [Q] are the eigenvectors and eigenvalue matrices and [B] is the vector that contains the inner relationships. The principal components are simultaneously calculated for both blocks. The intention is to minimize $\|F\|$ (i.e., $Norm\{[F]\}$), and hence to construct a useful relationship between [X] and [Y].

2.4.2 Multifrequency Mixing Techniques

Processed channel information from multiparameter mixing is commonly utilized in analyzing multifrequency EC inspection data. So-called mixing techniques, originally implemented electronically on analog signals by using rotation, scaling, and subtraction, were devised to enhance detection of EC signals of interest by suppressing the effect of unwanted signals such as background fluctuations and artifacts. Conventional digital mixing techniques use multifrequency signal components from two (or more) channels to construct a new mix channel based on known artifacts (signal to be suppressed) on a calibration standard tube. Mix frequencies are chosen so as to provide independent information on the signal to be eliminated. Current mix algorithms generally use a linear least squares method in which the output (mix channel) signal is a weighted linear combination of horizontal and vertical components of input signal components at different frequencies. Because independent mix coefficients can be calculated for each signal to be suppressed (often based on simulated artifacts on a calibration standard), in theory an unwanted signal could be eliminated by successive implementation of different sets of mix coefficients. However, except under ideal conditions, the mix signal will

always contain residual signals from unwanted artifacts. This could in part be attributed to background fluctuations as well as material and geometrical differences between the simulated and actual artifacts. Furthermore, variation in the probe's field of view (i.e., spread of the induced field) at different frequencies could also contribute to a nonzero mix residue. It is important to note that the mixing process could affect to different degrees both the amplitude and phase of the signal from defects of interest.

Recovery of defect-induced signals in the presence of strong background interference is an important and often challenging NDE problem when analyzing NDE results for ISI of SG tubing. Data analysis is further complicated when degradations are accompanied by tube ID variations such as design-related tube diameter changes or the presence of significant denting. These difficulties are associated with such factors as low S/N ratio and small phase separation between ID and deep OD indications. Multifrequency mixing is routinely applied to improve detection of flaw signals that are obscured by tubing artifacts. However, the mix channel information should be analyzed discerningly, particularly when more than two frequencies are used in the process. Conventional two-frequency least-squares (LS)-based mix algorithms that are optimized primarily to suppress a single OD artifact generally provide consistent outcomes. On the other hand, processed channel information from mixing algorithms that incorporate more than two frequencies could be unreliable for the interpretation of signals outside the segment where the mix coefficients were calculated. This is due in part to uneven perturbation of the signal amplitude and phase information that is introduced by higher-order (nonlinear) mix models. This issue is of particular importance when dealing with rotating probe data.

Direct (independent) and indirect (dependent) mixing algorithms, for suppressing multiple unwanted indications from composite signals have also been examined. In an indirect mix, regression coefficients are determined by using a data segment from a simulated artifact such as a TSP ring on a reference standard tube, which is expected to closely resemble those present in the actual SGs. The aim of the regression model is to best reproduce the primary/base frequency signal by combining signal components from auxiliary frequency channel(s). This is the conventional approach used for the analysis of EC ISI results. Alternatively, independent mix procedures have the potential to suppress unwanted signals by using multiple-frequency readings on the same tube. This approach, primarily suggested for suppression of dominant signal features, is of particular interest when tube standards with simulated artifacts that resemble field-induced signals are not readily available.

Various two- and three-frequency regression fits have been implemented at ANL. Preliminary results indicated that two-frequency mixes are generally more consistent, so the approach was to sequentially apply two-frequency mixes for suppression of two unwanted indications at the same axial location. To improve the mix outcome, several modifications were made to our previously developed standard mix algorithm. These consisted of energy-scaling each trace, resampling in frequency domain, and phase-angle referencing. Frequency resampling was done to increase the number of available independent variables. Phase-angle tracking was done to help reduce phase ambiguity from multiple application of linear regression coefficients. Based on cases tested so far, the amplitude renormalization consistently exhibited improved quality of mix outputs. This is believed to be a result of the weighting introduced by the energy-scaling process.

2.4.3   2-D Suppression of Unwanted Signals

Test case results are presented here from an investigation on the application of signal decomposition and factor analysis techniques for selective suppression of unwanted indications from rotating-probe data.   Initial studies suggest that 2-D multiple-frequency factor-based techniques could provide substantial improvement over conventional 1-D mix procedures for analysis of rotating-probe EC inspection results.   Preliminary evaluations of the two techniques discussed here was based on analyses of simulated composite signals from a rotating-probe that were produced from the available readings on a calibration standard.

Conventional regression-based mix algorithms were initially developed to aid in suppression of unwanted signals (e.g., external support structures and, to a lesser extent, tube dimensional variations) from EC signals. Multifrequency mix procedures that typically involve combining the information from a primary/base frequency and one or two auxiliary frequency channels have been fairly effective for the processing of bobbin coil readings.   However, independent evaluations at ANL suggest that 1-D mix algorithms are not as effective for the processing of higher-resolution rotating-probe inspection results.   In particular, unlike the situation for the bobbin coil, mixes for rotating-probe C-scan data are quite subtle and routinely fail to produce consistent outcomes.   Also, when mix coefficients are applied to the entire signal trace, significant distortion of both the amplitude and phase-angle information of the original readings could result. The nature of instability of traditional mix schemes for the processing of rotating-probe data becomes somewhat apparent when one compares a 1-D bobbin coil signal (i.e., each measurement point along the tube axis is an integration of coil response over the circumference) with 2-D readings (i.e., measurements along both axial and circumferential directions) from a rotating probe. To improve rotating-probe mixes, specially designed simulated TSP rings (e.g., a 270° ring as opposed to an axisymmetric 360° ring used for bobbin mixes) are often utilized.   Nevertheless, the mix results could vary substantially, depending on the selected portion of signal for the calculation of mix coefficients. For this reason, mix channel information is not currently used for reporting rotating-probe inspection results.

A study was initiated at ANL to evaluate potential alternatives to 1-D conventional mix procedures for RPC data.   Two approaches based on 2-D factor analysis techniques were considered.   Both methods utilize spectral decomposition, also referred to as singular value decomposition (SVD) or outer product expansion. However, they differ significantly in their analysis of factors.   The first method is based on a standard decomposition at a single-frequency and subsequent selection of appropriate coefficients. The second method, on the other hand, uses a least-squares (LS) regression approach with two frequencies.

Spectral decomposition methods serve as the fundamental numerical technique in a wide range of applications from solution of linear system of equations to problems in signal and image processing such as restoration, compression, denoising, pattern recognition, and feature extraction.   Such transformation algorithms basically attempt to decompose an often ill-conditioned data matrix to an outer product expansion of left- and right-hand unitary matrices of orthonormal eigenvectors with a matrix of pseudo-eigenvalues. With the underlying assumption that the basis functions that span the signal and noise subspaces are orthogonal, this mapping should then provide improved separation of relevant signal features from inconsequential trends. Following the decomposition, selection of appropriate factors allows for the preservation of relevant signal features and in effect elimination of background noise.

Factor analysis methods that use spectral decomposition together with multivariate regression schemes offer a more robust method for the analysis of factors through recursive regression between the independent and dependent variable matrices. The basic formulation of LS-based factor analysis method used here for the processing of rotating probe data was described earlier in this report.

In practice, selection of appropriate factors often poses the greatest challenge when spectral decomposition alone is used. This is particularly true for the EC inspection results with rotating probes in which flaw and artifacts at one frequency are often described by common factors. This means that it is not always possible to select a set of factors that reasonably separate consequential indications from artifacts and background fluctuations. Therefore, factors cannot be applied blindly, and some form of discretion is necessary in deciding which factors to keep. For this reason, the multiple-frequency LS-based factor analysis method should provide a more robust and systematic approach to suppression of unwanted signals in rotating-probe data.

The two approaches that were described above, namely, single-frequency spectral decomposition and a two-frequency decomposition with LS-based regression, were initially tested on simulated composite signals from RPC readings on a 22.2-mm (7/8-in.)-OD tube standard with machined notches and a 270° support plate slip ring. Various combinations of OD and ID notches within the TSP region were produced. This was done by vectorial addition of data segments with notches at various frequencies with that from the TSP segment. It is worth noting that the nonaxisymmeteric geometry of the TSP ring used here poses a greater challenge to any signal suppression scheme than do axisymmetric drilled support plates. However, it is expected that such nonuniform and overwhelming EC indications could be encountered in the field from external structures such as broached support plates.

Initial results on the suppression of TSP indication at a single frequency by using a standard SVD algorithm did not produce acceptable results. Specifically, in several test cases a reasonable degree of suppression of TSP indications introduced substantial degradation of the flaw signal. As mentioned earlier, the primary limitation of this method arises from the lack of separation of factors that describe artifact and flaw signals.

With the same simulated data, the two-frequency LS-based factor analysis method described in Sec. 2.4.1, on the other hand, rendered a systematic approach for repeatable suppression of TSP indications with acceptable degradation of flaw signals. Figures 22 and 23 show the results for two test cases by using the composite signal described above. In both cases, single and multiple flaws that were arbitrarily placed within the TSP region were recovered with a high level of suppression of TSP indications. Selection of primary and auxiliary frequencies for 2-D suppression is analogous to that used by standard 1-D mix procedures. Also, in a similar manner to conventional mix procedures, multiple unwanted indications could be suppressed by successive application of this method. Further studies in this area will be carried out by using specimens with laboratory-produced flaws and with various forms of simulated artifacts.
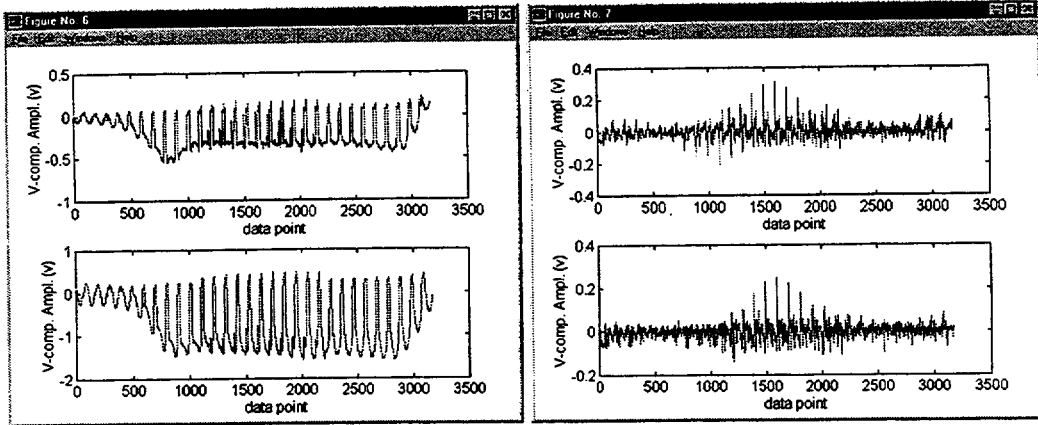
(a)   (b)

Figure 22. Demonstration of 2-D signal suppression on RPC traces of (a) simulated raw
data at 400 kHz (top) and 200 kHz (bottom) frequencies composed of a 40% TW
axial OD notch at an arbitrarily selected location within a 270° tube support
ring and (b) processed data using 400 kHz primary and 200 kHz auxiliary
frequency (top) and 300 kHz primary and 100 kHz auxiliary frequency (bottom).
In both cases, the processed data indicate substantial improvement of S/N ratio
over original readings.
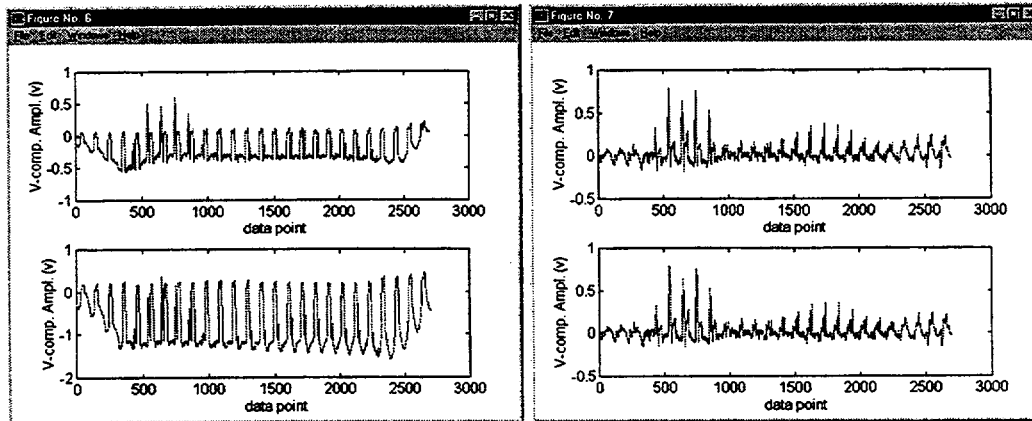
(a)   (b)

(b)

Figure 23. Demonstration of 2-D signal suppression on RPC traces of (a) simulated raw
data at 400 kHz (top) and 200 kHz (bottom) frequencies composed of a 40% TW
axial OD and 40% TW circumferential ID notch at arbitrarily selected locations
within a 270° tube support ring and (b) processed data using 400 kHz primary
and 200 kHz auxiliary frequency (top) and 300 kHz primary and 100 kHz
auxiliary frequency (bottom). In both cases, the processed data indicates
substantial improvement of S/N ratio over the original data.

2.4.4 Multivariate Analysis for Estimation of NDE Profile

Multivariate analysis is also used in the final stage of data analysis (shown in block 5 of Fig. 1) for estimation of the depth profile of a test section. Processed data from multiple channels is simultaneously used to construct a model that correlates the NDE results to flaw size and origin. In reference to Eqs. 14(a) and (b), dependent variables in this case consist of phase angle information at multiple frequencies. The independent variables are flaw size and origin. Eddy current measurement on a calibration standard tube is used for the determination of regression coefficients.

Reliability of any predictive correlation depends heavily on the calibration data used to construct that model. Both the range and composition of training data play crucial roles. In regard to the analysis of EC data, this translates to the composition of the available range of flaw size, type, and origin in the calibration standard tube. In addition, availability of a useful set of frequencies is of outmost importance. Studies have been carried out at ANL to determine the sizing accuracy based on the available number of channels. With a minimum of two frequencies required for constructing a two-parameter model, assessments so far suggest that the combined information from three frequencies generally produces more consistent results. Although, incorporation of a larger number of channels is also feasible, acquiring rotating probe data at a greater number of frequencies is generally prohibitive for practical ISI applications.

2.5 Rule-Based Flaw Identification

Eddy current testing of conducting materials is intrinsically a relative technique, unlike some conventional NDE methods for which absolute-type measurements are possible. Calibration of data with respect to known artificial signals in a tube standard that closely resemble field-induced degradations and artifacts is necessary in order to allow discrimination and quantitative characterization of consequential indications. Once EC readings at multiple frequencies are calibrated, the behavior of signals, typically extracted from their impedance plane trajectory, can be utilized for their characterization. The two most fundamental features that are attainable from the impedance plane are the changes in signal amplitude and phase as a function of frequency.

In conventional eddy current data analysis of SG tubing, human analysts are trained to recognize flaw-induced signals from artifacts by selective application of a series of rules once potential flawed regions are visually detected. Aside from well-defined rules for interpretation of signal behavior from traditional forms of tubing damage, empirical rules are also systematically applied that are founded on past experience and historical lessons learned in dealing with similar SG units. Complexity, origin, and location of indications in an SG are typical markers for detection of such flaws.

As stated above, conventional rules for identification of flaws are based on changes in the signal amplitude and phase angle among the primary and auxiliary channels. Variation of the signal level as a function of frequency can be used to identify flaws from artifacts. Artifacts would include any inconsequential indication such as tube deformation or geometry changes (e.g., dents, roll-transitions, and U-bend ovalization), conducting and ferromagnetic deposits (e.g., sludge, magnetite, and copper deposits), and tube support structures (e.g., tube sheet and tube support plates). As a direct consequence of the skin depth, or the characteristic depth of

35

penetration, the decay of eddy currents inside a conducting medium produces a sharper drop in the amplitude of OD-originated flaws than of ID indications, as frequency is decreased. Stronger attenuation of signals within the tube wall also renders the detection of OD indications more difficult. The larger phase lag from OD indications also results in a higher degree of phase rotation for OD-initiated indications. Depending on the calibration procedure that is in place for ISI of thin-wall SG tubing, clockwise (CW) and counter-clockwise (CCW) rotation of the impedance plane signal trajectory is commonly used to determine the flaw origin. For instance, adjusting of the phase angle at all frequencies from a TW flaw to a fixed value results in indications of OD origin to exhibit CCW rotations and those of ID origin having a smaller CW rotation. Likewise, information at lower frequencies can be utilized to more effectively distinguish OD deposits and permeability variations.

Analogous to the manual analysis of EC inspection data, characteristic behavior of EC signals as a function of frequency can be utilized in computer-aided data analysis algorithms. Because all available information is indiscriminately examined, such algorithms allow more effective identification of subtle forms of degradation. Computer-based algorithms that imitate some form of human decision making process are generally labeled as expert systems.

Automated identification of flaws and their origin is performed through implementation of a series of rules that are applied to the pre-processed multiple frequency NDE results. This intermediate stage of data analysis is shown in block 4 of Fig. 1. Rules are coded as a series of conditional statements (i.e., IF-THEN) that are sequentially applied to the selected data segments. Calculation of S/N from the earlier stages of the analysis is used to set the minimum threshold for sorting of signals that are to be examined. Combined amplitude and phase-based rules are implemented to better discriminate between potential flaws and noise. Rules that are currently in place are set to be generally conservative for identification of flawed regions of the tube. As a tradeoff between conservatism and sensitivity, they can be adjusted to some degree based on the value of S/N for a particular test section. The current set of rules is fixed for a specific coil configuration and range of frequency. Efforts are currently underway to facilitate semi-automated implementation of rules to more effectively deal with the expected variability in ISI data acquisition procedures. With the expansion of the NDE data base at ANL, it is expected that lessons learned from examination of a wider range of SG tubing degradations will aid modification and upgrading of the current set of rules as necessary.

2.6 Data Quality Issue

As it was noted earlier, eddy current testing is a comparative NDE method. Success of this technique is highly dependent on the consistency of data acquisition parameters and proper calibration results. Although the quality of data affects both detection and sizing, this issue is of particular concern when quantitative estimates of flaw size are to be determined. Any compromise in the setup of the instrumentation and the calibration procedures that are in place could affect the quality of NDE data and in turn the final analysis of results. Minimum requirements for acceptable data acquisition parameters are well documented in various EPRI examination technique specification sheets and NRC generic letters for ISI of SG tubing. These guidelines generally define the instrumentation setup (coil excitation frequencies, gain setting, cable length, sampling rate, probe speed, etc.) and calibration procedures to achieve a certain probability of detection (POD) for a given probe (e.g., bobbin, rotating, and array probes). With only a handful of techniques being qualified for sizing of particular forms of SG tubing damage,

these techniques are primarily aimed at ensuring attainment of a certain POD. The data quality issue has recently gained much attention, particularly in connection with the use of rotating probes for estimation of flaw size. Efforts are being made by the industry to define a suitable set of parameters that could be used to ascertain the appropriateness of data quality. One such parameter is the S/N for a particular section of SG tubing. Because initial detection of potential flaw signals during manual analysis of EC data is based on visual identification, defining of a particular value or range of values for the S/N may seem appropriate for manual analysis for the purpose of detection. However, in regard to sizing of flaws, manual or automated, the term S/N carries a much broader connotation. The quality of data that may seem appropriate for the purpose of detection may not meet the requirements for reliable estimation of the flaw size.

Automated data analysis algorithms that are intended for sizing of a wide range of damage mechanisms rely on strict adherence to some minimum requirements for the quality of EC inspection data. Detection probability of automated algorithms that incorporate signal conditioning schemes, in general, is less affected by the signal amplitude (i.e., S/N). However, unlike conventional manual analysis, aimed primarily at conservative detection of flaws, in which a certain level of compromise in data quality could be accommodated, rule-based automated techniques for sizing of flaws are more sensitive to data variability. For instance, degradation of S/N arising from baseline fluctuations and semiperiodic signals from tube deformations that could significantly reduce visual flaw identification can be generally dealt with by numerical processing of data. On the other hand, degradation of S/N in the form of acquisition-related corruption of data and insufficient sampling rate that may not substantially affect detection may significantly influence the sizing results. Recovery of signal peaks in a digitized data stream is governed by the Nyquist sampling rate that was mentioned earlier in this report. The relationship between sample interval Δx, and maximum observable frequency f_{max} according to the Nyquist theorem is given by

$$f_{max} = \frac{1}{2\mathrm{D}x} \cdot \qquad (15)$$

For rotating probes, sufficient sampling rates should be acquired in both axial and circumferential directions in accordance with the rotational and push/pull speed of the probe. Although lack of sampling can be remedied to some degree through interpolation of the data, significant undersampling will always result in loss of information. Other factors that are crucial to successful operation of automated data analysis schemes are the availability of data at appropriate set of frequencies and proper calibration standards. Importance of these factors was described earlier in connection with rule-based identification and multivariate sizing algorithms.

3 Data Analysis Results

NDE results from machined flaws and laboratory-produced specimens have been utilized in various studies for the evaluation and refinement of algorithms that have been implemented at ANL. Data analysis results using the multiparameter algorithm described in this report are presented next on several samples from separate batches of tubes with chemically induced cracking. Selected test cases are initially provided to demonstrate the level of resolution enhancement that is achievable through processing of standard rotating probe data. Subsequently, analysis results are presented on representative samples from three separate batches of laboratory-grown specimens. Flaw types in these tubes are representative of those incorporated into the ANL tube bundle mock-up. A more complete listing of the sizing profiles on a batch of specimens used to benchmark NDE accuracy through comparisons with destructive examination results are provided in Sec. 4. Finally, sample calculations are presented on a subset of tubes to assess multiparameter sizing of flaws in presence of simulated artifacts.

3.1 Comparison of Original and Processed NDE Profiles

As a means to demonstrate the level of enhancement in spatial resolution, the original and processed rotating probe data from a selected set of tubes with laboratory-grown cracks are presented here. The specimens were chosen primarily on the basis of complexity of the flaw signal, and in one case on the atypical nature of the probe response. Multiple-frequency EC data was acquired with a standard three-coil rotating probe that incorporates a 2.92-mm (0.115-in.) pancake, a mid-range +Point™, and 2.03-mm (0.080-in.) high-frequency pancake coil. Original amplitude profiles are all from the +Point coil at a single channel. Processed results on the other hand are the estimated depth profiles by using multichannel information from the mid-range pancake coil.

Figures 24-28 display a series of graphics on comparison of the original and processed channel data on specimens with laboratory-grown SCC degradation. Cracks of both OD and ID origin with axial and circumferential orientations are included. For all cases shown here, conventional isometric plot (Eddynet™) of the +Point™ probe amplitude response at a single frequency is displayed along with the multiparameter sizing profile of the same specimen. Image display of the sizing results is also shown in Figs. 25-27. The maximum depth obtained by conventional analysis of original data was notably underestimated in the majority of cases shown. Furthermore, complex geometry of cracks in some specimens resulted in difficulty of determining the flaw orientation from the original signal. Improvement in the spatial resolution of the processed data is clearly visible in all cases shown here. Comparison of estimated profiles with destructive results also shows improved sizing accuracy by multiparameter data analysis.

3.2 Analyses of Laboratory-Grown SCC Specimens

Data analysis results are presented next on representative samples from three separate batches of laboratory-grown specimens. Flaw types in these tubes are representative of those incorporated into the ANL tube bundle mock-up. All specimens used so far were made of 22.2-mm (0.875-in.)-diameter Alloy 600 tubing. The primary pancake coil readings from a 3-coil rotating probe was utilized for multiparameter data analysis. Manufactured flaws in the first

batch were composed primarily of circumferential and those in the second batch of axially oriented cracking. A separate batch of tubes was also produced to carry out blind studies for better assessment of the performance of alternate data analysis schemes in detection and sizing of various flaw types. Results are also presented here on the analysis of EC rotating-probe data on representative specimens from this collection of tubes. A detailed description of sizing results on this batch of tubes is provided in the next section in connection with destructive examination results.

Figures 29-33 display the results for selected samples from the first batch of NDE samples containing OD- and ID-initiated cracks of primarily circumferential orientation. Figure 29 displays results of the analysis for a laboratory-grown specimen with circumferential ODSCC. The sizing profile is shown for two arbitrarily selected views of the estimated depth. The estimated profile is shown for only a small section of tube in the vicinity of the crack. Figure 29(a) shows a representative display of intermediate results in image format. Preprocessed images at different stages of analysis for both the in-line standard and the flawed tube are also shown. Presentation of data in this format provides a useful tool for visual identification of potential flaws that often show up as structured indications within the baseline signal. Figure 29(b) shows terrain plots of the estimated flaw profile from two different azimuth and elevation angles. Analysis results in this case indicate presence of ≈360° multiple parallel circumferential cracks with maximum depth of ≈80% TW. Figures 30-33 display the sizing results for three other specimens with circumferential cracks. Finally, Fig. 33 shows the profile of an axial crack from the same batch of tubes. Analyses of EC inspection data on this set suggest that a majority of flaws are quite complex in nature.

Figure 34 displays the analysis results for specimen SGL-099 with laboratory-grown circumferential ODSCC degradation. Estimated depth profiles are shown as a terrain plot, as well as in axial and circumferential cross sections of the tube. Only the section of tube in the vicinity of the crack is shown here. Figure 34(a) shows a terrain plot of the estimated flaw depth profile from an arbitrarily chosen azimuth and elevation angle. Figure 34(b) shows the same data from axial and circumferential viewpoints, respectively. Analysis results in this case indicates the presence of 360° multiple circumferential cracking with a maximum depth exceeding 90% TW.

Figure 35 shows similar results for a specimen with multiple axial ODSCC degradation. The dominant indications are two parallel axial cracks with maximum depths estimated to be ≈90% TW. Figures 36-38 display sizing results for three other representative specimens from this sample set that contain multiple axial cracks. Eddy current inspection results from this second batch of tubes generally indicate that the majority of flaws are less complex in their morphology than those in the earlier batch of tubes that contained mostly circumferentially oriented cracks.

A batch of 31 tubes containing various crack types and sizes has also been utilized to further assess the capability of computer-aided data analysis algorithms. Flawed tubes in this set have been augmented with blank specimens having no visible damage, to better test the techniques. Eddy current readings on these tubes were acquired with and without simulated artifacts such as TSP, sludge, magnetite, and copper deposits that may be present to various
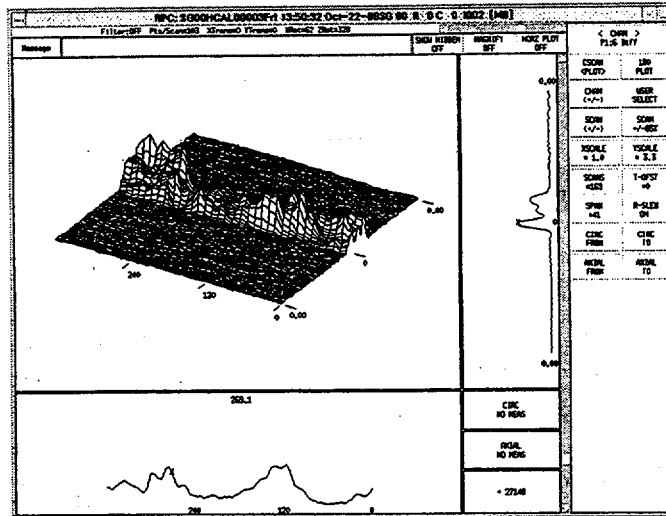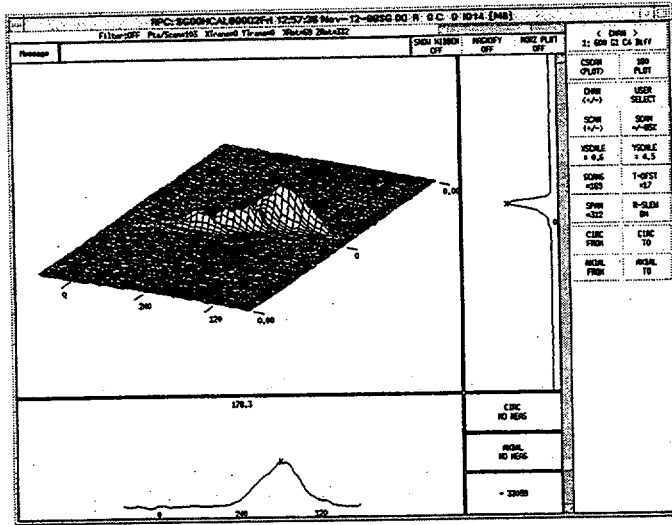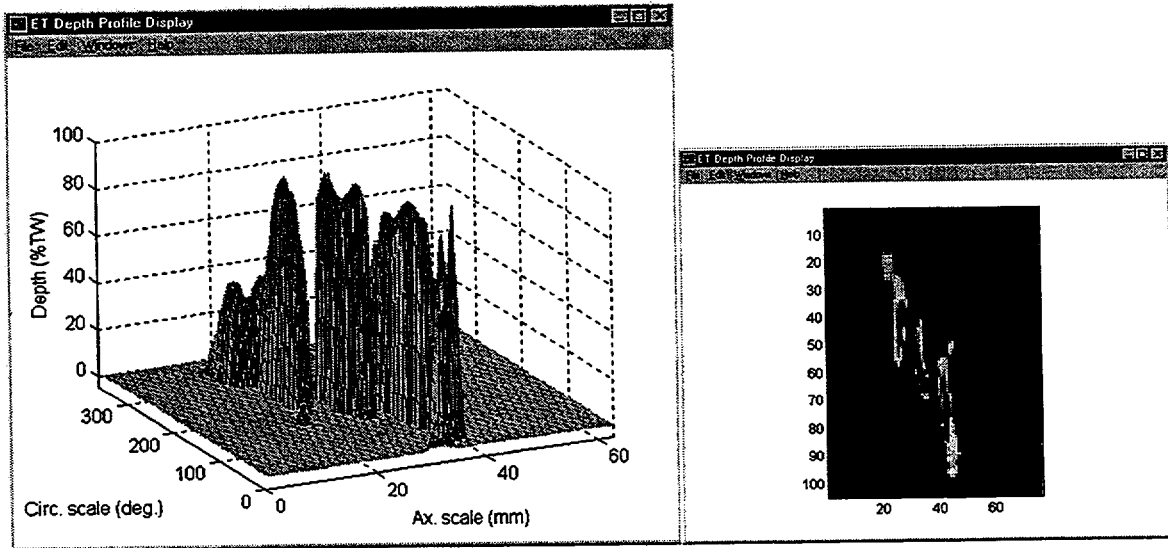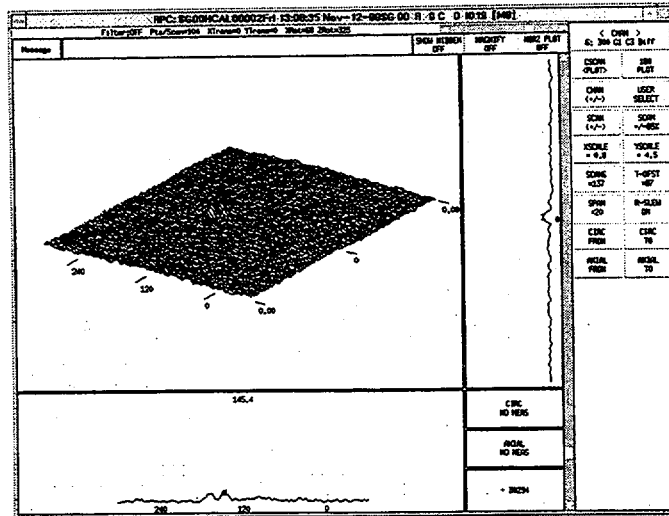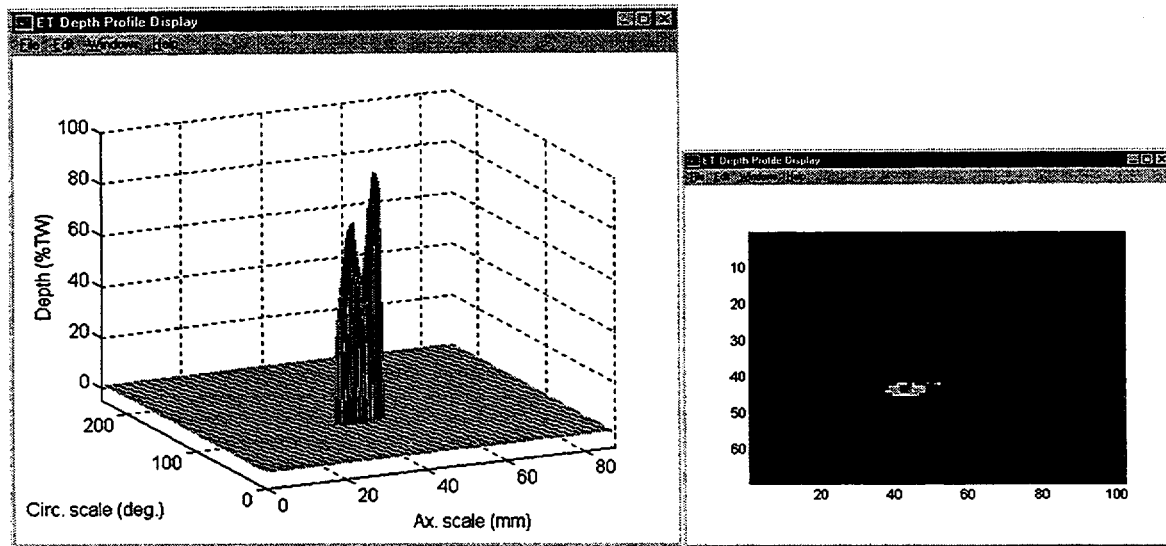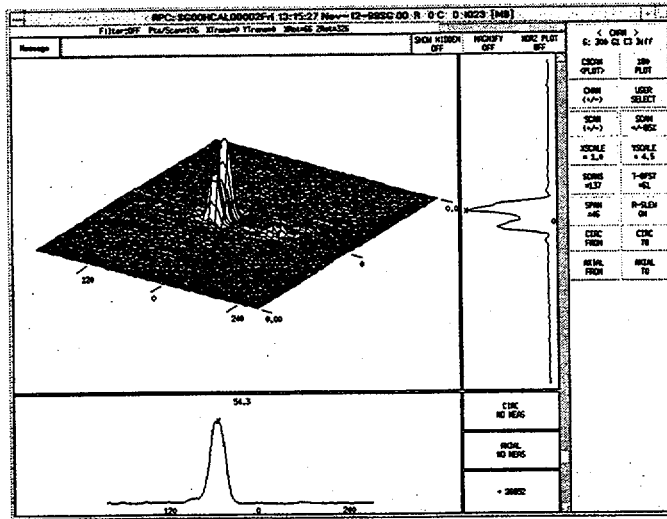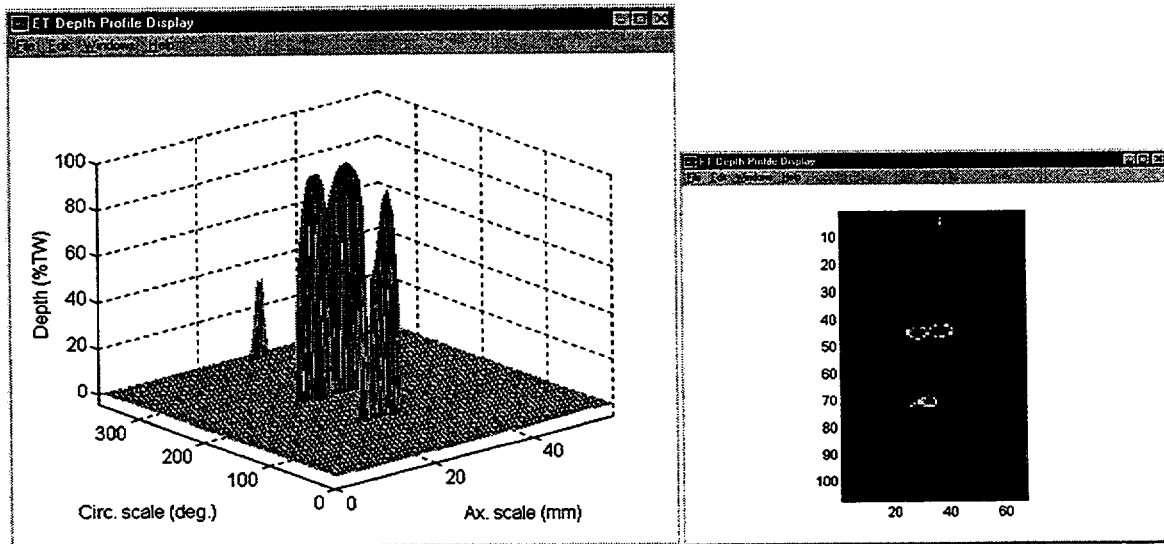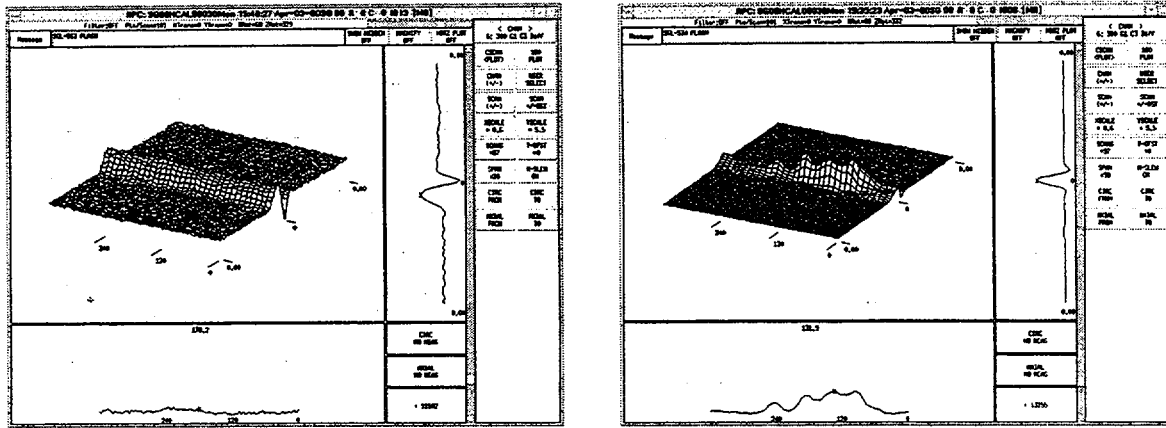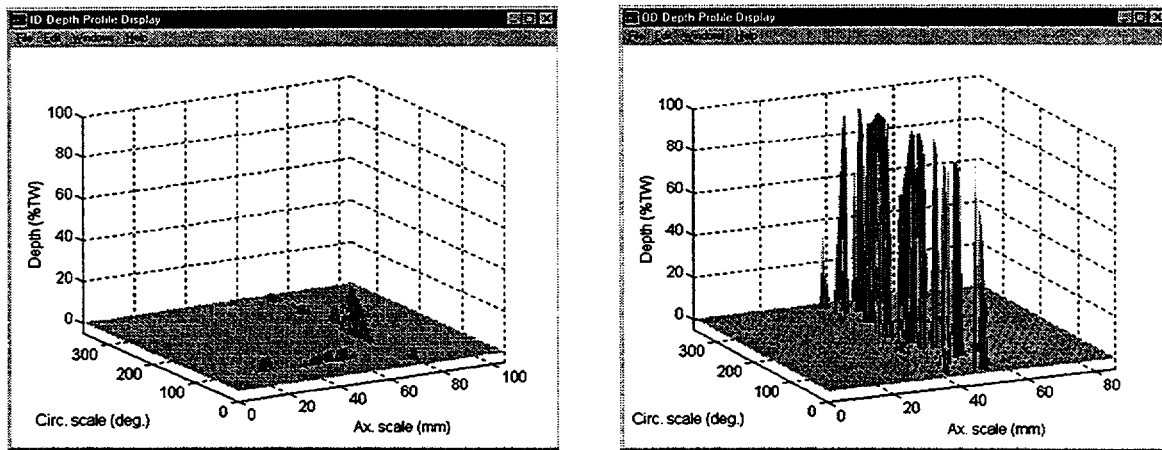
(a)
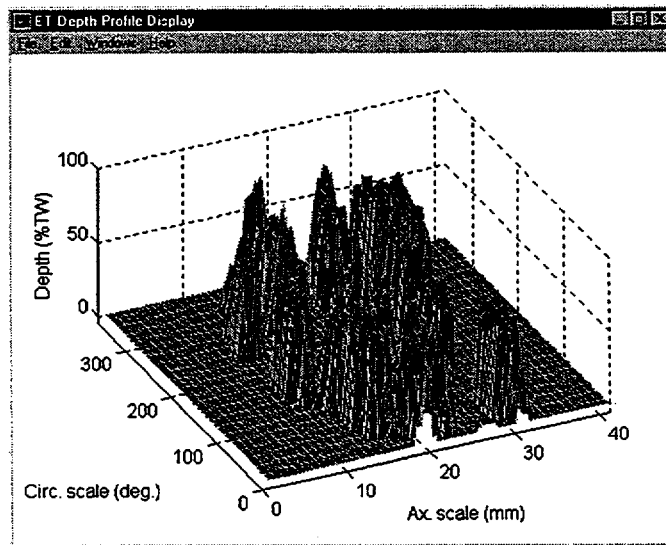
(b)

Figure 24. (a) Conventional isometric plot (Eddynet™) of +Point™ probe amplitude response and (b) multiparameter sizing profile of the same specimen with laboratory-grown circumferential ODSCC. Results suggest presence of ≈360° staggered cracking with maximum depth >80% TW.

(a)

(b)

Figure 25. (a) *Conventional isometric plot (Eddynet™) of +Point™ probe amplitude response and (b) multiparameter sizing profiles of same specimen with laboratory-grown circumferential ODSCC. Image display axes in this case are pixel locations in axial (horizontal) and circumferential (vertical) directions. Results suggest presence of ≈360° parallel cracking with maximum depth ≈100% TW.*

(a)

(b)

Figure 26. (a) Conventional isometric plot (Eddynet™) of +Point™ probe amplitude response and (b) multiparameter sizing profiles of same specimen with laboratory-grown axial ODSCC. The image display axes in this case are pixel locations in axial (horizontal) and circumferential (vertical) directions. NDE results suggest presence of axial cracking with max. depth >90% TW. Flaw exhibited no bobbin and uncharacteristically low rotating probe amplitude response.

42

(a)

(b)

Figure 27. (a) Conventional isometric plot (Eddynet™) of +Point™ probe amplitude response and (b) multiparameter sizing profiles of same specimen with laboratory-grown ODSCC. Image display axes in this case are pixel locations in axial (horizontal) and circumferential (vertical) directions. Results suggest presence of multiple axial cracking with maximum depth ≈100% TW.

43

(a)

(b)

Figure 28. (a) Conventional isometric plot (Eddynet™) of +Point™ probe amplitude response and (b) multiparameter sizing profiles for two specimens with laboratory-grown SCC indications at roll-transition region. Results suggest presence of circumferential ID cracks with maximum depth <30% TW (left) and 100% TW axial cracks (right).

degrees during field inspections. The effect of tube dimensional variations on detection and sizing of indications is also simulated by producing flaws within the transition zone of mechanically rolled tube sections.

Figures 39-47 display the analysis results for a subset of the 31-tube laboratory-grown specimens. In all cases, the results are shown as amplitude image displays of the standard and flawed tube at intermediate stages of processing, along with the estimated 3-D depth profile in the vicinity of the flawed region. The terrain plot is also displayed from two different view angles to provide axial and cross-sectional profiles. For the set of samples shown here, the profile of degraded regions suggests the presence of OD-initiated SCC in all tubes except one, which contained cracks that originate from the ID side of the tube. Eddy current inspection results from this batch of samples show a wide range of complexity in flaw geometries, varying from

44

single axial/circumferential to multiple and mixed-mode cracks. A more detailed description of NDE results on this set is provided in Sec. 4.
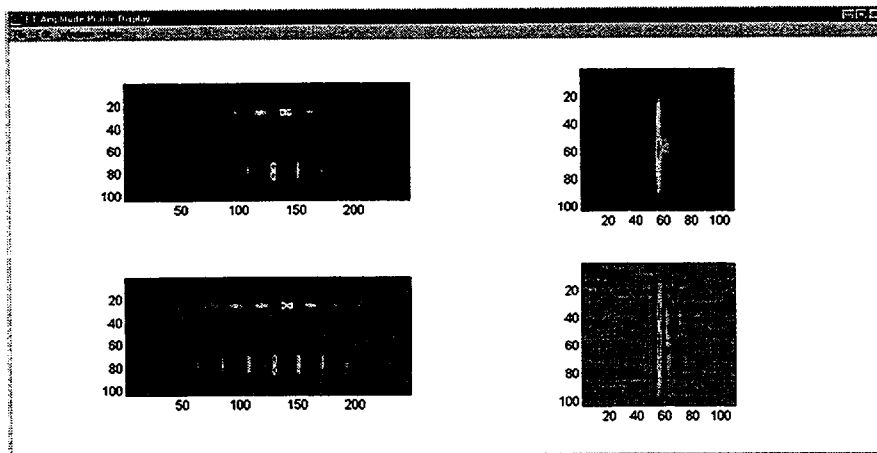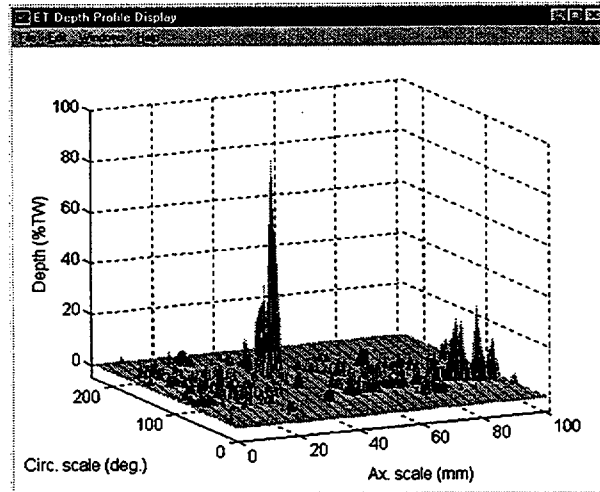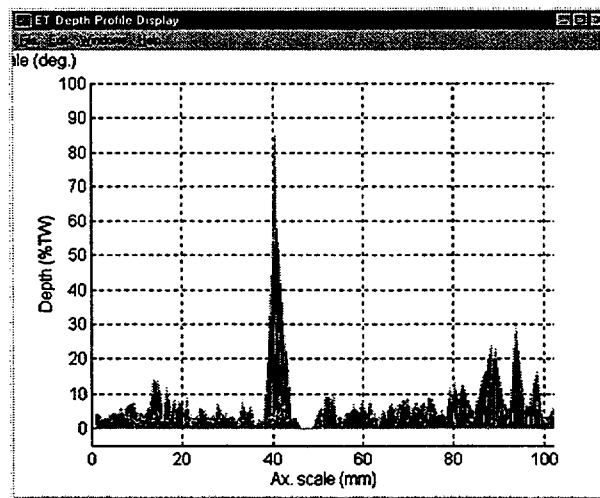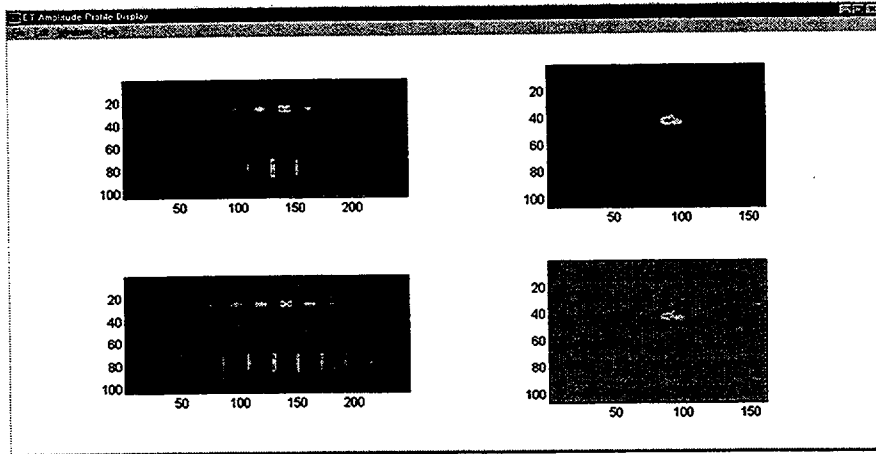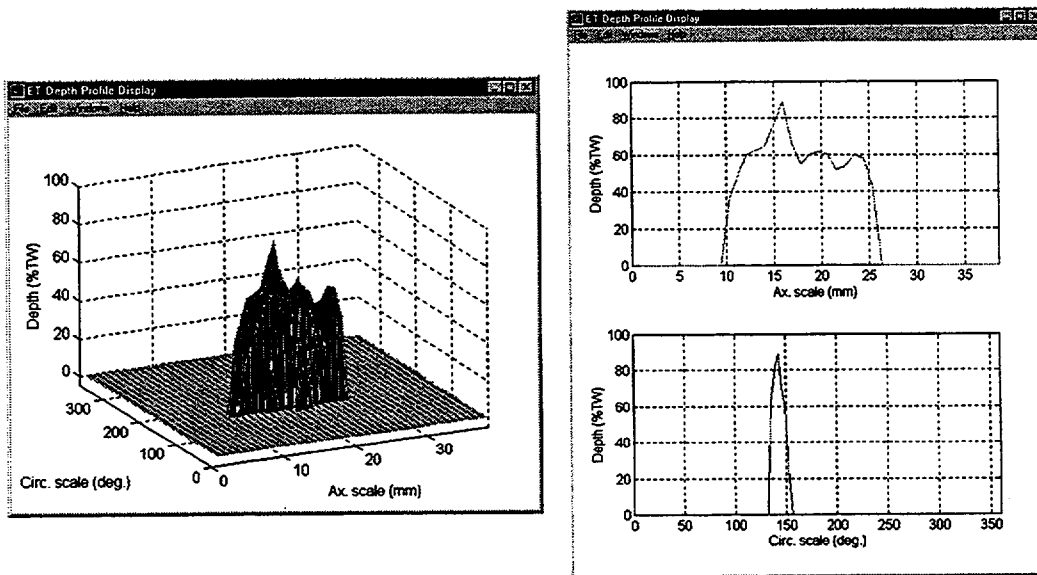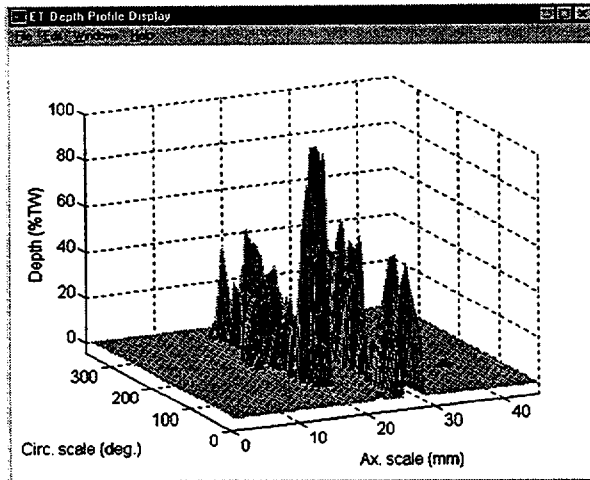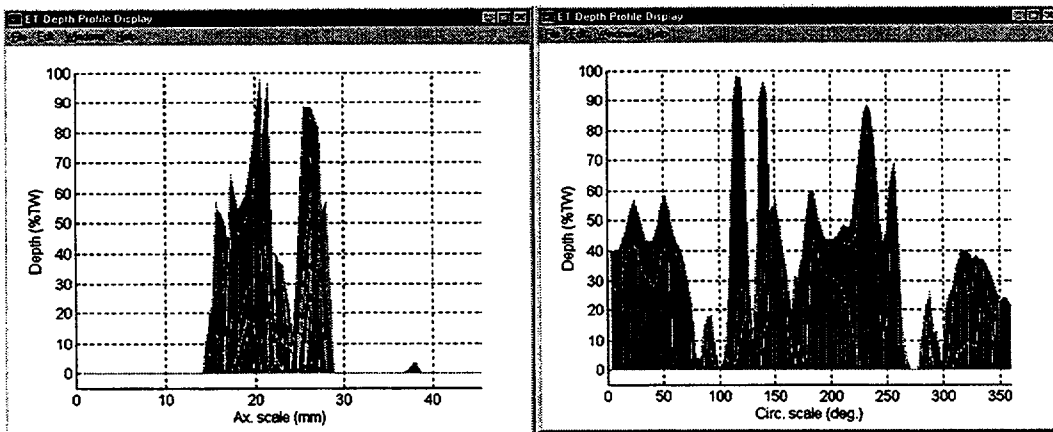

(a)
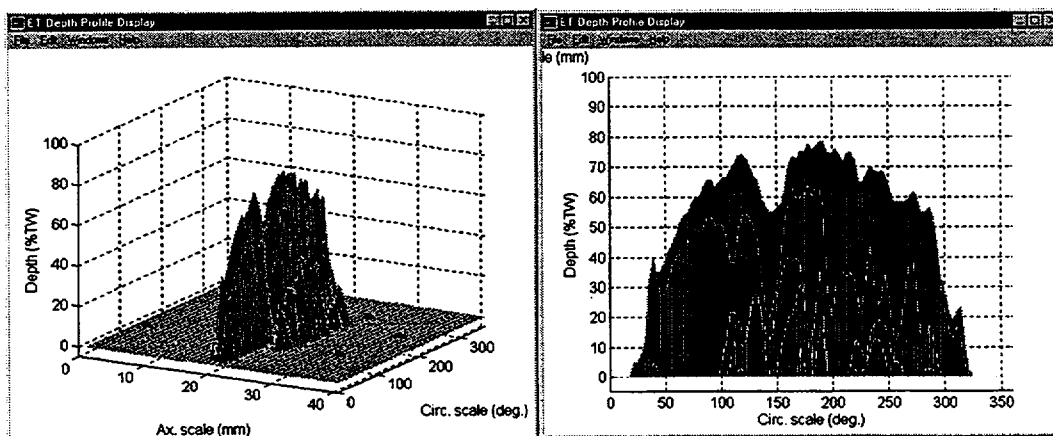
(b)

Figure 29. Representative display of data analysis results for specimen with laboratory-grown circumferential ODSCC showing (a) pre- (top) and post-processed (bottom) images of normalized data and (b) terrain and cross-sectional plots of estimated flaw profile. Results indicate ≈360° circumferential cracks, with maximum depth of ≈80% TW.
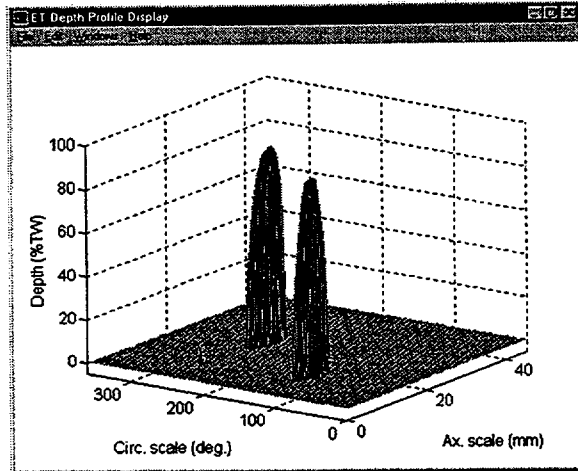
45
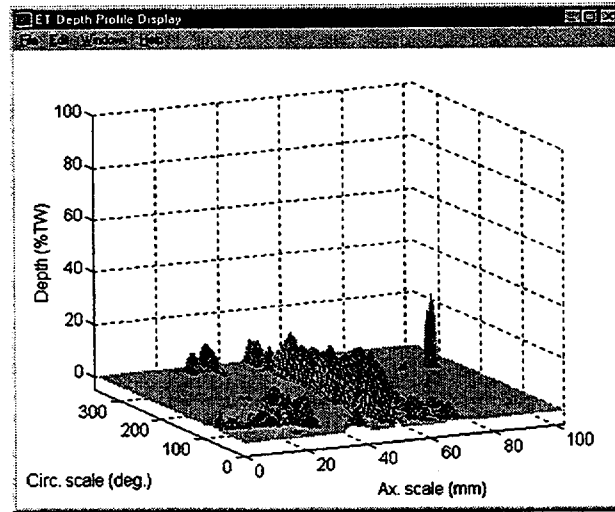
(a)
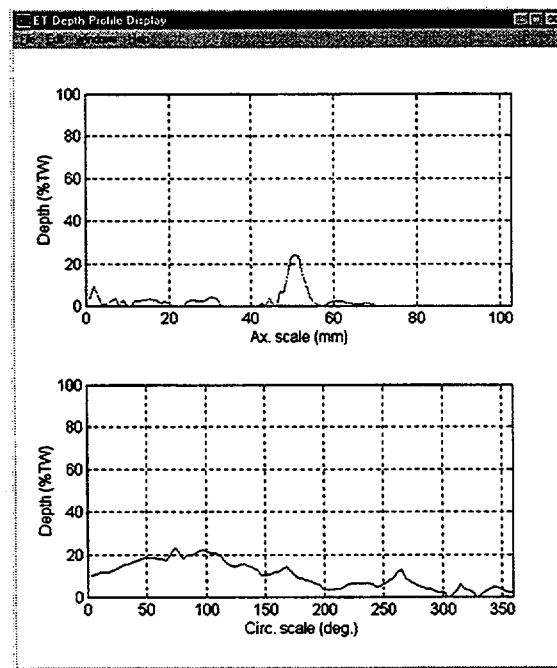
(b)

Figure 30. Representative display of data analysis results for specimen with laboratory-grown shallow circumferential IDSCC showing (a) terrain and (b) cross-sectional plots, taken over a point with maximum depth, of estimated flaw profile. Results indicate ≈360° circumferential cracking with maximum depth of >20% TW.
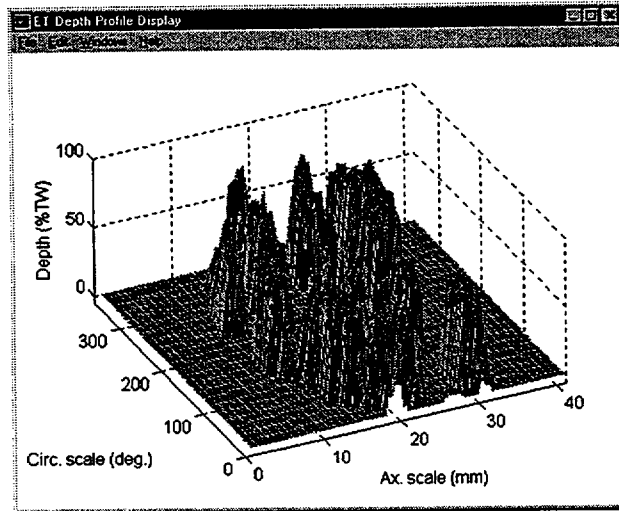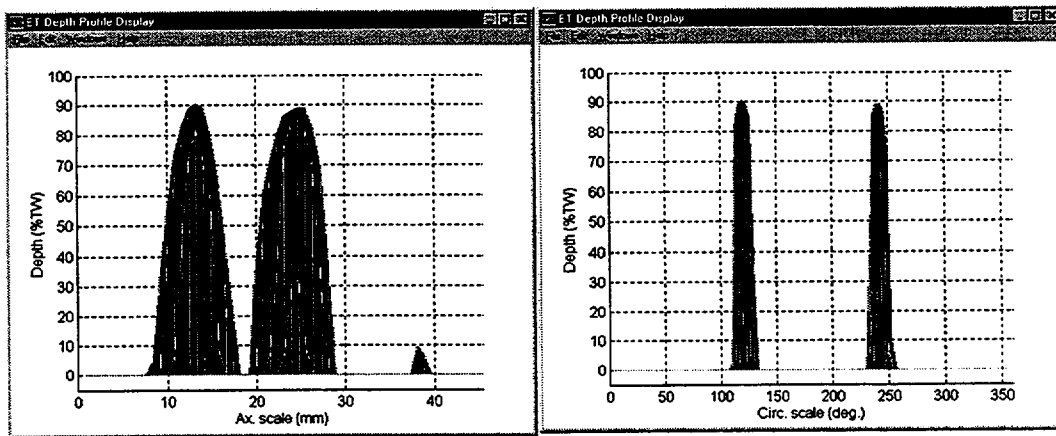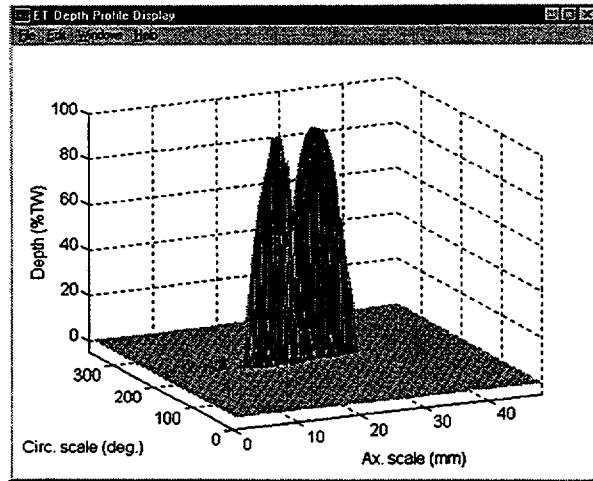
(a)
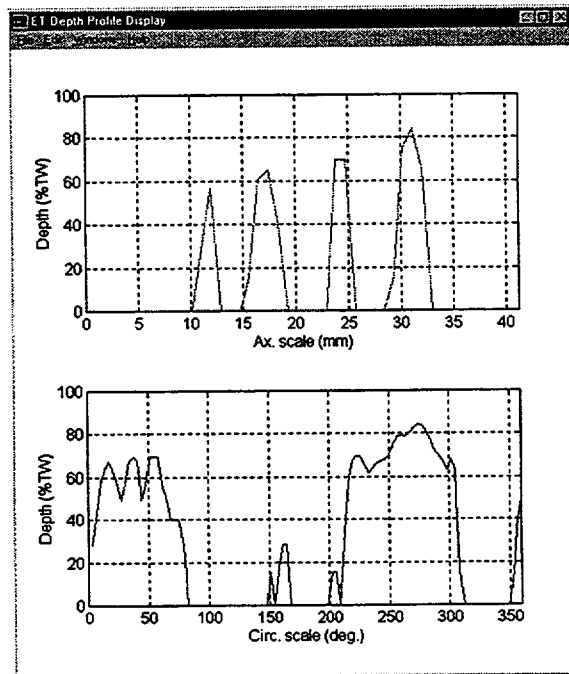
(b)

Figure 31. Representative display of data analysis results for specimen with laboratory-grown circumferential ODSCC showing (a) terrain and (b) cross-sectional plots, taken over a point with maximum depth, of estimated flaw profile. Results indicate ≈360° staggered circumferential cracking with maximum depth of >80% TW.
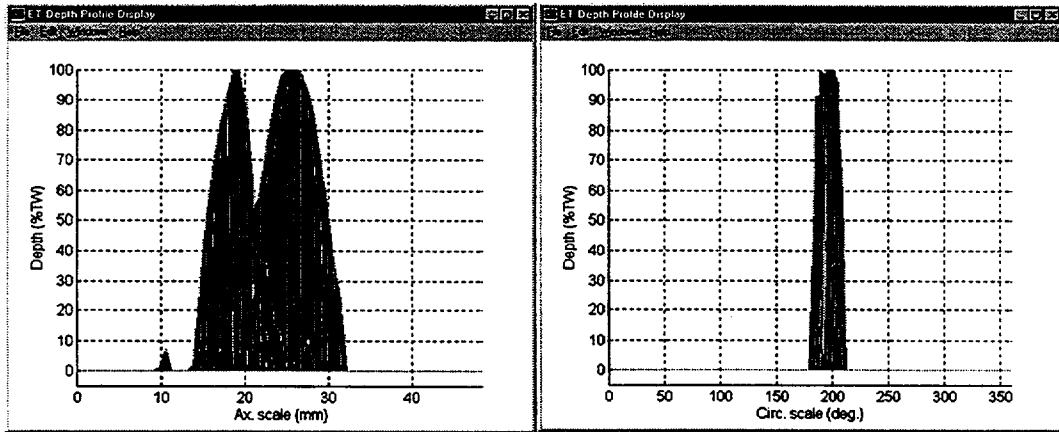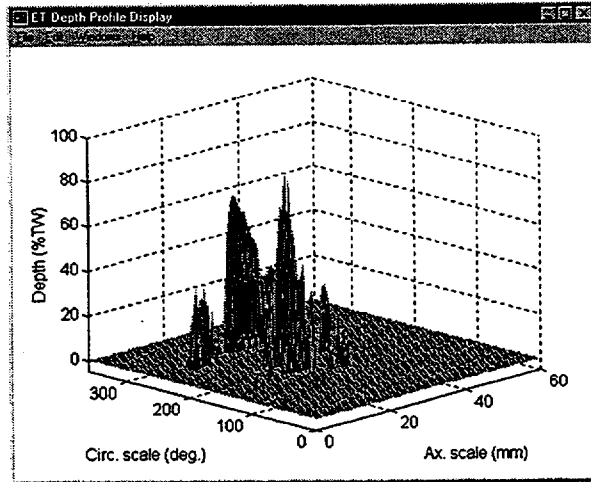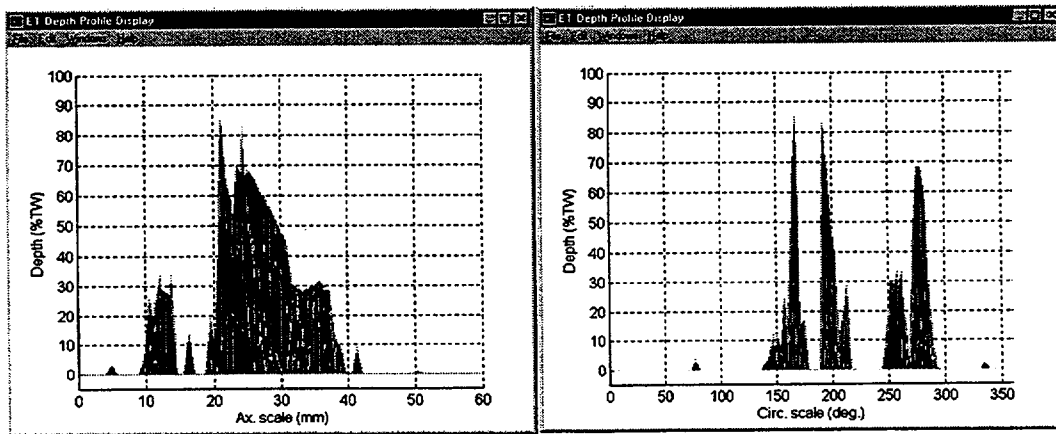
(a)

(b)

Figure 32. Representative display of data analysis results for specimen with laboratory-grown axial IDSCC showing (a) terrain plot and (b) cross-sectional view of estimated flaw profile. Results indicate dominant single axial crack with maximum depth of >80% TW.

48

(a)

(b)

Figure 33. Representative display of data analysis results for specimen with laboratory-grown axial ODSCC showing (a) pre- (top) and post-processed (bottom) images of normalized data and (b) terrain and cross-sectional plots, taken over a point with maximum depth, of estimated flaw profile. Results indicate >15-mm (0.6-in.)-long axial crack with maximum depth of ≈90% TW.

(a)

(b)

Figure 34. Representative display of data analysis results for specimen with laboratory-grown circumferential ODSCC showing (a) terrain and (b) cross-sectional views of estimated flaw profile. Results indicate ≈360° circumferential cracks with maximum depth >90% TW.
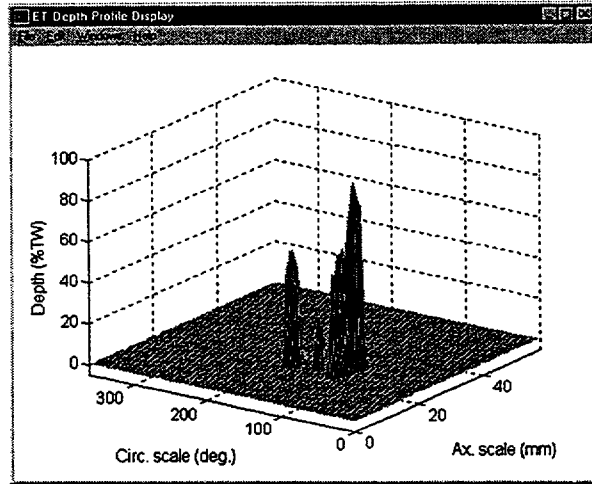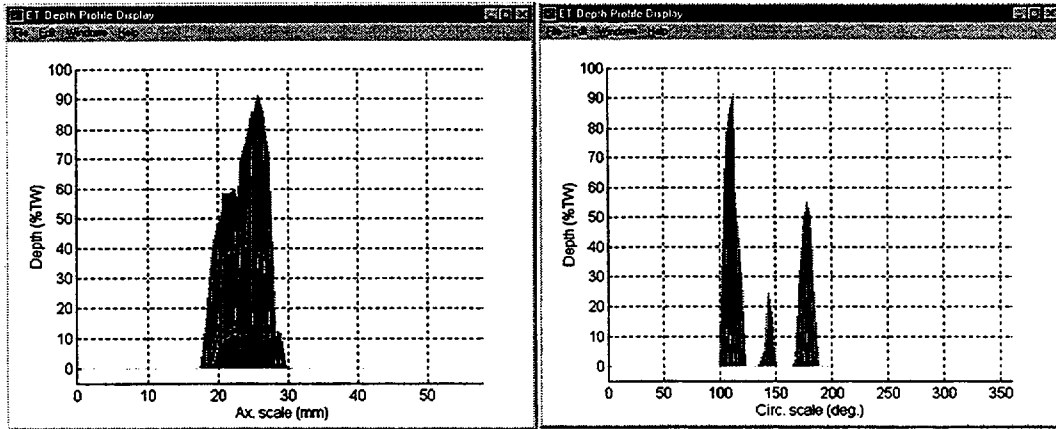
(a)

(b)

Figure 35. Representative display of data analysis results for specimen with laboratory-grown axial ODSCC showing (a) terrain and (b) cross-sectional views of estimated flaw profile. Results show two indications with maximum depths >80% TW.
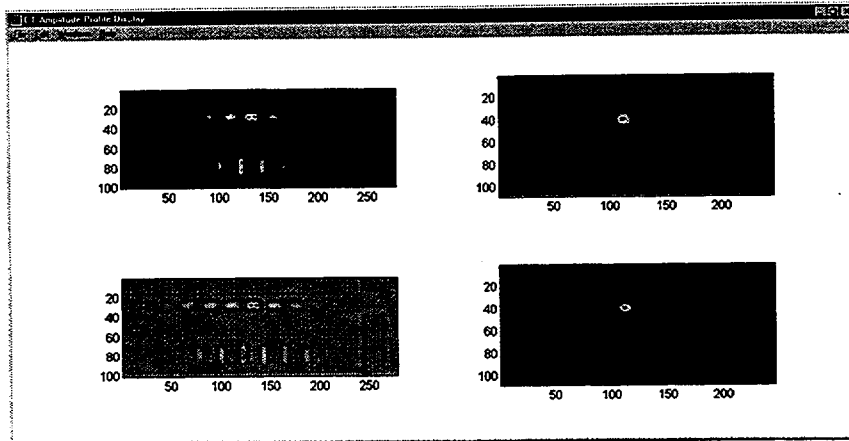
(a)

(b)

Figure 36. Representative display of data analysis results for specimen with laboratory-grown axial ODSCC showing (a) terrain and (b) cross-sectional views of estimated flaw profile. Results indicate two closely spaced parallel (axially offset) cracks with maximum depths reaching 100% TW.

(a)

(b)

Figure 37. Representative display of data analysis results for specimen with laboratory-grown axial ODSCC showing (a) terrain and (b) cross-sectional views of estimated flaw profile. Results indicate multiple axial cracks with maximum depths >80% TW.
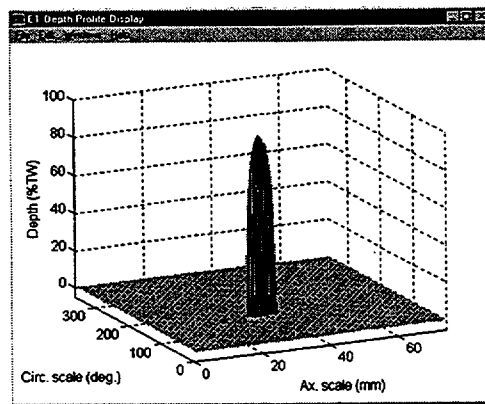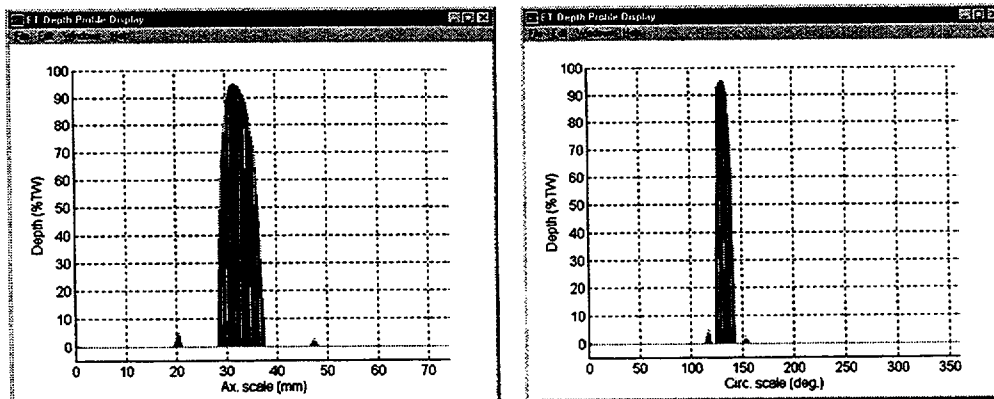
(a)

(b)

Figure 38. Representative display of data analysis results for specimen with laboratory-grown axial ODSCC showing (a) terrain and (b) cross-sectional views of estimated flaw profile. Results indicate multiple axial cracks with maximum depths >80% TW.
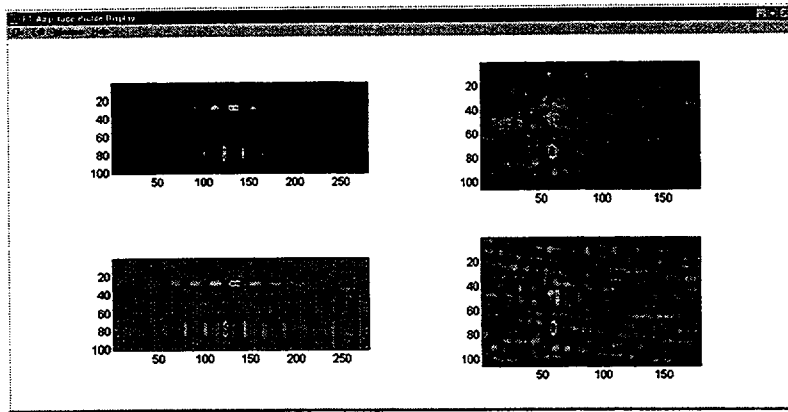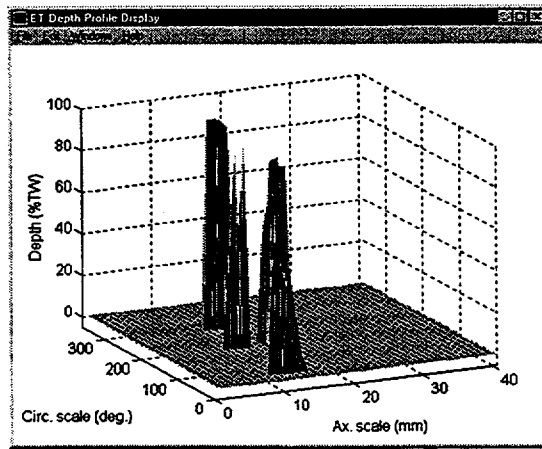
Figure 39. Representative display of data analysis results for specimen with laboratory-grown ODSCC degradation showing (a) image display, (b) terrain profile, and (c) cross-sectional views of estimated flaw size. Results indicate single crack with maximum depth >90% TW.
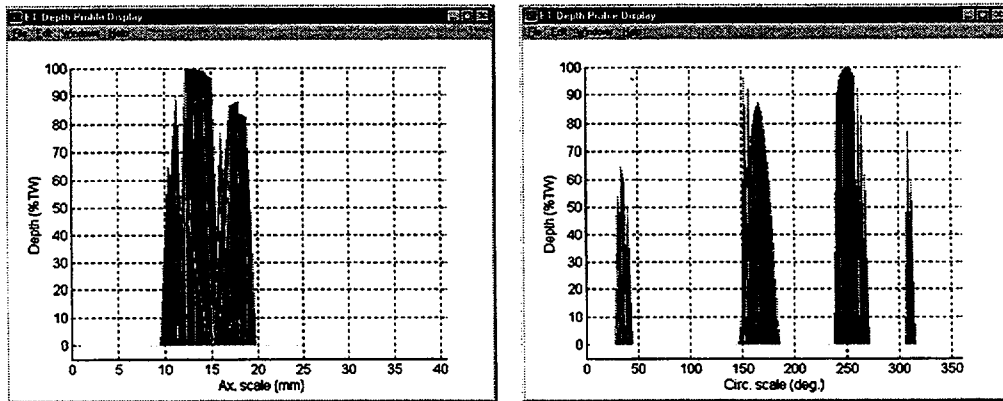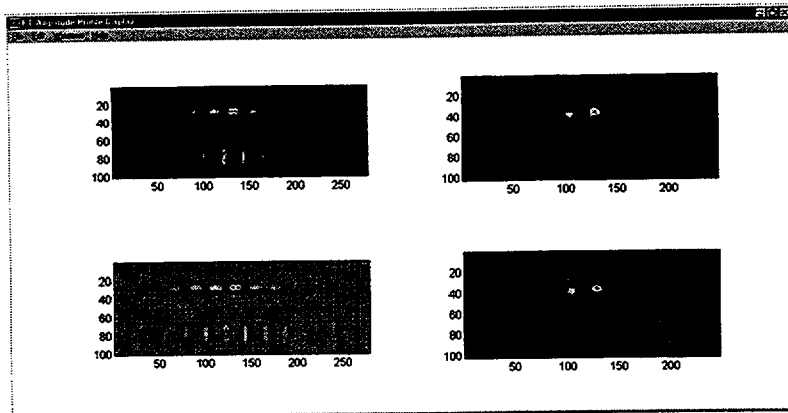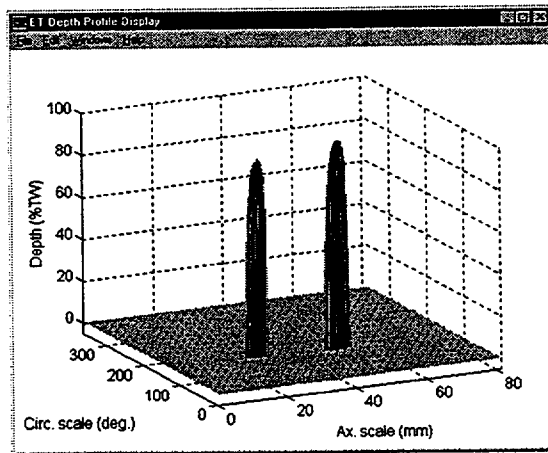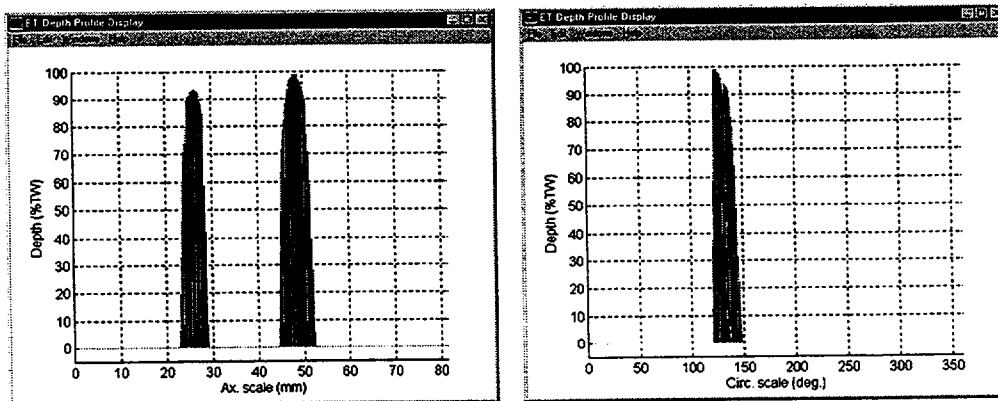
(a)

(b)

(c)

Figure 40. Representative display of data analysis results for specimen with laboratory-grown ODSCC degradation showing (a) image display, (b) terrain profile, and (c) cross sectional views of estimated flaw size. Results indicate multiple cracks around circumference, with maximum depth of dominant flaw reaching 100% TW.

Figure 41. *Representative display of data analysis results for specimen with laboratory-grown ODSCC degradation showing (a) image display, (b) terrain profile, and (c) cross-sectional views of estimated flaw size. Results indicate two circumferentially offset cracks, with maximum depth reaching ≈100% TW.*
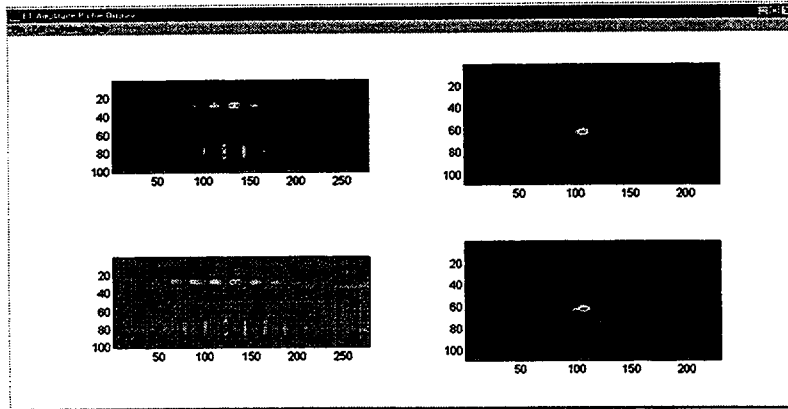
(a)

(b)

(c)

Figure 42. Representative display of data analysis results for specimen with laboratory-grown ODSCC degradation showing (a) image display, (b) terrain profile, and (c) cross-sectional views of estimated flaw size. Results indicate segmented crack with maximum depth of ≈100% TW.
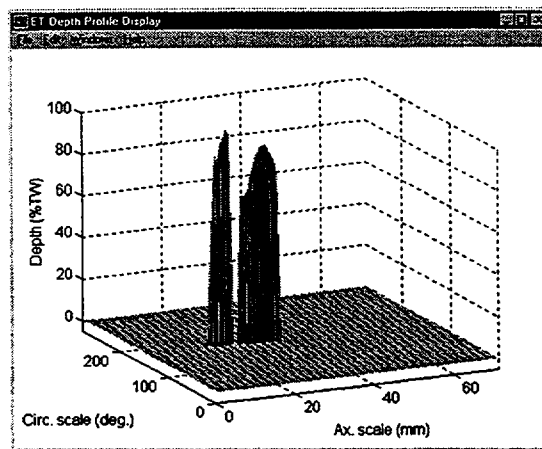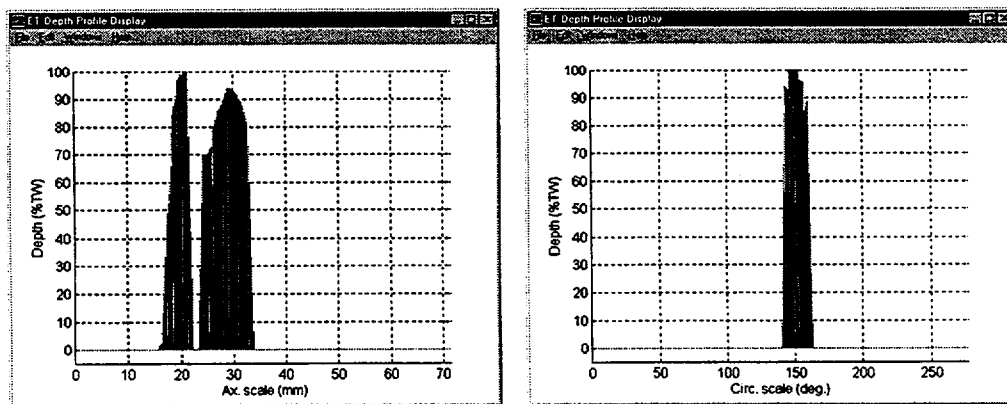
Figure 43. Representative display of data analysis results for specimen with laboratory-grown ODSCC degradation showing (a) image display, (b) terrain profile, and (c) cross-sectional views of estimated flaw size. Results indicate single axial crack with maximum depth >90% TW.
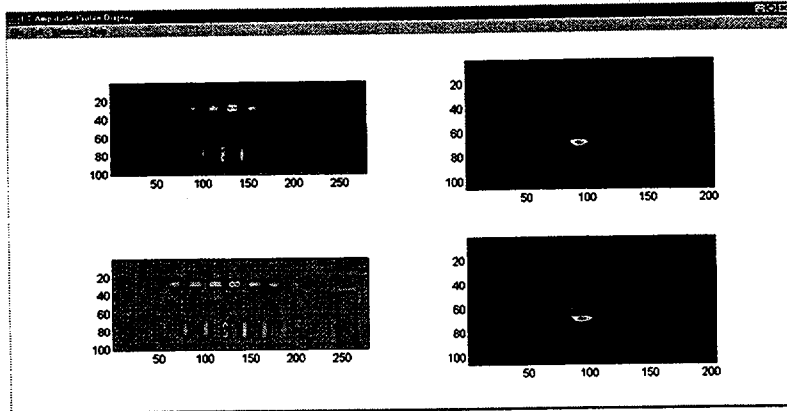
(a)

(b)

(c)

Figure 44. Representative display of data analysis results for specimen with laboratory-grown ODSCC degradation showing (a) image display, (b) terrain profile, and (c) cross-sectional views of estimated flaw size. Results indicate multiple cracks around circumference, with maximum depth >60% TW.
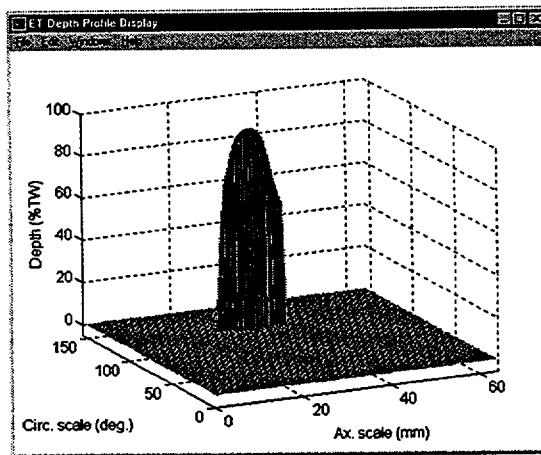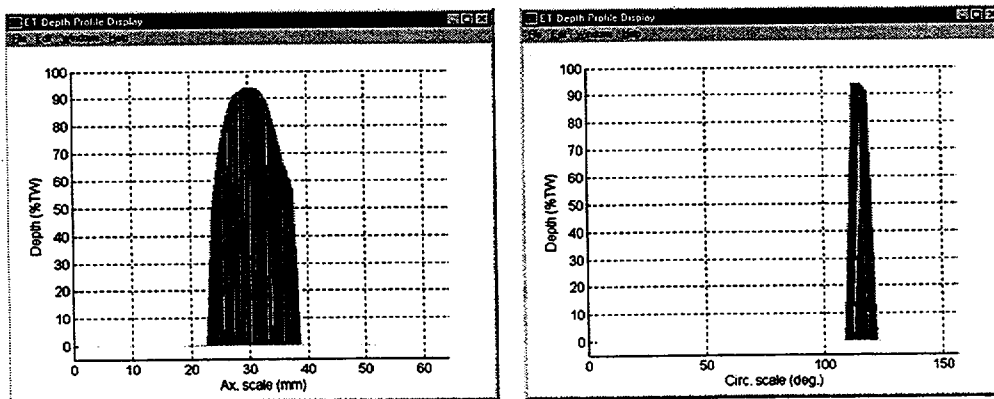
60

(a)

(b)

(c)

Figure 45. Representative display of data analysis results for specimen with laboratory-grown ODSCC degradation showing (a) image display, (b) terrain profile, and (c) cross-sectional views of estimated flaw size. Results indicate multiple cracks around circumference, with maximum depth of dominant flaws reaching ≈100% TW.
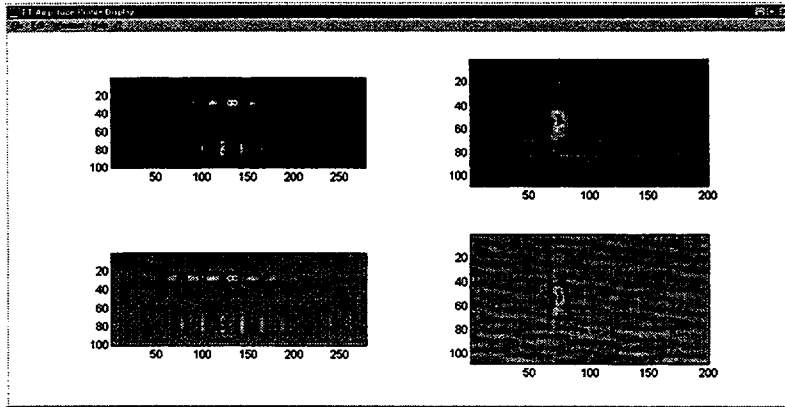
61

(a)

(b)

(c)

Figure 46. Representative display of data analysis results for specimen with laboratory-grown ODSCC degradation showing (a) image display, (b) terrain profile, and (c) cross-sectional views of estimated flaw size. Results indicate multiple cracks at several axial locations around circumference, with maximum depth >60% TW.
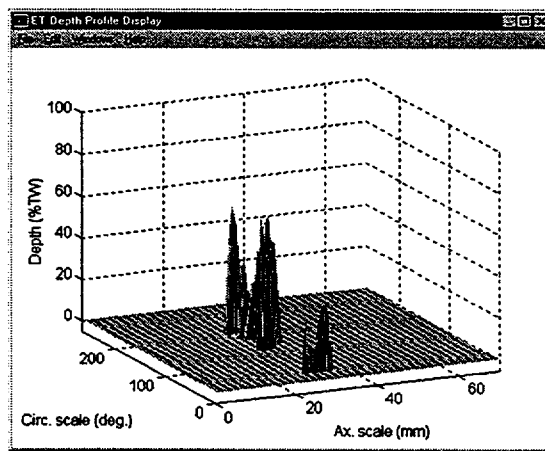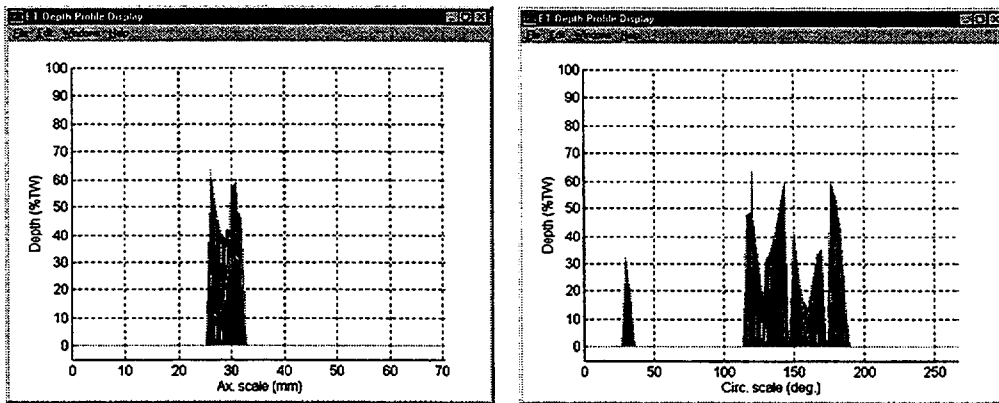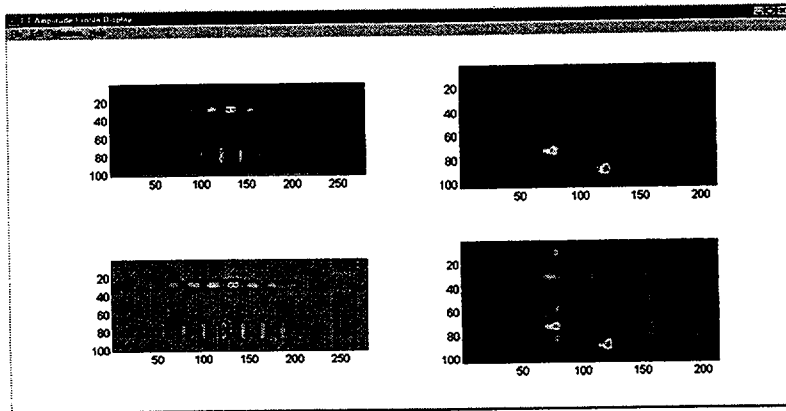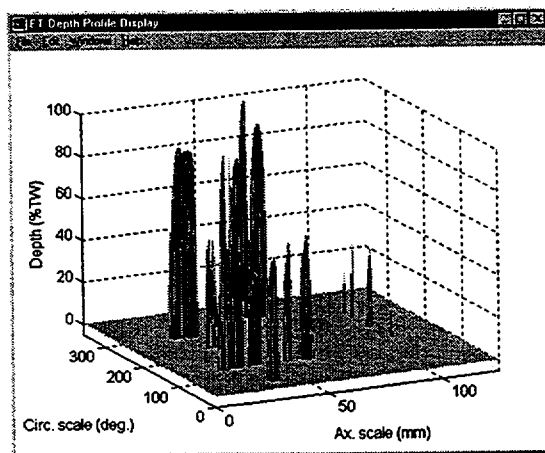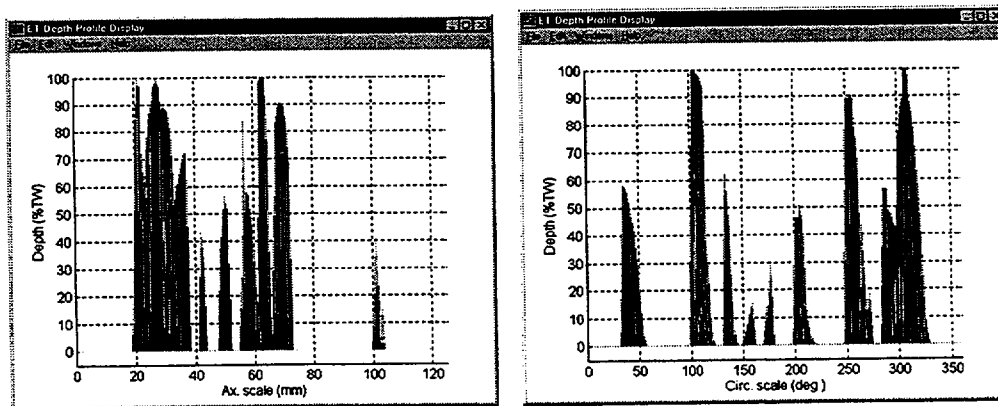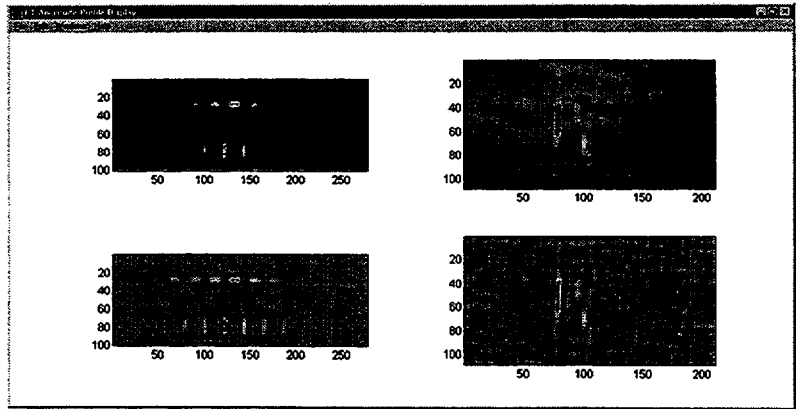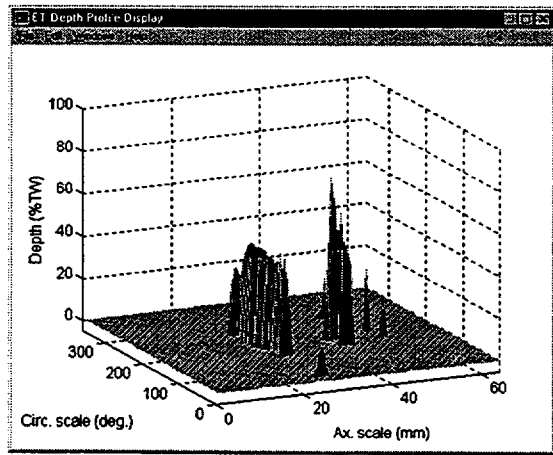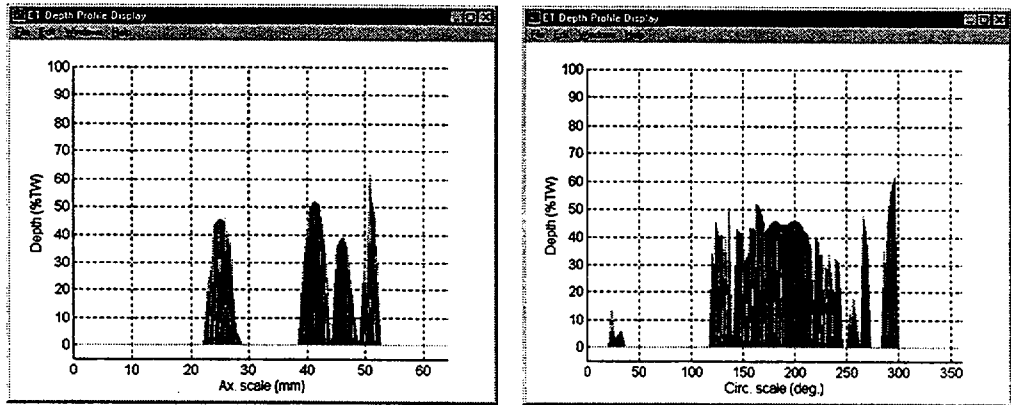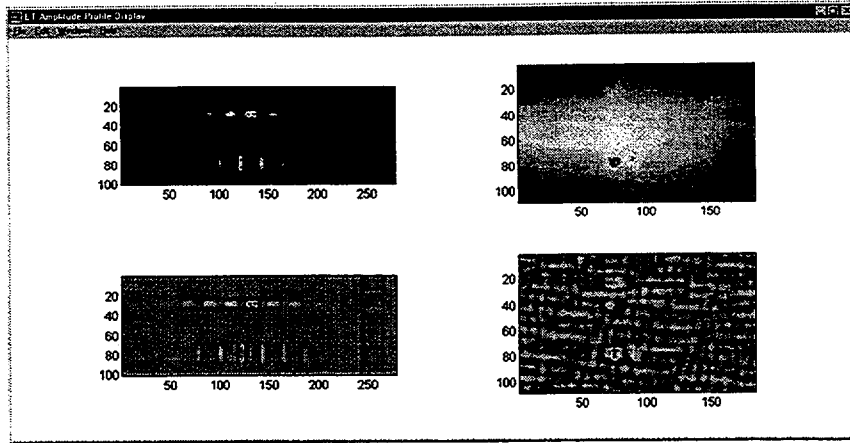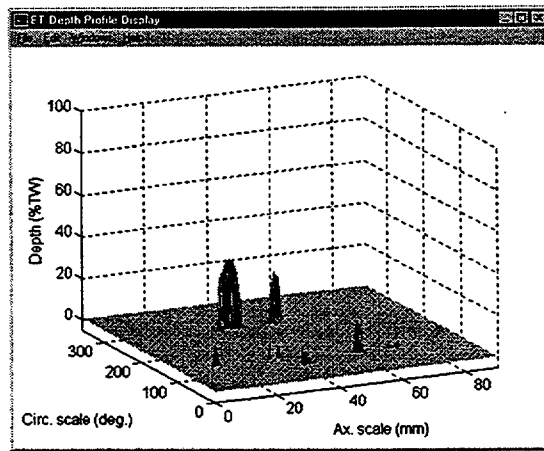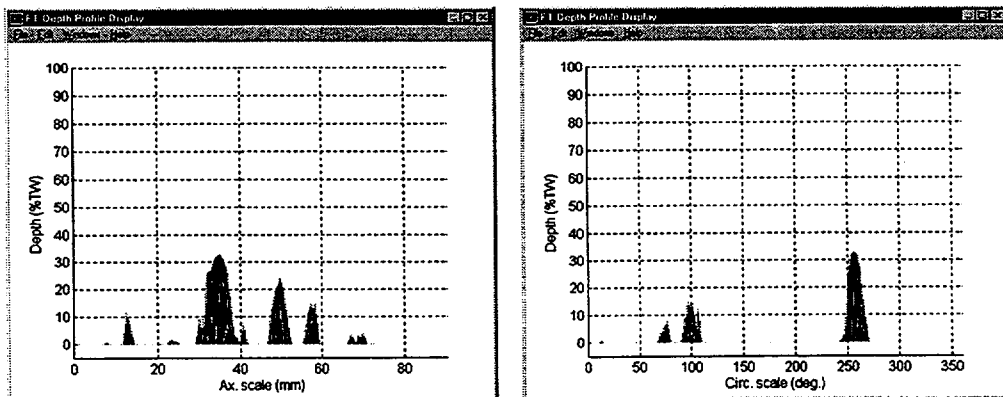
62

(a)

(b)

(c)

Figure 47. Representative display of data analysis results for specimen with laboratory-grown IDSCC degradation showing (a) image display, (b) terrain profile, and (c) cross-sectional views of estimated flaw size. Results indicate multiple cracks, with dominant crack depth <35% TW.

## 3.3 Assessment of Sizing Accuracy in Presence of Artifacts

In continuation of studies to demonstrate the effect of various artifacts on flaw signals, results of the analyses on a subset of specimens from the 31-tube set are given here. Data on these tubes was collected with and without the removable collars that simulate artifacts such as TSP, sludge, magnetite, and copper deposits that may be present to various degrees during field inspections. Representative test cases from profiling of six tubes are displayed as amplitude images of the standard and flawed tube with simulated artifact and terrain plots of sizing profile in the vicinity of degraded region of the tube. Eddy current data for each test case of simulated OD artifact was collected separately, each time scanning the entire batch of tubes. Acquisition frequencies represent typical primary and auxiliary channels that are used for the inspection of thin-wall SG tubing. Studies so far suggest that the degree of signal distortion depends primarily on the artifact geometry and composition, as well as signal amplitude at a given excitation frequency.

Figures 48 and 49 show the profiling results for the case of TSP simulation. Terrain plots of estimated profiles are displayed for a small section of the tube in the vicinity of the flaw. Variation of maximum depth for the deep crack shown in Fig. 48 was relatively insignificant for all the simulated collars used in the study. For the test case of shallower ODSCC shown in Fig. 49, the dominant indications were placed near the edge of the collar. Although this scenario generally results in maximum perturbation of the flaw signal, the profiles for the case of plain tube and TSP simulation are in good agreement.

Figures 50 and 51 show representative test cases of deep and shallow ODSCC, respectively, in the presence of a sludge artifact. Finally, Figs. 52 and 53 display the profiling results for OD and ID cracking, respectively, for the case of magnetite simulation. The estimated maximum depth of cracks varied by <10% of tube wall thickness for all the test cases considered here. As expected, the effect of OD simulated collars are less for larger amplitude signals and more significant for the smaller amplitude portions of the flaw. For the specimens shown here, variations in NDE flaw depth and length are within the range that is expected from such factors as probe alignment and data acquisition parameters (i.e., variations in sampling rate, rotational and push/pull speed). Examination of additional samples from this data set with various degrees of flaw complexity, origin, dimension, and orientation is currently underway. Results of this study should help understand the uncertainties in the accuracy of this sizing technique. Studies so far suggest that the degree of signal distortion depends primarily on the artifact geometry and composition, as well as on signal amplitude at a given excitation frequency.
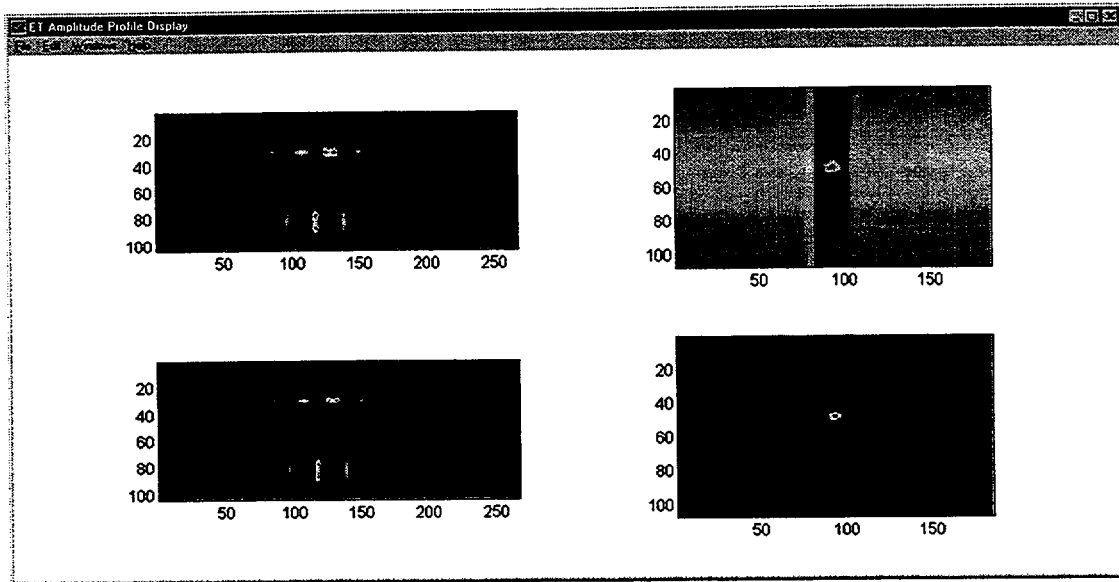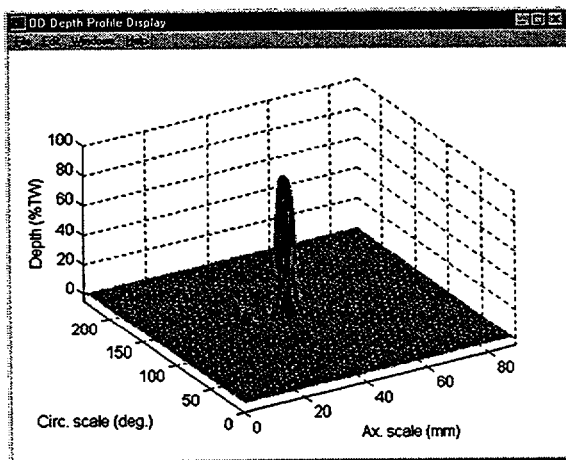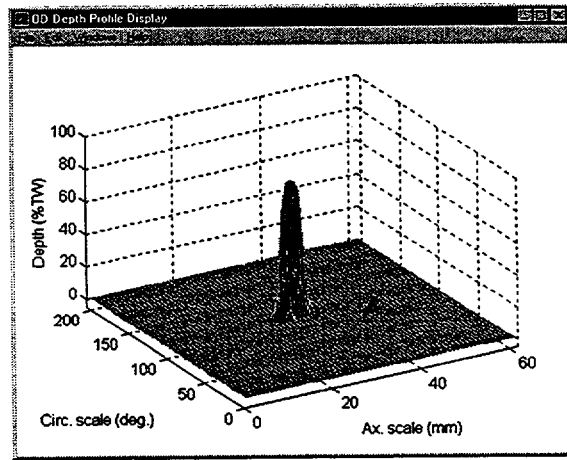
Figure 48. *Data analysis results for specimen with laboratory-grown ODSCC showing (a) Image display of scanned region of standard and flawed tube with a TSP collar placed over crack. Also shown are terrain plots of depth profile over approximately same region of tube (b) without and (c) with TSP collar. Estimated maximum depth (>90% TW from plain tube) varies by <10% TW for all simulated artifacts.*

Figure 49. Data analysis results for specimen with laboratory-grown ODSCC showing (a) Image display of scanned region of standard and flawed tube with TSP collar placed over crack. Also shown are terrain plots of depth profile over approximately same region of tube (b) without and (c) with TSP collar. Estimated maximum depth (<50% TW from plain tube) varies by <10% TW for all simulated artifacts.
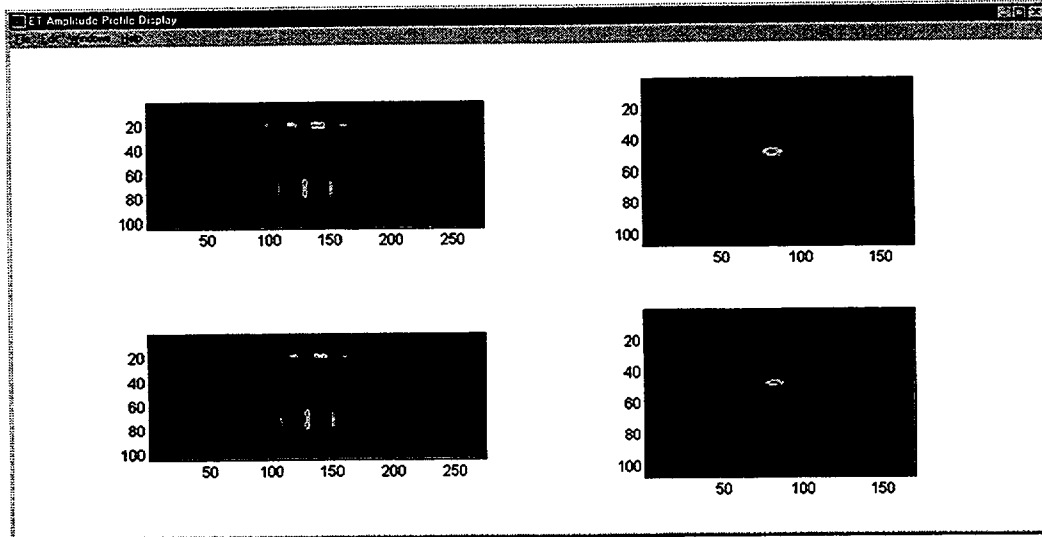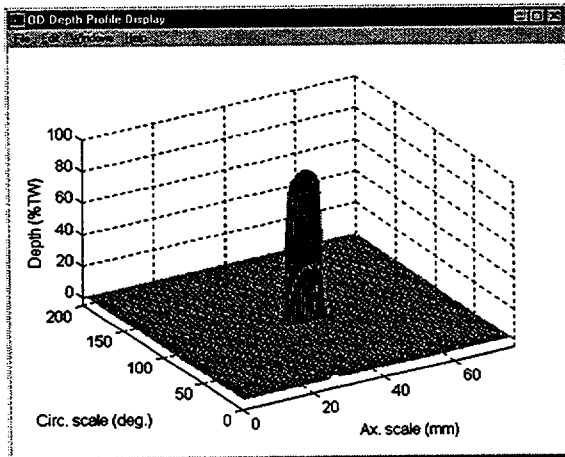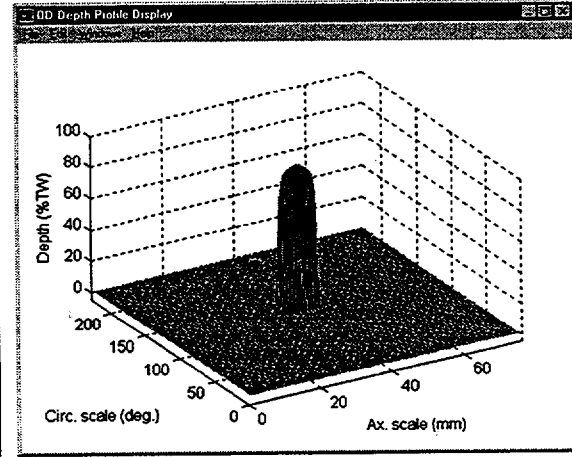
Figure 50. *Data analysis results for specimen with laboratory-grown ODSCC showing (a) Image display of scanned region of standard and flawed tube with sludge collar placed over crack. Also shown are terrain plots of depth profile over approximately same region of tube (b) without and (c) with sludge collar. Estimated maximum depth (>90% TW from plain tube) varies by <10% TW for all simulated artifacts.*
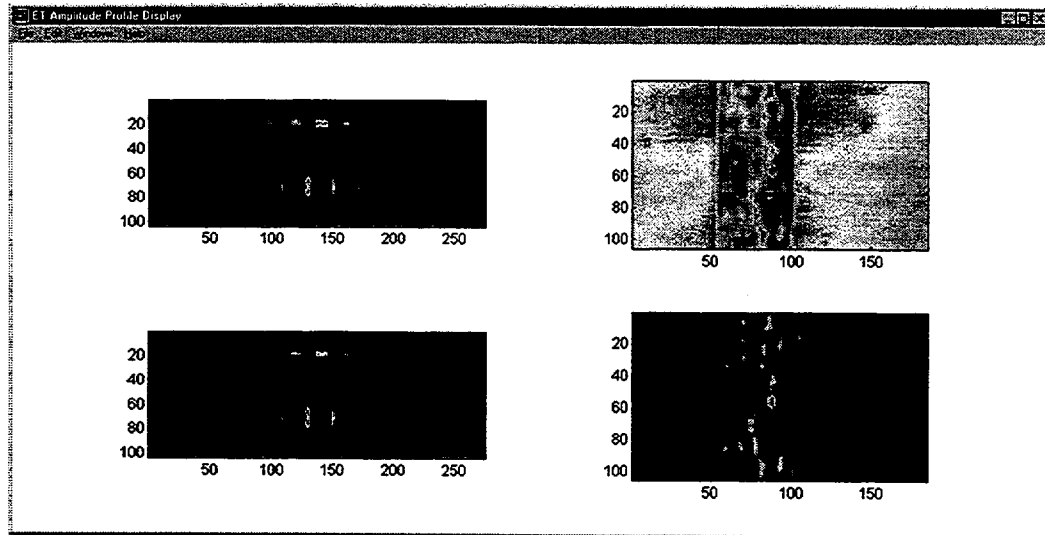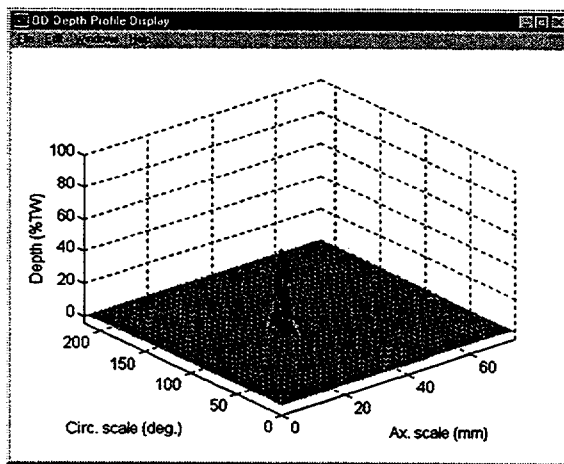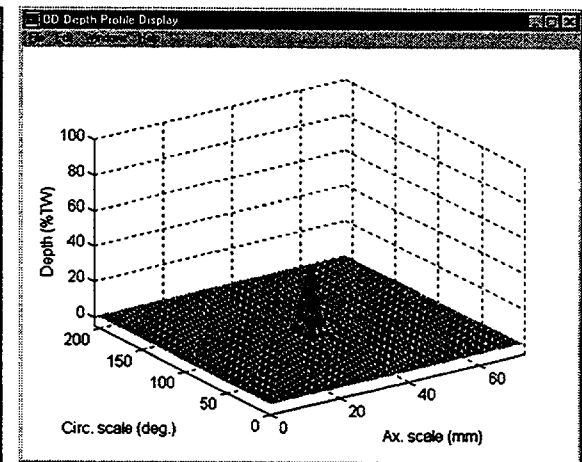
Figure 51. Data analysis results for specimen with laboratory-grown ODSCC showing (a) Image display of scanned region of standard and flawed tube with sludge collar placed over crack. Also shown are terrain plots of depth profile over approximately same region of tube (b) without and (c) with sludge collar. Estimated maximum depth (≈40% TW from plain tube) varies by <10% TW for all simulated artifacts.
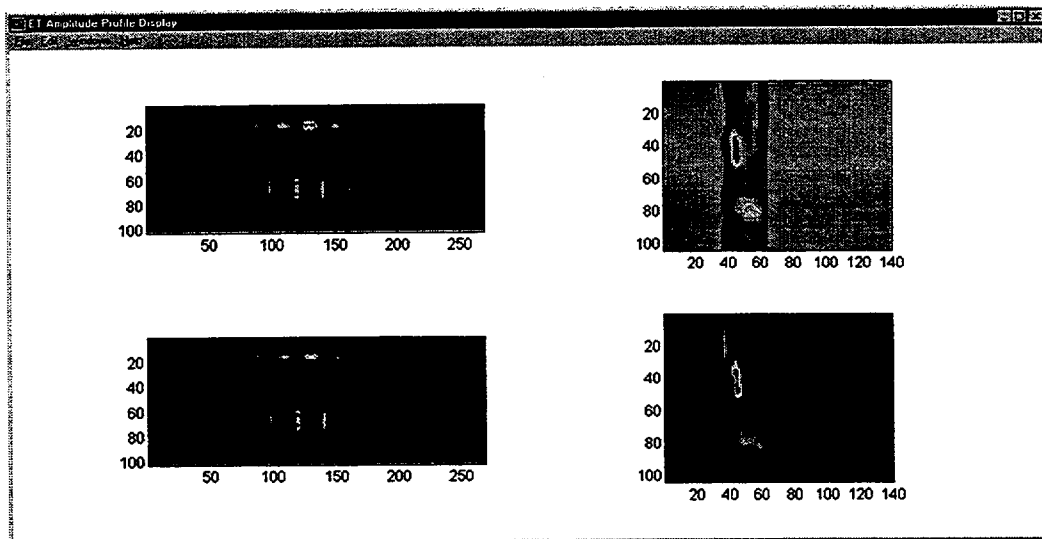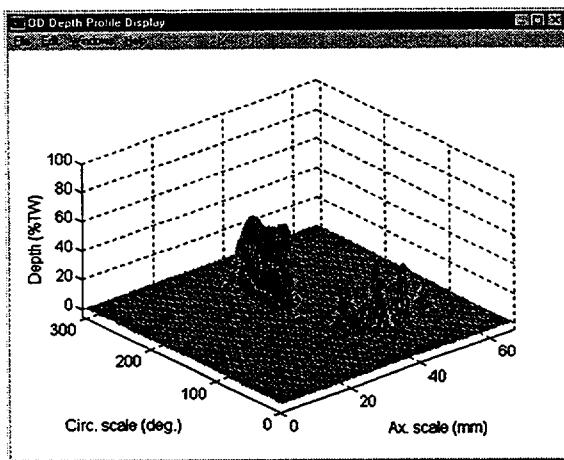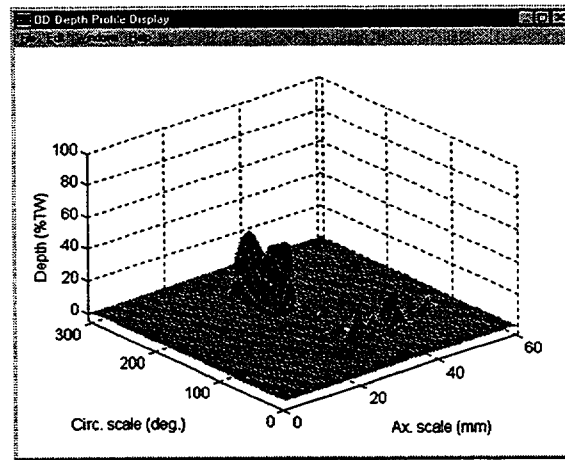
Figure 52. *Data analysis results for specimen with laboratory-grown ODSCC showing (a) Image display of scanned region of standard and flawed tube with magnetite collar placed over crack. Also shown are terrain plots of depth profile over approximately same region of tube (b) without and (c) with magnetite collar. Estimated maximum depth (<50% TW from plain tube) varies by <10% TW for all simulated artifacts.*
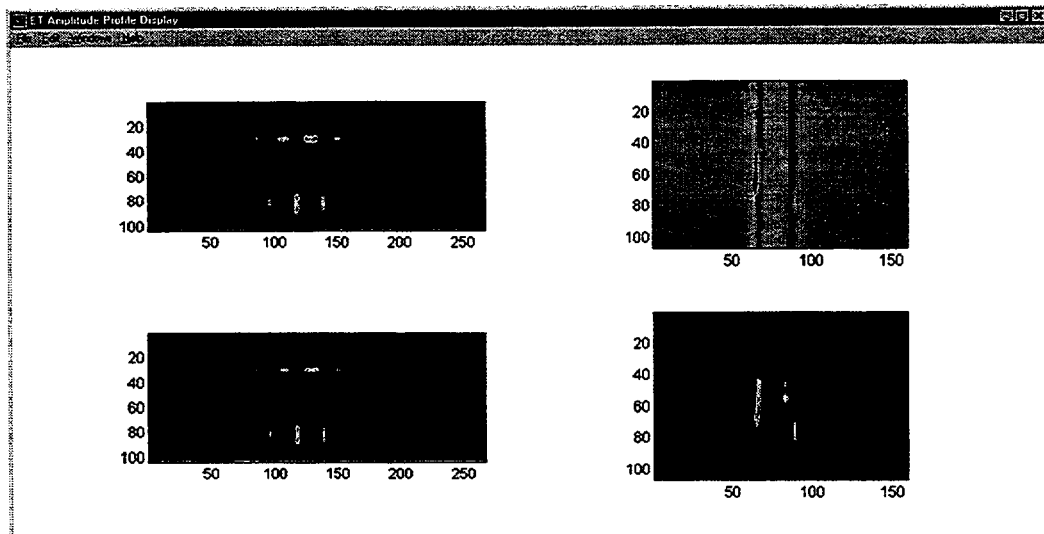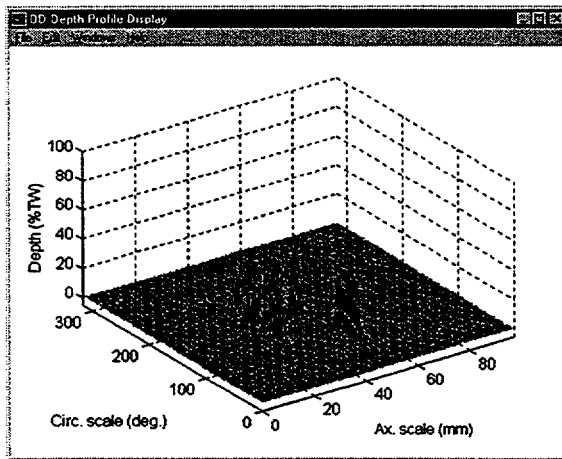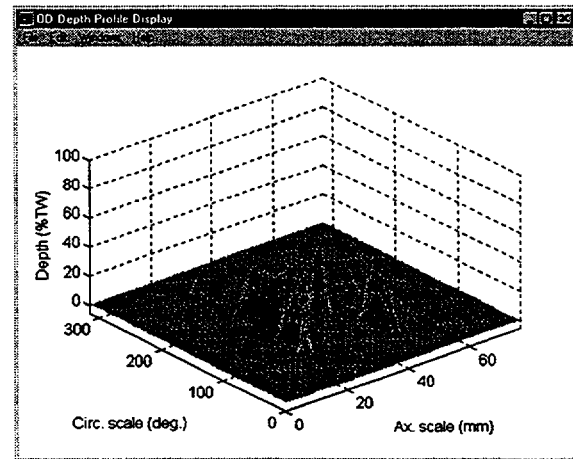
Figure 53. *Data analysis results for specimen with laboratory-grown IDSCC showing (a) Image display of scanned region of standard and flawed tube with magnetite collar placed over crack. Also shown are terrain plots of depth profile over approximately same region of tube (b) without and (c) with magnetite collar. Estimated maximum depth (<40% TW from plain tube) varies by <10% TW for all simulated artifacts.*
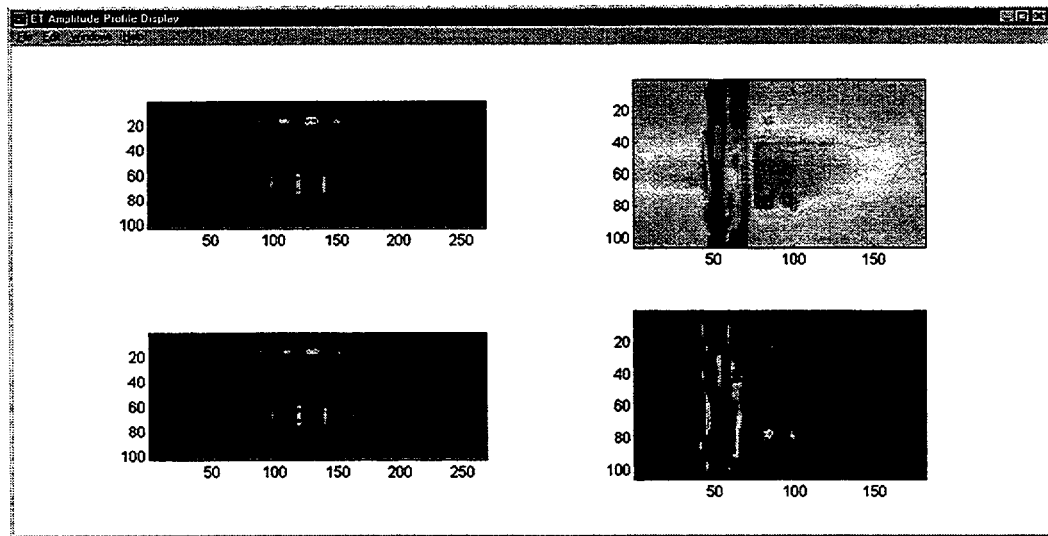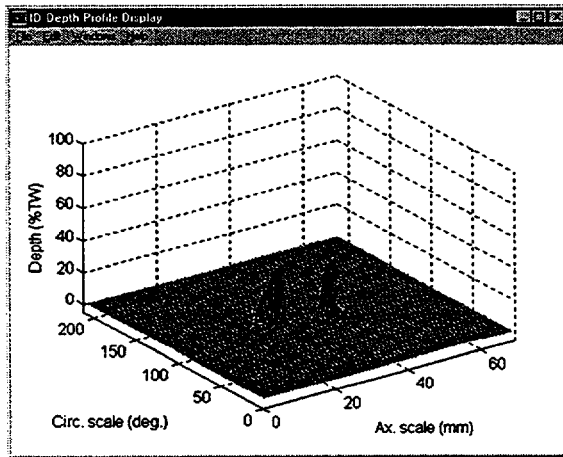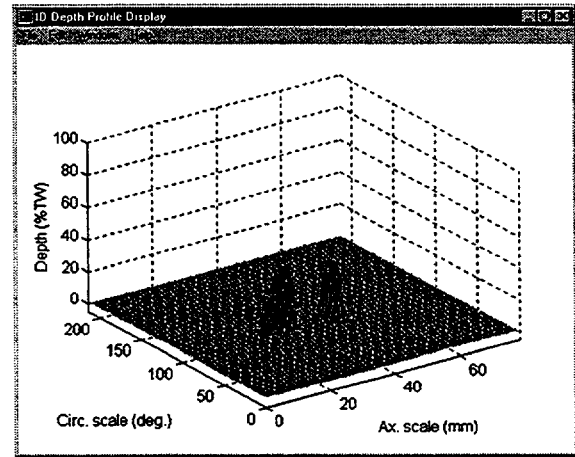
4 Benchmarking of the Multiparameter Algorithm

4.1 Stress Corrosion Cracks Used in the Benchmark Tests

In the development of the multiparameter algorithm, the results from the algorithm have been compared to fractographic results on a wide variety of SCC flaws and EDM and laser-cut notches. To provide an objective benchmark, however, an additional set of 29 SCC flaws were produced and used for a blind test of the predictions of the algorithm against fractographic measurements of the crack geometry. Six of the benchmark samples have not yet been destructively analyzed because they will also be used for leak and ligament rupture tests that have not yet been performed.

The stress corrosion cracks for the blind test were produced in a 1M aqueous solution of sodium tetrathionate at room temperature and atmospheric pressure. The Alloy 600 tubes used to produce the specimens were sensitized by heat treating at 600°C for 48 hours (h), prior to the stress corrosion cracking (SCC) to produce microstructures that are susceptible to cracking in the sodium tetrathionate. Masking by coating areas of the tubes with lacquer was used to limit or localize the cracking area. The tubes were internally pressurized for hoop stress to produce axial cracks and axially loaded to produce circumferential cracks. The times to produce cracking ranged from 20–1000 h, depending on the type of crack being produced. A variety of OD and ID crack geometries were produced; axial, circumferential, skewed, or combinations of these. Many of the specimens contained multiple cracks separated by short axial or circumferential ligaments. Cracked tubes were examined by dye penetrant techniques, conventional EC NDE, multiparameter algorithm, and destructive methods.

For the destructive examination, the samples were first heat-tinted before fracture to permit differentiation of the SCC and fracture opening surfaces, then the specimens were chilled in liquid nitrogen and the cracks were opened by fracture. The fracture surfaces were examined macroscopically and with optical and scanning electron microscopy. Details of the procedure are given in the Appendix. The fractography and NDE data were digitized to obtain tabular and graphical comparisons of the depths as a function of axial or circumferential position. Well-defined markers on the test sections provided a means to accurately overlap the profiles.

4.2 Comparison of Crack Geometries Determined by Fractography and Multiparameter Algorithm

Crack profiles from the destructive analyses are compared with those obtained from the multiparameter algorithm in Figs. 54–76. Figure 77 compares the maximum depths as determined by fractography to the maximum depths determined by the multiparameter algorithm. A linear regression fit and 95% confidence bounds for the observed data as a function of the multiparameter estimates is shown in the figure. The overall root mean square error (RMSE) in the predicted maximum depths is 13.7%. If the comparison is limited to deeper cracks, the RMSE is smaller, 9.7% for depths 30–100%, and 8.2% for ODSCC of depths 50–100%. The data are too few, however, to determine whether the apparent variation of the RMSE with depth is statistically significant.

71

Because the field of view of the rotating pancake probe is limited, the depth measurements at points ≥ 5 mm apart along the crack profile are essentially independent, and additional comparisons of the estimated depth with that determined by fractography were made at various points along the crack profile. To avoid observer bias in the selection of the data for comparison, the intersections of the crack profiles with the the major grid lines in the graphs of the superimposed profiles were chosen as the points for the comparison. This corresponds in most cases to a spacing of 5–10 mm between points. Figure 78 shows the results for 89 points from 20 different cracks, axial and circumferential, ID and OD. A linear regression curve and 95% confidence bounds for the observed data as a function of the multiparameter estimates is shown. The intercept is 13.8 in this case, somewhat less than that generated from the maximum depth data, but the slope of 0.79 is almost identical to the linear regression line slope for the maximum depth data.

The RMSE values from the data of Figs. 77 and 78, for various binned depth ranges, are presented in Tables 2 and 3. In Table 2, the depth ranges are given in terms of the fractographic depths. This is useful when assessing the capability of the multiparameter algorithm for cracks of a certain depth. In Table 3, the depth ranges are given in terms of the predicted depths. This is more useful when assessing the uncertainty in predicted depths.

The overall RMSE for all cracks of all depths is 15.1%, but this is somewhat misleading because there is significant variation in the RMSE with depth. The RMSE value is significantly better for the 80–100% TW bin than for the other depth bins.

In Table 3, two sets of RMSE values are given. One set is based on the values obtained directly from the multiparameter algorithm and the other on "corrected" values obtained from the regression fit shown in Fig. 78. For the shallowest cracks, the "corrected" values give a significantly lower RMSE value, but when all the data are considered the differences in the RMSE for corrected and uncorrected predictions are small. This indicates that there is little systematic bias in the predictions of the multiparameter algorithm, i.e., the errors are random.

The regression fit is very sensitive to the values at zero depth. However, these reflect more of a problem of detection; the errors are not really in sizing, but rather represent of cracks that were just not detected. Thus, direct comparison of the multiparameter and observed values may be a better measure of the sizing capability of the algorithm. This comparison is shown in Fig. 79, where the direct multiparameter predictions are used as the best estimate of the crack depth, and the 95% confidence bounds in the figure account for the variation of the RMSE with crack depth.

These results can be used to estimate the uncertainty in POD curves if the multiparameter algorithm is used to determine the "true" state of the mockup for the NDE round-robin. Instead of characterizing the error in the depths in terms of the overall average for all depths (≈15%), the error will be taken as a function of depth. Analytically, the values of RMSE given in Table 3 are assumed to apply at the midpoint of the depth range for each bin. The error at other depths is then estimated by linear interpolation of these values.

4.3 Comparison of Failure Pressures Predicted by Using NDE and Fractography Data

Although the accuracy of measurements of SCC crack depths by EC is usually determined by a comparison of the depth data with those measured by fractography, a more useful comparison, at least from the structural integrity standpoint, is that between the failure pressures predicted from data obtained by the two methods. Therefore, the ligament rupture pressures of all the SCC specimens were predicted by using the equivalent rectangular crack method discussed in Ref. 3. Equivalent rectangular cracks were calculated from the crack depth profiles measured by fractography, as well as those by the multiparameter algorithm. A comparison of the ligament rupture pressures predicted by using the multiparameter algorithm and fractography data is shown in Fig. 80a. A similar comparison for the unstable burst pressures is shown in Fig. 80b. The "1:1" line shows where the data would fall if there were perfect agreement between the NDE and fractographic results. Regression lines and 95% confidence bounds are also shown for the actual results. For shallower cracks (higher failure pressures), the multiparameter algorithm estimates tend to overpredict the failure pressure compared to the fractography data.

Figure 54.
Comparison of NDE and fractography profiles for specimen AGL 224 with circumferential IDSCC (crack #1).

Figure 55.
Comparison of NDE and fractography profiles for specimen AGL 224 with circumferential IDSCC (crack #2).

Figure 56.
Comparison of NDE and fractography profiles for specimen AGL 288 axial IDSCC.

Figure 57.
Comparison of NDE and fractography profiles for specimen AGL 394 with circumferential ODSCC.

Figure 58.
Comparison of NDE and fractography profiles for specimen AGL 533 with axial ODSCC.

Figure 59.
Comparison of NDE and fractography profiles for specimen AGL 535 with axial ODSCC.

Figure 60.
Comparison of NDE and fractography profiles for specimen AGL 536 with axial ODSCC.
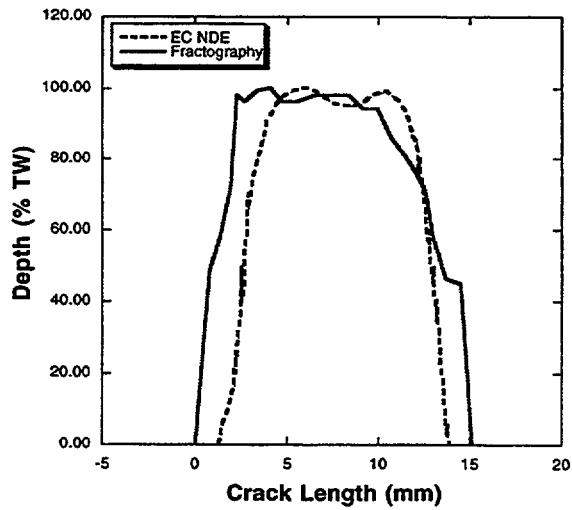
Figure 61.
Comparison of NDE and fractography profiles for specimen AGL 503 with axial ODSCC.
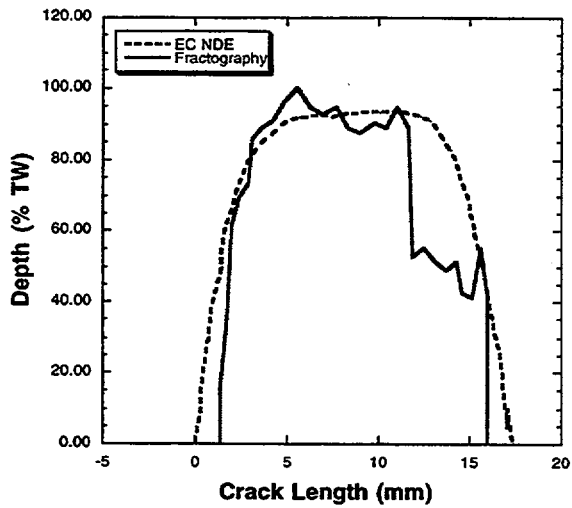
Figure 62.
Comparison of NDE and fractography profiles for specimen AGL 516 with axial ODSCC.
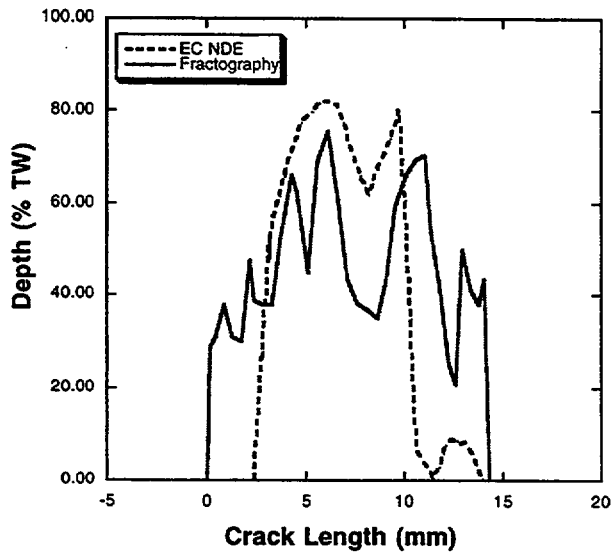
Figure 63.
Comparison of NDE and fractography profiles for specimen AGL 517 with axial ODSCC.
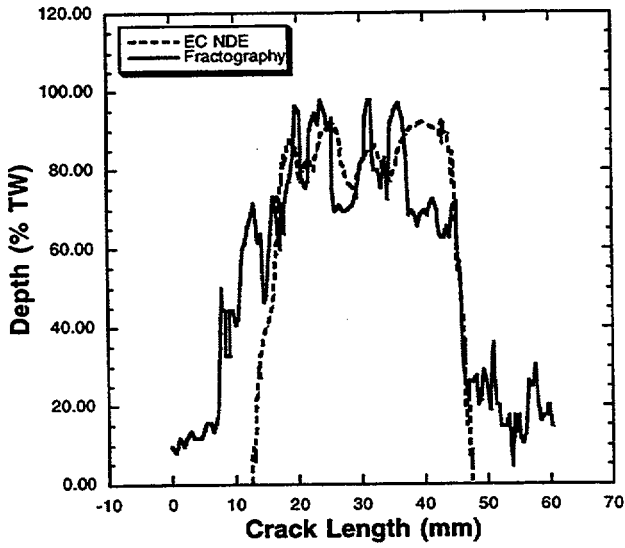
Figure 64.
Comparison of NDE and fractography profiles for specimen AGL 824 with axial ODSCC
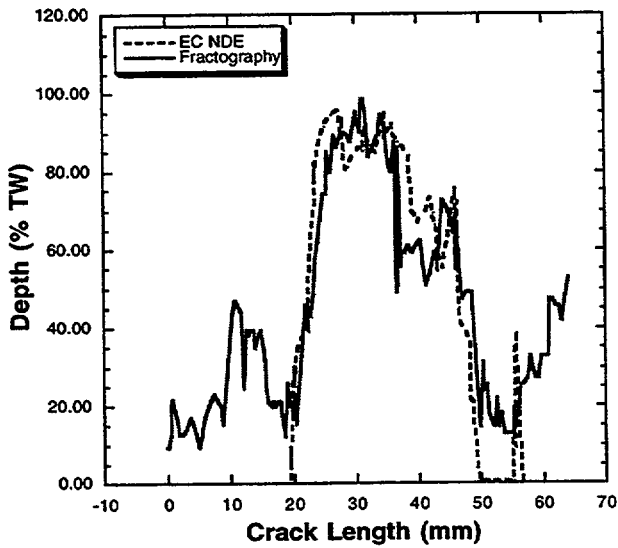
Figure 65.
Comparison of NDE and fractography profiles for specimen AGL 826 with circumferential ODSCC.
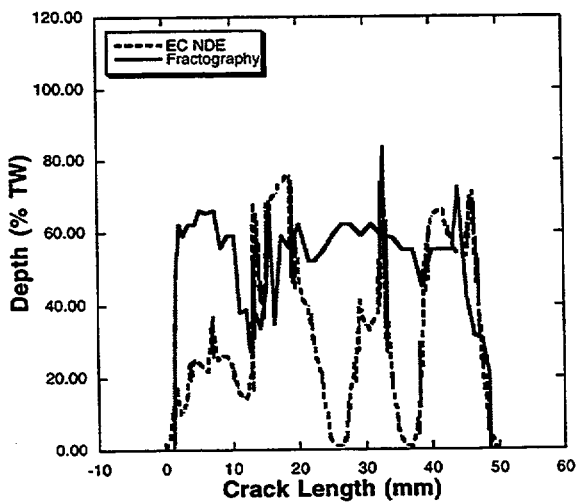
Figure 66.
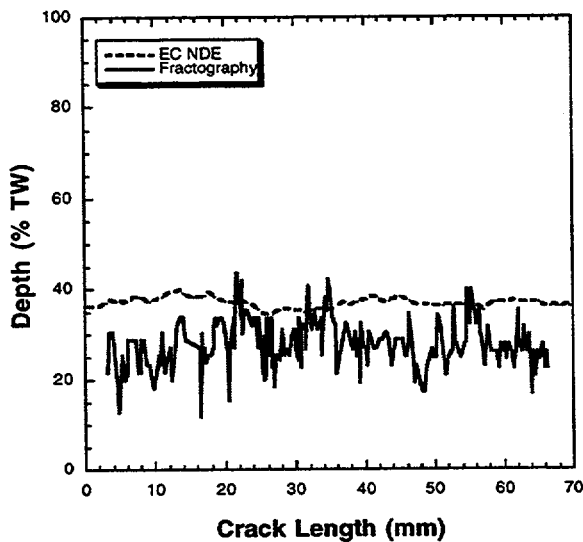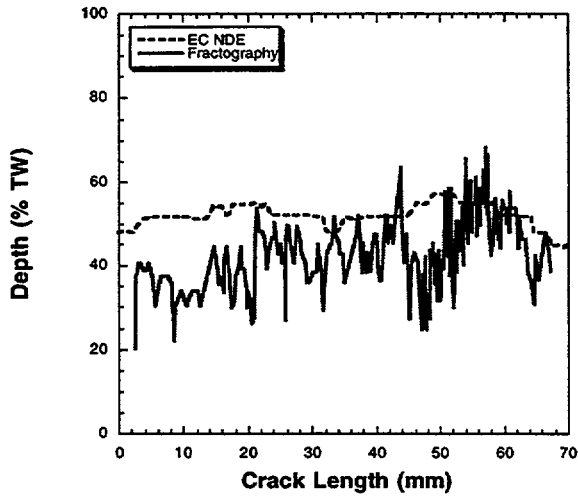*Comparison of NDE and fractography profiles for specimen AGL 835 with axial ODSCC.*
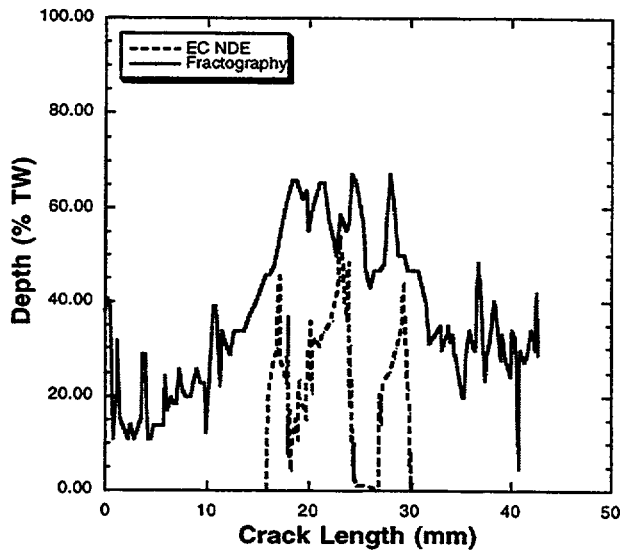
Figure 67.
Comparison of NDE and fractography profiles for specimen AGL 838 with circumferential ODSCC.
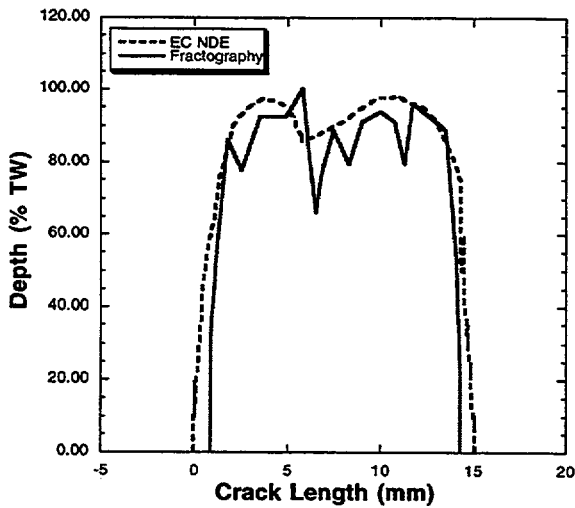
Figure 68.
Comparison of NDE and fractography profiles for specimen AGL 854 with axial ODSCC.
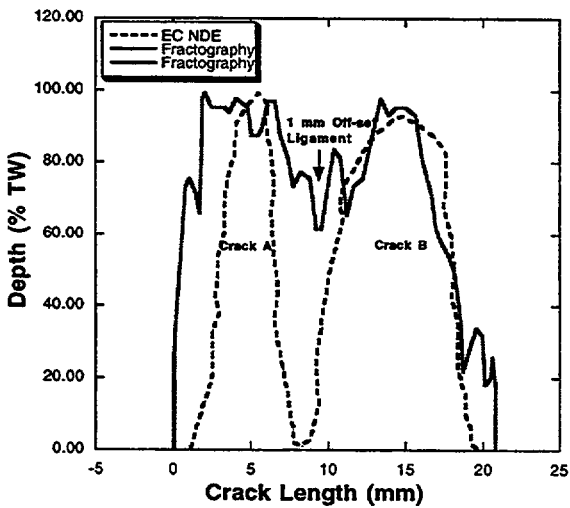
Figure 69.
Comparison of NDE and fractography profiles for specimen AGL 855 with axial ODSCC.
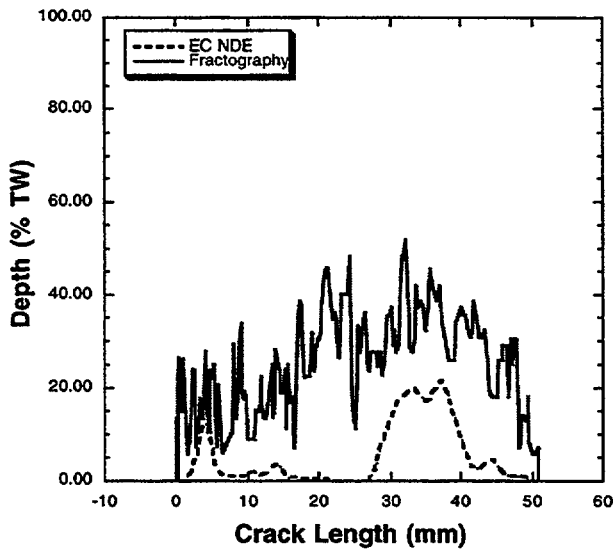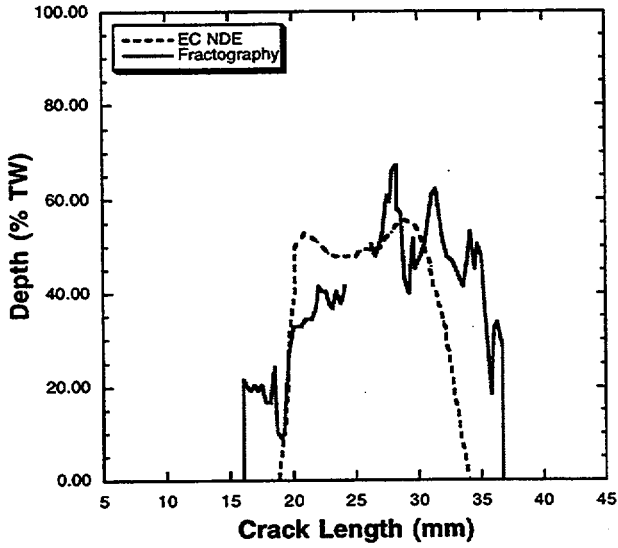
Figure 70.
Comparison of NDE and fractography profiles for specimen AGL 861 with axial ODSCC.
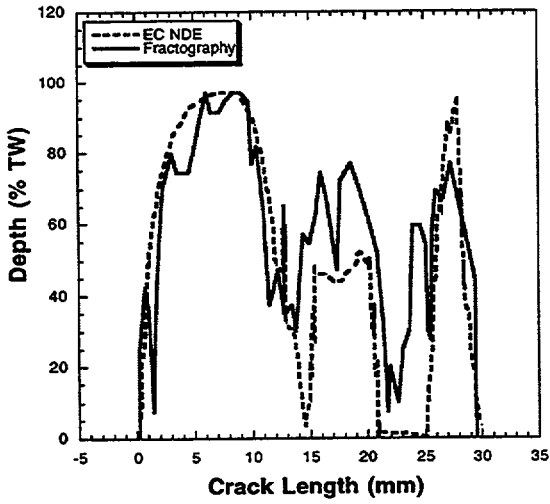
Figure 71.
Comparison of NDE and fractography profiles for specimen AGL 874 with axial ODSCC.
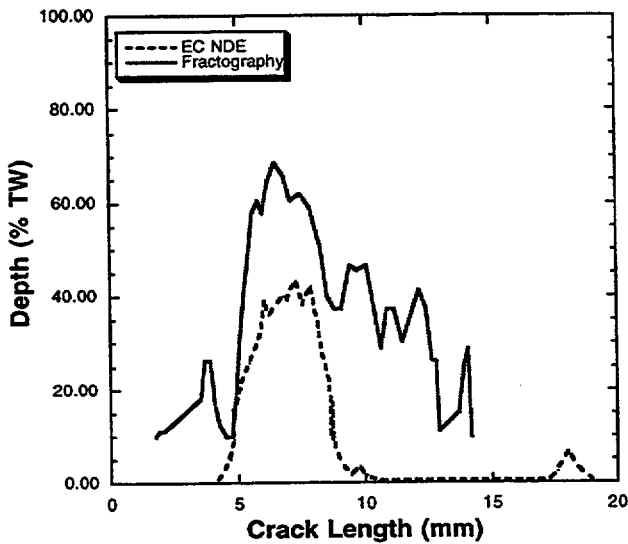
Figure 72.
Comparison of NDE and fractography profiles for specimen AGL 876 with axial ODSCC.

79
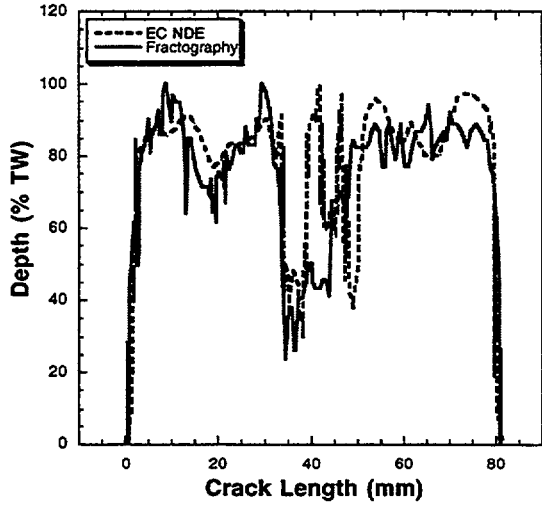
Figure 73.
Comparison of NDE and fractography profiles for specimen AGL 883 with axial ODSCC.
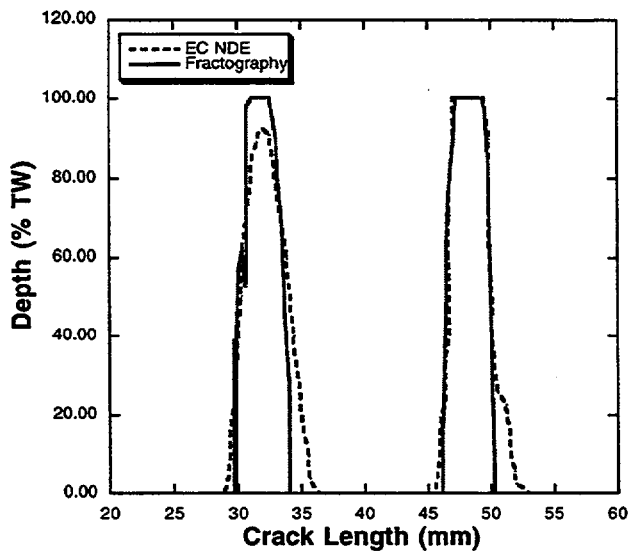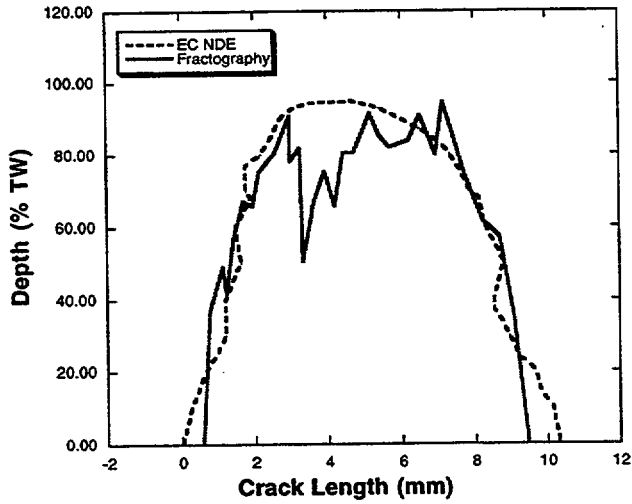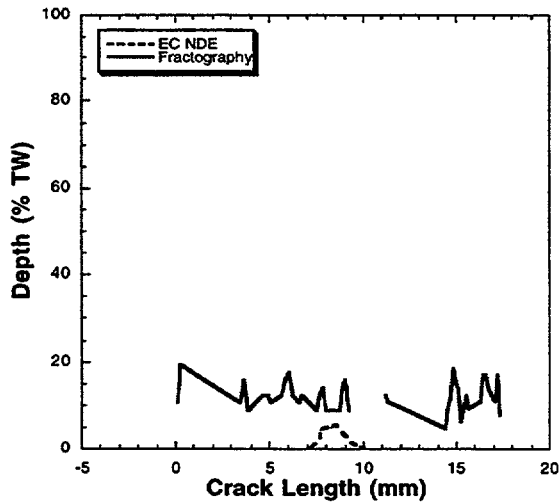

Figure 74.
Comparison of NDE and fractography profiles for specimen AGL 893 with circumferential ODSCC.
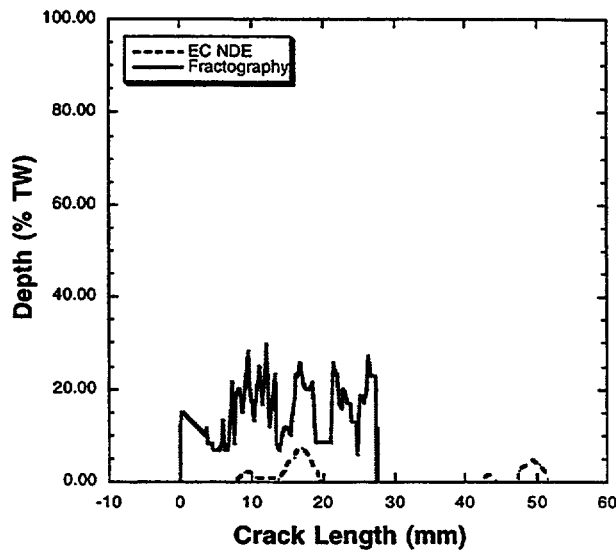
Figure 75.
Comparison of NDE and fractography profiles for specimen AGL 816 with axial IDSCC.
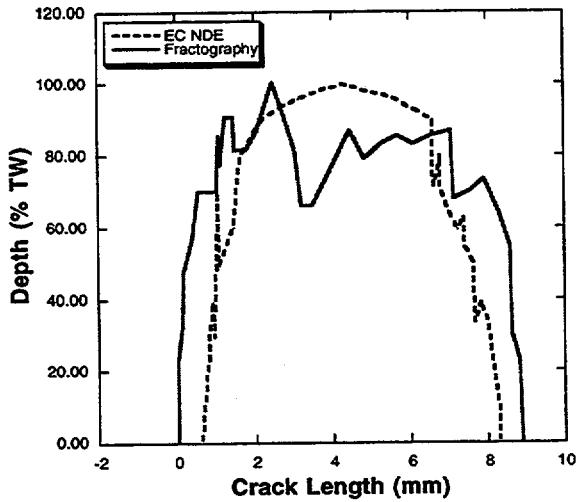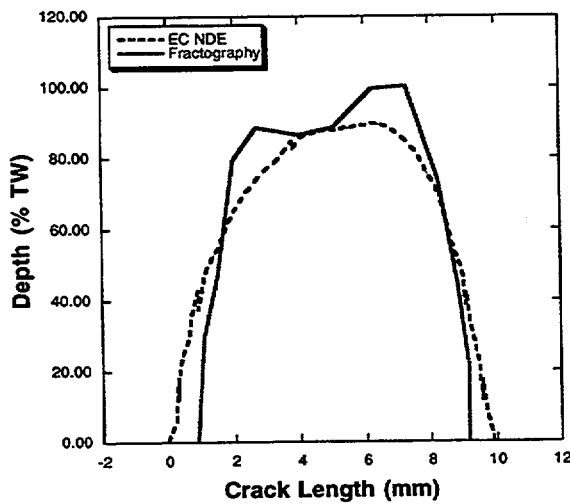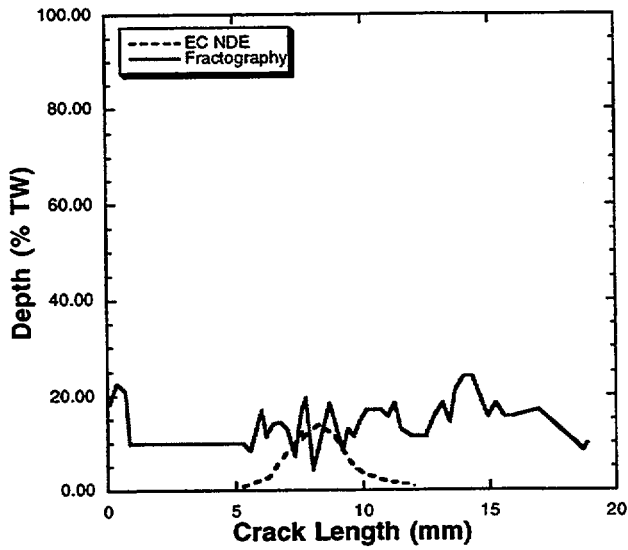
Figure 76.
Comparison of NDE and fractography profiles for specimen AGL 816 with axial IDSCC (2)
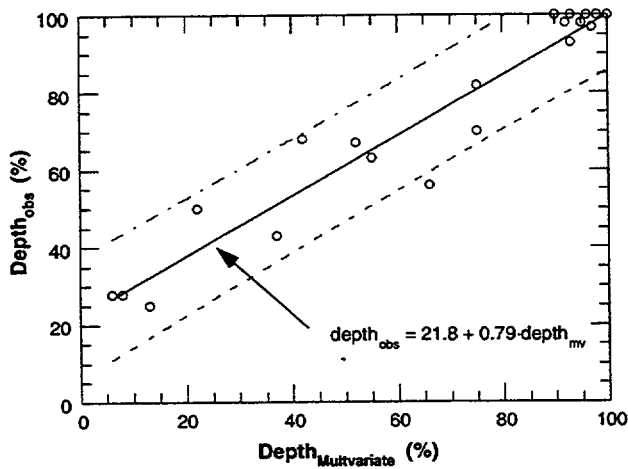
Figure 77.
Comparison of maximum depth determined by multiparameter algorithm with that determined by fractography
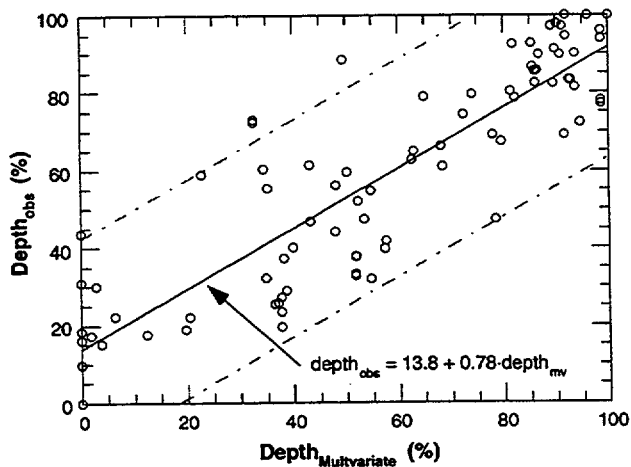
Figure 78.
Comparison of depths determined by multiparameter algorithm with those by fractography, and regression fit and estimated 95% bounds for observed depth as a function multiparameter depth estimate.
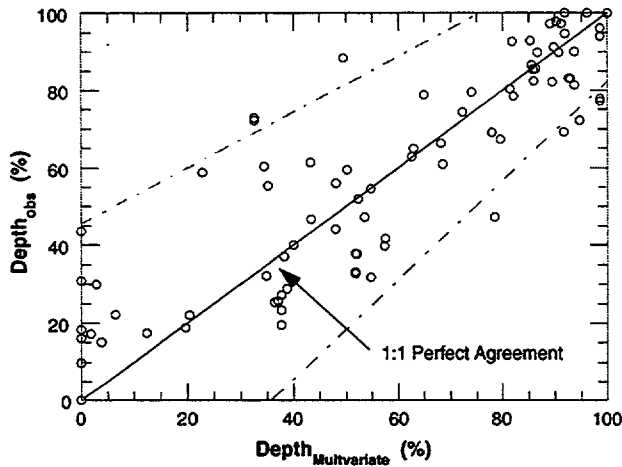
Figure 79.
Comparison of depths determined by multiparameter algorithm with those by fractography. In this case, observed and predicted results are shown in terms of "perfect agreement" 1:1 line and estimated 95% bounds that account for variation in uncertainty with depth.
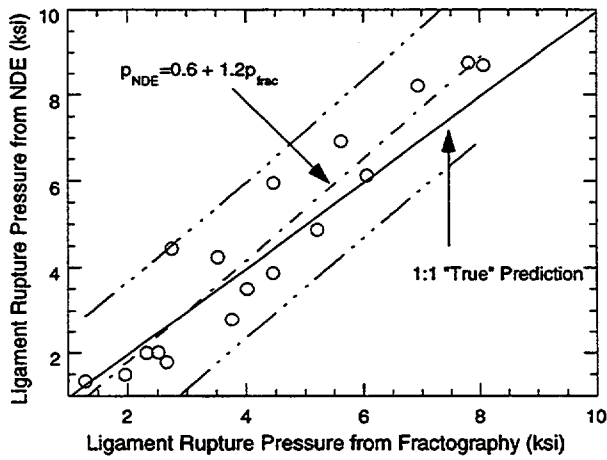
(a)
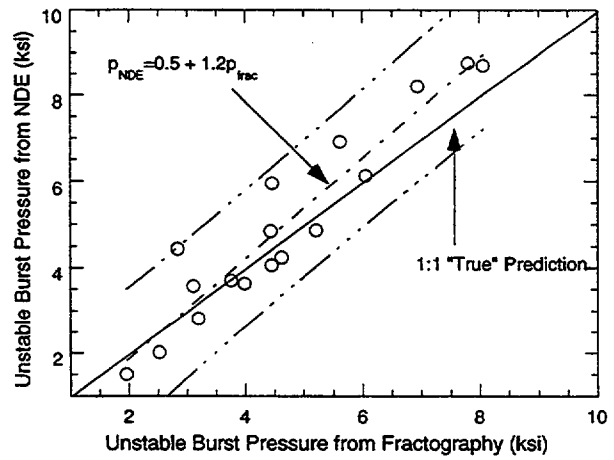
(b)

Figure 80. Comparison of predicted (a) ligament rupture pressures and (b) unstable burst pressures of specimens with SCC using crack depth profiles from fractography and advanced NDE technique. Regression fits and 95% confidence bounds are shown along with 1:1 line that would denote perfect agreement between NDE and fractography.

Table 2   *Comparison of RMSE for depth estimates by multiparameter algorithm as function of the fractographic crack depth.*

Depth range (% TW)	RMSE Maximum crack depth (% TW)
0–100	13.7
30–100	9.7
50–100 (ODSCC only)	8.2

Depth range (% TW)	RMSE Crack depth (% TW)
0–100	15.5
0–20	11.9
20–40	15.9
40–60	20.5
60–80	18.7
80–100	9.8

Table 3   *Comparison of RMSE for depth estimates by multiparameter algorithm (MP) and by regression fit in Fig. 78 as a function of predicted crack depth.*

Depth range (% TW)	RMSE Crack depth MP (% TW)	RMSE Crack depth Regression (% TW)
0–20	19.5	12.8
20–40	21.0	23.0
40–60	16.3	16.1
60–80	12.2	10.6
80–100	9.8	9.5

5 Concluding Remarks

Eddy current inservice inspection of steam generator tubes with rotating probes is carried out to overcome known limitations associated with conventional bobbin coils. High-resolution inspections with small coils inherently provide more detailed information about a tube's condition. These so-called supplementary nondestructive evaluation methods are in place both to help resolve non-quantifiable calls made by the initial bobbin coil inspections and as the recommended technique for examining difficult regions of tubing that historically have been more susceptible to cracking. Detailed manual analysis of multifrequency eddy current data collected with rotating probes can be laborious, particularly when dealing with complex and distributed cracks. Additionally, influence of undesired signals from support structures, deposits, and tube geometry variations can substantially complicate the decisionmaking process during manual analysis of data.

Studies carried out here and elsewhere have shown that EC signal amplitude is not always a reliable indicator of flaw size, particularly for cracks with complex geometries. A typical example is the apparent difference between the amplitude response from a machined notch and that from a tight or ligamented crack of comparable length and depth. Flaws that behave similarly from the structural integrity standpoint could produce EC signals with amplitude profiles that are quite dissimilar. Also, complexity of crack geometry and variability in influence of many coherent sources of signal distortion could lead to unreliable estimates of flaw size by conventional methods of data analysis. More accurate and detailed NDE information about crack profile and distribution can help to better assess the structural integrity of SG tubes for ISI applications.

Computer-aided data analysis techniques can provide reliable and efficient processing of multifrequency EC data acquired with high-resolution probes. The basic structure of a data analysis scheme for the processing of EC recordings with a standard rotating probe was described in this report. Implementation of data conversion, calibration, and analysis routines for off-line manipulation of inspection results was discussed. Sample calculations were provided in some cases to demonstrate the outcome of intermediate stages of the process. Selected examples from analyses of various batches of machined and laboratory-produced specimens with chemically induced cracking were provided to illustrate the results. Comparisons of estimated flaw profile by NDE with true state by fractography were presented to benchmark the NDE results. The influence of undesired signals from support structures and deposits on the sizing results was assessed through analysis of a subset of tubes with simulated artifacts. Effect of uncertainties in NDE estimates of flaw size on the prediction of tube structural integrity was also addressed. Certain key issues regarding the quality of data and its implications on reliability and uniformity of NDE results were discussed. Through comparative studies, results of these investigations have demonstrated that improved sizing accuracy and efficiency in processing of data can be achieved by integrating suitable algorithms for computer-aided analysis of EC inspection results.

A key objective of this work has been to characterize flaws in the ANL tube bundle mock-up in order to minimize the expense of tedious destructive examinations and to further assist in parallel studies under this program on prediction of tube structural integrity from NDE estimates of flaw profiles. NDE assessments so far have been limited to analyses of data from

rotating pancake coils; however, many of the fundamental processes described in this report are applicable to other probe geometries and coil configurations. Evaluation of signal processing and data analysis schemes to date have dealt exclusively with laboratory-grown and machined flaws that represent damage types present in the mock-up. Accordingly, simulated support structures and deposits used here closely resemble those present in the mock-up. These artifacts simulate some of the most common sources of signal distortion; however, they reproduce only a subset of those encountered during field inspections.

Investigations at ANL on computer-aided analysis of EC inspection data collected with high-resolution probes are currently aimed at improving the generalization capability of the algorithms implemented for this purpose. Future investigations in this area should involve further studies in several key areas, some of which are noted here. Suppression schemes that are more global are better suited to deal with a wider range of unwanted signals from different SG designs and associated degradation mechanisms. Also, rule-based algorithms should be adapted to handle the existing levels of variability in NDE test parameters. Furthermore, it would be desirable for such algorithms to accommodate differences in probe response due to coil designs and configurations used for ISI applications. Standard probes generally include either impedance or transmit/receive elements that may be configured as rotating or array probes. Rotating probes that are commonly used for the inspection of SG tubing often incorporate multiple coils within the probe head. Depending on coil design, they could provide multimode (differential and absolute) capability and directional sensitivity (axial or circumferential orientation of flaw). Combining readily available information from multiple coils could improve reliability in characterizing flaws. The foundation for implementing more versatile data analysis algorithms rests on the availability of data bases that encompass broad variability in parameters that influence NDE results. Efforts are currently under way to augment the NDE data base at ANL with a wider range of flaw morphologies that will also include EC inspection results from field-degraded tubes.

References

1. S. Bakhtiari and D. S. Kupperman, "Advanced NDE for Steam Generator Tubing," NUREG/CR-6638, ANL-99/9, Jan. 2000.

2. D. R. Diercks, S. Bakhtiari, K. E. Kasza, D. S. Kupperman, S. Majumdar, J. Y. Park, and W. J. Shack, "Steam Generator Tube Integrity Program," Semiannual Report, Oct. 1998 - Mar. 1999, NUREG/CR-6511, ANL-00/4, Vol. 7, 2000.

3. S. Majumdar, K. Kasza, and J. Franklin, "Pressure and Leak-Rate Tests and Models for Predicting Failure of Flawed Steam Generator Tubes," NUREG/CR-6664, ANL-99/23, Aug. 2000.

Appendix: Characterization of Corrosion and Stress Corrosion Cracks in Steam Generator Tube Specimens

A.1 Scope and Application

This procedure is for metallurgical and destructive examination of laboratory-degraded steam generator (SG) tubes with corrosion attack or stress corrosion cracks. It is not applicable for the tubes contaminated with radioactive substances. The procedure includes method of preparation, examination, and disposition of SG tubes to be examined. Examination techniques include dye penetrant examination, pressure and rupture, fractography, cross-sectional microscopy, optical macro/microscopy, and scanning electron microscopy.

This procedure is written in a general sequence of operation. Portions of the procedure may be skipped when judged unnecessary by the principal investigator.

General Precaution

Use protective sleeves for tubes to prevent scratch or other mechanical damage. Wear clean pair of gloves to handle tubes not to contaminate surface. When transferring specimen, record onto data; your name, location or name of person you are transferring to, purpose of transfer, date, and your initial.

Identification of Tube

Verify the alphanumeric identification (ID) that is permanently inscribed on the OD at both ends of each tube (Figure A1). This ID must be carried through the entire procedure. Any subsections of tube specimen resulting from cutting or fracture must be permanently marked with the ID. All documentation should be referenced to the ID.
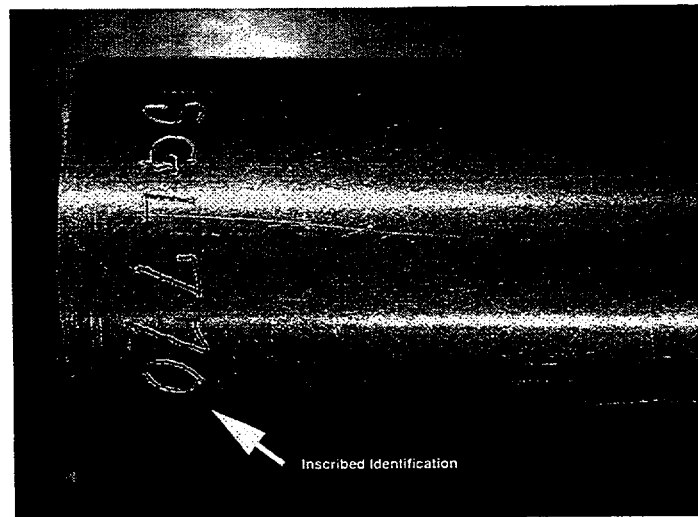

Inscribed Identification

Figure A1. Inscribed identification of tube specimen

A.2 Dye Penetrant Examination

Dye penetrant examination is performed for degradations on the OD. After completion of degradation process, tube specimen is ultrasonically cleaned in high-purity water and dried. Dye penetrant examination is performed in the vicinity of degradation.

Magnaflux Spotcheck SKC-S Cleaner/Remover is sprayed onto test area to clean surface, and then wiped off repeatedly until the surface is clean.

Magnaflux Spotcheck SKL-SP Penetrant is sprayed over the test area and left for 1 to 30 minutes; usually 10 minutes is sufficient. To remove excess penetrant, SKC-S Cleaner/Remover is sprayed onto a clean dry paper towel that is then used to lightly wipe the test area.

Magnaflux Spotcheck SKD-S2 Developer is lightly sprayed over the test area by holding the spray can about 8 to 12 inches from the surface. Wait for 5 to 15 minutes, then inspect.

If the above procedures are not satisfactory, clean the surface with the Magnaflux Spotcheck SKC-S Cleaner/Remover, then ultrasonically clean the tube in high-purity water, dry, and clean again with the Magnaflux Spotcheck SKC-S Cleaner/Remover. Then Magnaflux Zyglo 2L-27A Penetrant is sprayed over the test area and left for 1 to 30 minutes; usually 10 minutes is sufficient. Wipe off the penetrant with a clean dry paper towel. To remove excess penetrant, the SKC-S Cleaner/Remover is sprayed onto a clean dry paper towel that is used to lightly wipe the test area.

Magnaflux Zyglo 2P-9f Developer is lightly sprayed over the test area by holding the spray can about 8 to 12 inches from the surface. After 10 minutes, the test area is inspected by using a fluorescent light to visualize degradation.

Results of the dye penetrant examination are documented by photography at 0.5–5X magnification. The photograph should include a calibrated scale so that the magnification factor may be measured directly from the photograph (Fig. A2).
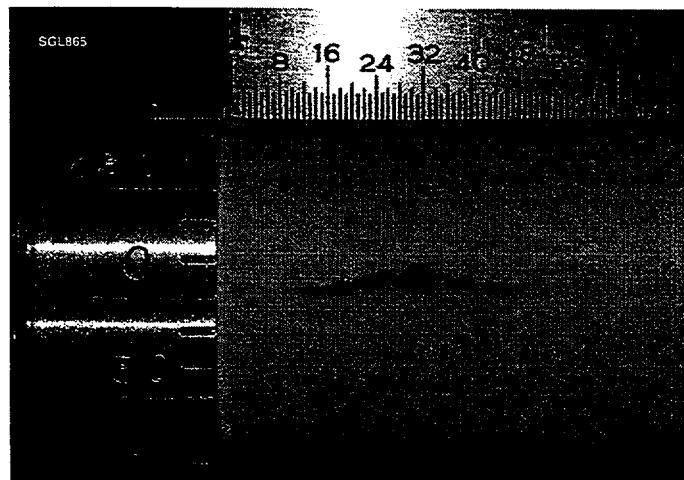
Figure A2. Dye penetrant examination of tube specimen SGL 865.

A.3 Installation of Reference Markers

NDE-detectable markers are attached on the OD in the crack area to provide reference positions of degradation. These markers are used to locate the NDE indications, to decide proper sectioning procedure and locations (Section 9), and to verify relative position between degradations (Section 14).

Four pieces of platinum wire (about 0.010 inches diameter), each of a different length (0.125, 0.250, 0.375, and 0.500 inches), are spot-welded, properly spaced, in the crack area (Fig. A3). Denting or scribe marks may also be used for the purpose. Be careful not to loosen the attached markers from the specimen throughout the process.

NDE indications for the markers and degradations must be simultaneously presented so that relative positions between the markers and degradation can be determined.
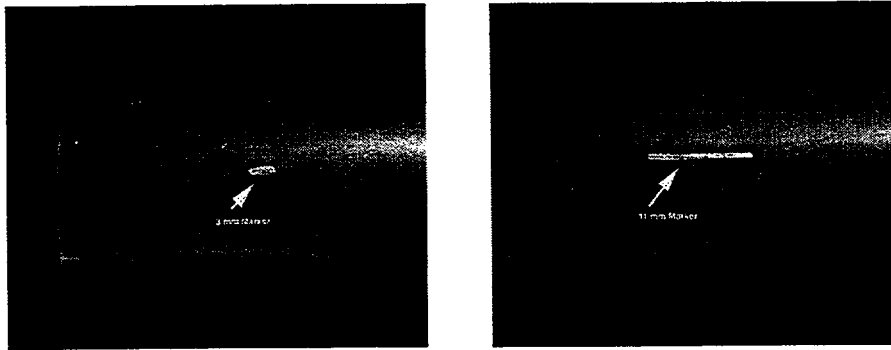
Figure A3. Wire markers attached to tube specimen.

A.4 Nondestructive Examination

Eddy current or other NDE measurements are performed on the tubes with the markers attached. The results should include a profile of degradation in real space coordinates, and EC voltages. The profile should also simultaneously include images that properly identify the four different markers with respect to degradation in real space coordinates (Fig. A4).
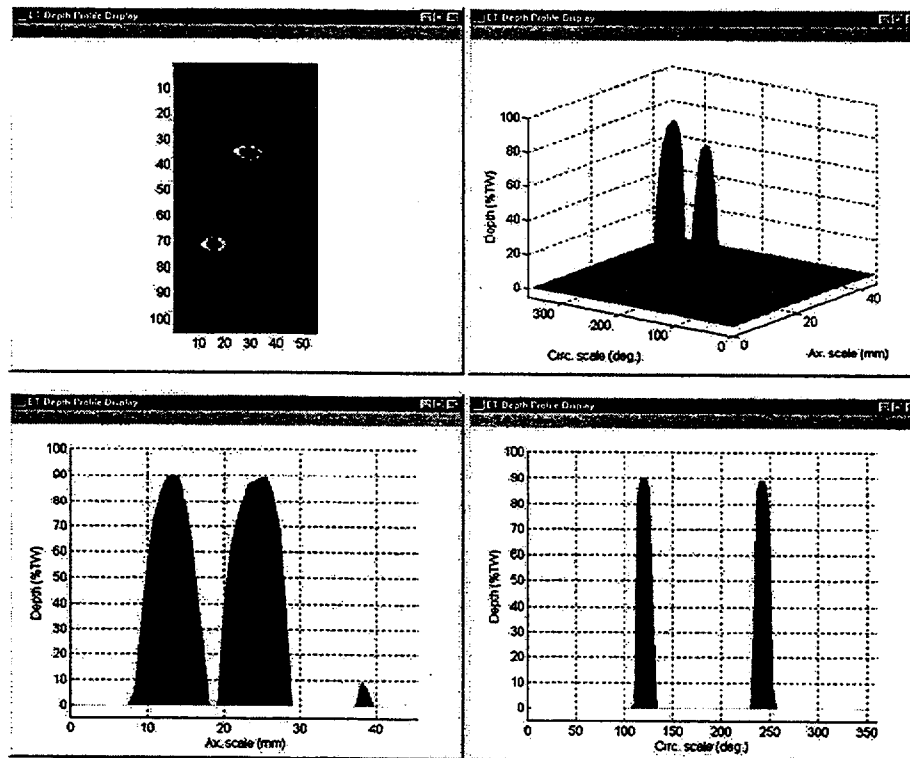
Figure A4. EC NDE evaluation of tube specimen.

Heat Tinting

To discriminate SCC and fracture area, the specimen is heat tinted for 1-5 minutes at 600°C in air atmosphere. This makes the SCC appear in darker contrast to the fracture area.

Pressure-Leak Testing

Pressure-leak testing may delineate SCC more clearly, particularly for tight, shallow secondary cracks and networks of cellular cracks. Applied pressure is higher than that used to produce degradation. However, application of too much pressure should be avoided because gross plastic deformation of the tube and degradation can introduce significant inaccuracies in measuring flaw size and shape. The correct pressure is selected by the principal investigator with consideration of the flow stress of the material, prior degradation process history, and type and extent of degradation.

Document the pressure-leak test results by photographs (Fig. A5).
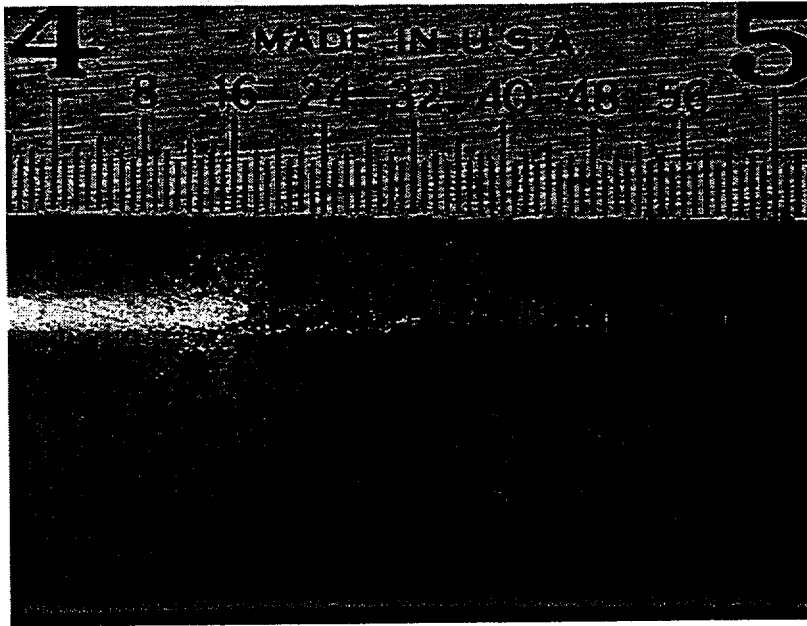
Figure A5. Tube specimen SGL 413 with OD axial SCC after pressur-leak test.

Dye Penetrant Examination after Pressure-Leak Testing

Dye penetrant examination is performed according to the procedure in Section A2. The degradation might have opened more during the pressure and leak testing and additional dye penetrant indications may be seen. Document the results.

Sectioning of Tube Specimen

General mapping for the location of degradation is constructed from the EC/NDE and dye penetrant examination results. The map should include the size and location of degradations, and distances between degradations. The tube is sectioned into convenient pieces for cross-sectional metallography or fracture. The map should also include the detailed sectioning plan.

Metallography of Cross Section

Cross-sectional microscopy is performed on a metallographically polished surface. The specimen may be etched to delineate grain boundaries and other microstructural features, by electrolytic etching in a 5% nitric acid–alcohol solution at 0.1 mA/mm^2 for 5-30 seconds, or by other techniques.[A1] The etching may also enhance the image contrast, but the tip of a tight intergranular crack could be confused with a grain boundary. Photographic images are recorded at 10-500X magnification (Fig. A6).

Axial ODSCC   Branched Axial ODSCC
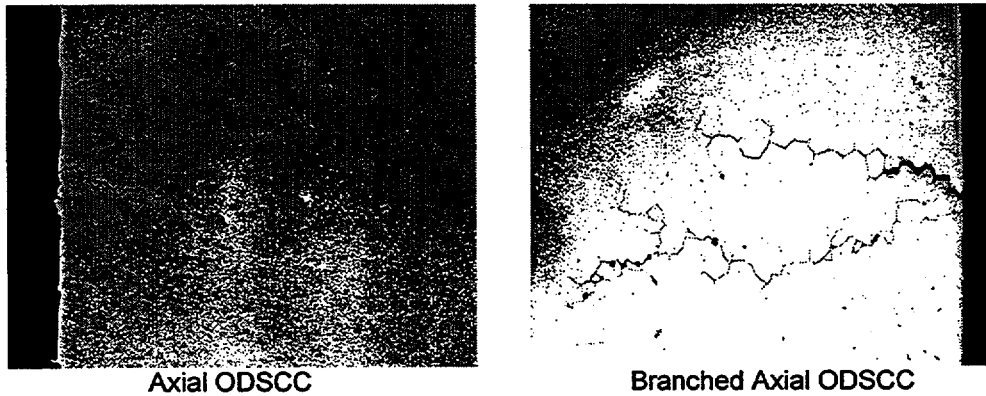
Figure A6. Cross-sectional optical metallography.

A.5 Fracture of Specimen

Degradation is opened by fracture, and the fracture surface is examined by optical or scanning macro/microscopy. The size of the undegraded ductile fracture area may be minimized by properly selecting the size of the fracture specimen or introducing notches near the ends of degradation. Nevertheless, sectioning or cutting should not destroy any part of the degradation.

The specimen is first chilled in a liquid nitrogen bath, and then fractured by fatigue loading, which may be applied by a fatigue machine or manually. The loading should ensure that degraded surfaces are not rubbed against each other or disturbed. In some instances, the specimen may further be plastically deformed to delineate degradations that were not detected by NDE or dye penetrant examination.

Pieces of the specimen resulting from the fracture should be clearly identified, marked with new identification numbers, and documented.

A.6 Digital Fractography

The fractured surfaces are recorded by digital photography at 0.2–10X magnification (Fig. A7). A calibrated scale must be included in the digital photography of the fracture surface in the same frame. The optimal magnification factor is selected, depending on the size and shape of the degradation. Methods of illumination of fracture surface play an important role in obtaining the optimal image quality; the best illumination may be found by trial-and-error. For a large crack, photographs may be taken of partial areas, and then a composite photograph may be constructed later. Reference markers are needed for partial photography, but should not disturb the degradation.

All digital photographs must be identified with a unique and proper file name that is traceable to a particular degradation and tube.
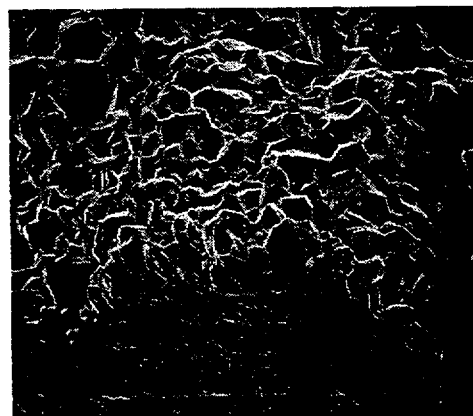
Figure A7. Scanning electron microscopy for fractography of tube specimen SGL 413.

Scanning electron microscopy (SEM) of a fracture surface will provide size and shape of degradation, and information on the type of degradation, in a three-dimensional perspective (Fig. A8). SEM may be performed at 5–2000X magnification, depending on the features of interest. For size measurements, calibrated size references should be attached close to the area of interest and photographed simultaneously with the fracture surface in the same frame. The overall SEM magnification factor alone will not be enough to accurately determine the degradation size.

All SEM photographs must include the magnification factor and be identified with a unique and proper file name that is traceable to a specific degradation and specific tube ID.
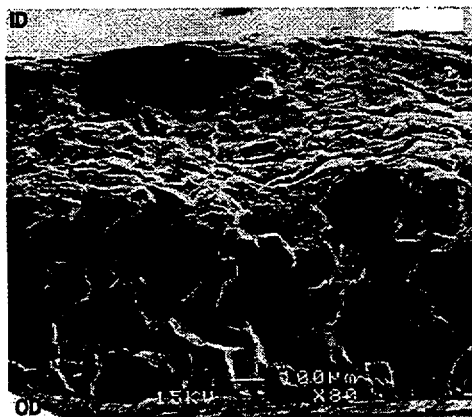
SEM of axial ODSCC   SEM of circumferential ODSCC

Figure A8. Scanning electron microscopy of ODSCC.

A.7 Comparison of Destructive Fractography with NDE Measurements

The contours of a crack determined by fractography and NDE evaluation are digitized by using software such as Datathief. Sampling distance depends on the complexity of the crack geometry. Short sampling distances should be used for a complicated geometry over a small scale, while longer distances may be used for simpler geometries, e.g., straight line or smooth
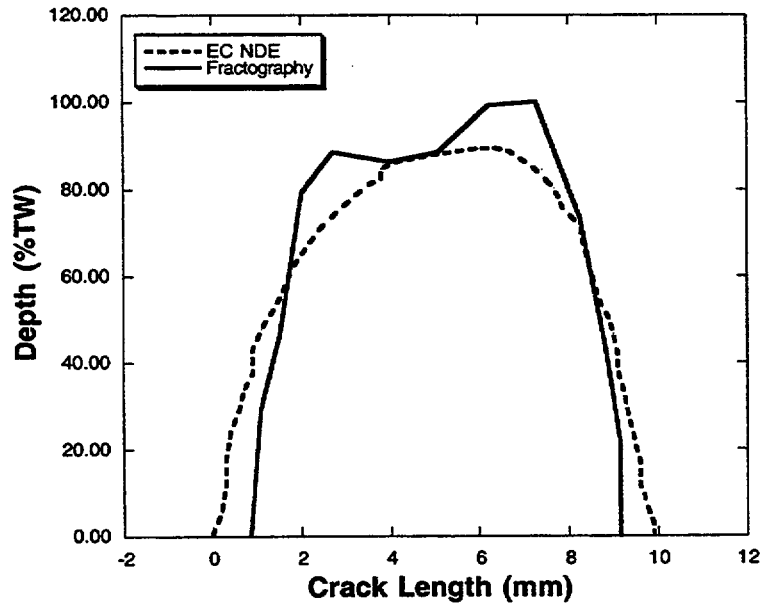
Figure A9. *Size and shape of OD axial SCC in tube specimen AGL 536 determined by EC NDE and Fractography.*

contours. Digitized data are plotted for graphical presentation with software such as KaleidaGraph. Fractography and NDE results may be plotted simultaneously for comparison (Fig. A9).

Digitized data are stored with proper file names that are traceable to a specific degradation and tube.

Disposition and Documentation

All subsections and remainders should be clearly marked with ID and stored in the tube specimen rack and in the respective metallography specimen box. The storage is recorded in the main data log.

Results of examination and characterization are documented as a part of the scientific notebook and maintained for the period required by the program.

References for Appendix

A1 Metallography and Microstructure, Metals Handbook, 9th Ed., Vol. 9, American Society for Metals (1985).

A2 Fractography, Metals Handbook, 9th Ed., Vol. 12, American Society for Metals (1987).

1. REPORT NUMBER (Assigned by NRC, Add Vol., Supp., Rev., and Addendum Numbers, if any.)
NUREG/CR-6746 ANL-01/21

2. TITLE AND SUBTITLE

Advanced Nondestructive Evaluation for Steam Generator Tubing

3. DATE REPORT PUBLISHED	
MONTH	YEAR
October	2001

4. FIN OR GRANT NUMBER
W6487

5. AUTHOR(S)

S. Bakhtiari, J.Y. Park, D.S. Kupperman, S. Majumdar, W.J. Shack

6. TYPE OF REPORT

Technical; topical

7. PERIOD COVERED *(Inclusive Dates)*

8. PERFORMING ORGANIZATION - NAME AND ADDRESS *(If NRC, provide Division, Office or Region, U.S. Nuclear Regulatory Commission, and mailing address; if contractor, provide name and mailing address.)*

Argonne National Laboratory
9700 South Cass Avenue
Argonne, IL 60439

9. SPONSORING ORGANIZATION - NAME AND ADDRESS *(If NRC, type "Same as above"; if contractor, provide NRC Division, Office or Region, U.S. Nuclear Regulatory Commission, and mailing address.)*

Division of Engineering Technology
Office of Nuclear Regulatory Research
U.S. Nuclear Regulatory Commission
Washington, DC 20555-0001

10. SUPPLEMENTARY NOTES

J. Muscara, NRC Project Manager

11. ABSTRACT *(200 words or less)*

This report describes research activities carried out at Argonne National Laboratory (ANL) as part of the Steam Generator (SG) Tube Integrity Program sponsored by the U.S. Nuclear Regulatory Commission (USNRC). As a follow-up to a preceding publication on the assessment of advanced nondestructive evaluation (NDE) techniques for inservice inspection of steam generator tubing. This report provides an overview of more recent studies associated primarily with signal processing and data analysis techniques applied to eddy current NDE. Results of efforts made to date on implementation of various algorithms that pertain to computer-aided analysis of eddy current rotating probe data are discussed. As a benchmark for NDE accuracy, production and destructive characterization of specimens with laboratory-induced cracking are described. The effect of uncertainties in NDE estimates of flaw size on the prediction of tube structural integrity is addressed.

12. KEY WORDS/DESCRIPTORS *(List words or phrases that will assist researchers in locating the report.)*

Steam Generator
Stress Corrosion Cracking
In-service Inspection
Eddy Current Testing
Nondestructive Evaluation
Rotating Probes
Signal Processing
Computer-aided Data Analysis

13. AVAILABILITY STATEMENT

unlimited

14. SECURITY CLASSIFICATION
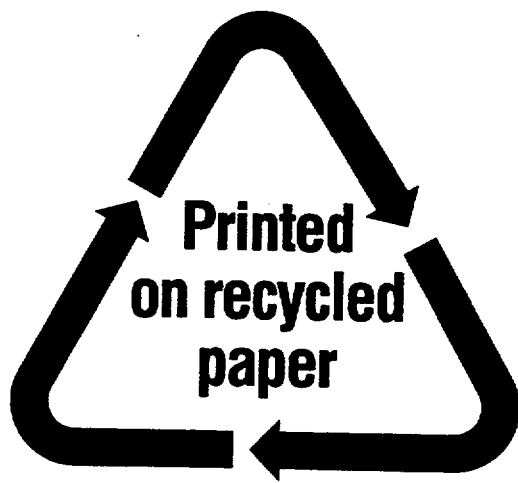
(This Page)
unclassified

(This Report)
unclassified

15. NUMBER OF PAGES

16. PRICE